AD________________

Award Number: DAMD17-99-1-9379

TITLE: Improving Detection of Axillary Lymph Nodes by Computer-Aided Kinetic Feature Identification in Positron Emission Tomography

PRINCIPAL INVESTIGATOR: Xiaoli Yu, Ph.D.

CONTRACTING ORGANIZATION: The University of Southern California
Los Angeles, California 90089-9074

REPORT DATE: August 2004

TYPE OF REPORT: Final

PREPARED FOR: U.S. Army Medical Research and Materiel Command
Fort Detrick, Maryland 21702-5012

DISTRIBUTION STATEMENT: Approved for Public Release;
Distribution Unlimited

REPORT DOCUMENTATION PAGE

Form Approved
OMB No. 074-0188

1. AGENCY USE ONLY (Leave blank)	2. REPORT DATE	3. REPORT TYPE AND DATES COVERED
	August 2004	Final (1 Aug 99 - 31 Jul 04)

4. TITLE AND SUBTITLE
Improving Detection of Axillary Lymph Nodes by Computer-Aided Kinetic Feature Identification in Positron Emission Tomography

5. FUNDING NUMBERS
DAMD17-99-1-9379

6. AUTHOR(S)
Xiaoli Yu, Ph.D.

7. PERFORMING ORGANIZATION NAME(S) AND ADDRESS(ES)
The University of Southern California
Los Angeles, California 90089-9074

E-Mail: xiyu@csi.usc.edu

8. PERFORMING ORGANIZATION REPORT NUMBER

9. SPONSORING / MONITORING AGENCY NAME(S) AND ADDRESS(ES)
U.S. Army Medical Research and Materiel Command
Fort Detrick, Maryland 21702-5012

10. SPONSORING / MONITORING AGENCY REPORT NUMBER

11. SUPPLEMENTARY NOTES

12a. DISTRIBUTION / AVAILABILITY STATEMENT
Approved for Public Release; Distribution Unlimited

12b. DISTRIBUTION CODE

13. ABSTRACT (Maximum 200 Words)

The goal of this project is to improve detection of metastatic axillary breast cancer through sophisticated physiological modeling and statistical signal processing techniques. The major focus of this project was to explore temporal physiological differences in malignant and normal tissues based on the advanced FDG-PET kinetic modeling assessment; assess and improve the accuracy of ROI-based molecular feature extraction techniques from the known primary breast tumor; design the space-temporal filtering and detection criteria to identify the early metastases from sever background interference and count noise; integrate the developed feature extraction and filtering/detection criteria into a software prototype of Intelligent Detection of Early Metastasized Molecular Feature (IDEMMF) system; and test and evaluate the prototype with phantom, animal study and clinical patient study. Our theoretical findings include mathematically map of the physiological differences in temporal domain onto the kinetic (macro) parameter domain; revealing and characterization of the temporal or parametric domain differences in frequency domain and time-frequency. The evaluations on a small scale of animal and patient data show that the IDEMME system can significantly enhance the metastatic lesion detection by exploring the temporal differences in dynamic FDG-PET images.

14. SUBJECT TERMS	15. NUMBER OF PAGES
Breast Cancer, Axillary Disease, PET, Statistical Signal Processing	83
	16. PRICE CODE

17. SECURITY CLASSIFICATION OF REPORT	18. SECURITY CLASSIFICATION OF THIS PAGE	19. SECURITY CLASSIFICATION OF ABSTRACT	20. LIMITATION OF ABSTRACT
Unclassified	Unclassified	Unclassified	Unlimited

NSN 7540-01-280-5500

Standard Form 298 (Rev. 2-89)
Prescribed by ANSI Std. Z39-18
298-102

Table of Contents

1. Introduction

Despite significant advances in primary and metastatic lesion detection with static PET, the ability to accurately detect axillary metastases at an early stage remains the greatest challenge in breast cancer imaging. At an early stage, radiotracer uptake of metastatic tissue is often weak, due to the relatively fewer cells involved with disease. Moreover, the diseased tissue and abnormal uptake is, in most circumstances, embedded in severe background interference and count noise, thus hardly differentiated from surrounding normal tissues with visual inspection in either 2-D or 3-D static PET images. Once metastases develop into fully visible lesions, detection may already been delayed for a certain amount of time. To avoid or reduce such delay it is desired that the molecular changes of metastases in PET images can be detected from interference at an earlier stage before they become completely visible.

This proposed project uses a different approach to enhance the signal-to-noise ratio (SNR) in PET images for early metastasis detection. We have been developing an intelligent detection of early metastasized molecular feature (IDEMMF) system for evaluating axillary metastatic lesions at an early stage with dynamic positron emission tomography (PET). The objective is to extend lesion visibility from limited 2-D or at most 3-D to a higher dimensional space, where molecular features in the malignancy and normal tissue can be better distinguished. Thus, increasing the SNR of metastatic lesions not routinely visualized becomes approachable. The premise of this approach is that molecular features available in dynamic PET data in the primary tumor of an individual patient can be used to identify early metastases that are obscured by overlying background tissue activities. IDEMMF "learns" the molecular features from the primary tumor and normal tissues of an individual patient in order to identify the tumor-like multidimensional (temporal + 3D spatial) molecular features of tissues that are undergoing metastases but too weak to be visualized due to server background interference and count noise. Using IDEMMF, these features can be enhanced via a combination of sophisticated PET molecular imaging models and advancing image processing techniques.

2. Body

The whole proposed study consists of four tasks: *Task 1*: Developing the mathematical formula to linearly map and identify the physiological features contained in PET dynamic sinogram sequence (Month 1-8), *Task 2*: Developing the schemes for objective reduction of dynamic sinogram data guided by the identified TAC subspaces of the desired signal (tumor) and the interference (normal tissue background plus noise) (Month 4 - 12), *Task 3*: Deriving and analyzing statistical hypothesis test criteria to test the presence of an axillary metastasis in the dynamic images reconstructed from the compressed sinogram data (Month 13 - 24), and *Task 4*: Clinical Evaluation (Month 13 - 36). For each task, several subtasks were defined (see the SOW in the grant application for details).

The hypothesis was tested in the project is

Hypothesis: *The molecular mechanisms and kinetics of [18F] FDG in the metastases of the individual patient are similar to those in primary tumors, but differ from those in normal tissue. The multidimensional molecular features extracted in visible primary lesion and normal tissues of a patient can be utilized to enhance the tumor-like features in faint or invisible metastases by cleaning up the normal background and statistical noise superimposed on them.*

The Intelligent Detection of Early Metastasized Molecular Feature (IDEMMF) system under the development consists of four major modules as depicted in Fig 1 (1) tracer molecular modeling; (2) primary tumor feature extraction; (3) feature-guided filter design; and (4) detection criteria design. The functions and interactive relationship of these modules are described as follows. In general, the tracer model is the vehicle to define the relationship between the noninvasive in vivo measured dynamic molecular PET data and a set of parameters reflecting local rates of physiological transport, molecular behaviors and biochemical reactions. Parameter estimation mathematically extracts useful physiological information intrinsic to molecular features of the time activity curve (TAC) of known normal tissues and primary malignancy in a dynamic PET image sequence. These procedures have been well-established in the literature. In our technique, however, once the parameter estimations were obtained for an individual patient, the corresponding molecular feature spaces, spanned by a few molecular feature vectors specifically associated to this patient, was formed for both malignant and normal tissues. A feature-guided filter was then designed for this patient, based on his/her own feature spaces rather than on pooled-training features, considering molecular behaviors may vary from patient to patient. The single patient tuned filter was applied to the dynamic images in order to objectively suppress the background tissue interference and statistical noise from the contaminated TACs of small, faint metastatic lesions that could not be discerned on routine visual inspection. The filtered sets under two hypothesized data models were processed further by a statistical hypothesis testing procedure. This procedure made hypotheses on the data according to tissue types (normal or malignant) and then tested to see which hypothesis the measured data were most likely consistent with. The outputs of signal detection which were proportional to the likelihood (probability) of a given hypothesis being true or false for each measurement were used as an adjunct to visual inspection.

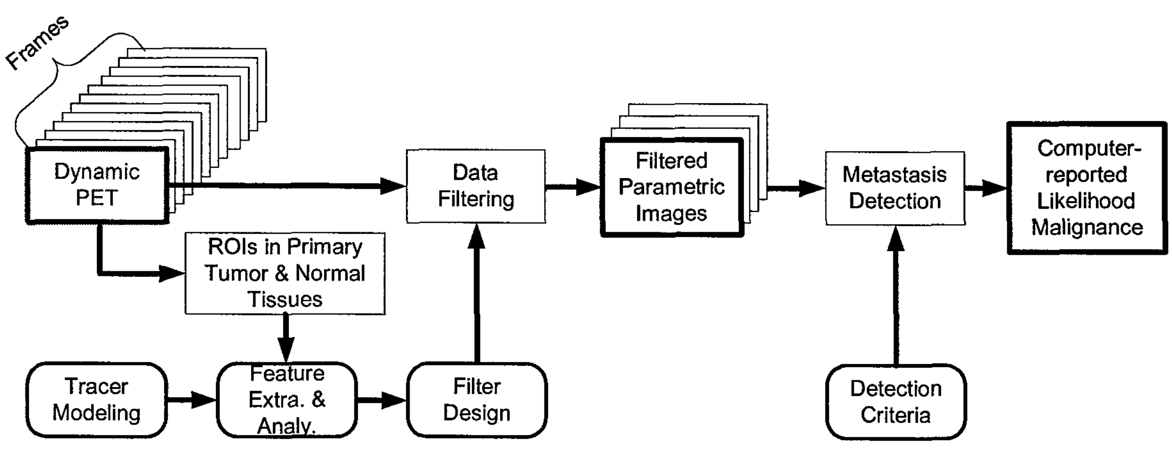

Figure 1: A diagram of the proposed IDEMMF system

2.1. Development of feature extraction and analysis

The feature extraction and analysis in dynamic PET images have been studied in both theory and practice. The intensive mathematical analysis has been performed based on the advanced FDG-PET kinetic modeling. The detailed analysis results can be found in Appendix A. The main improvements on the existing region of interest based techniques are briefly reported below.

2.1.1 TAC feature extraction

Using dynamic phantom data with known ground truth, we tested, to a certain degree, how the time activity curve in a large, visible lesion could be possibly interfered by its surrounding background activity (partial volume effect) [1,2, 4,6] through the currently used, imperfect reconstruction techniques and how the accuracy of lesion feature related parameters might be affected by the common ROI-averaged time activity curve.

We have performed an experimental study with a realistic liver phantom. In the liver phantom *three* artificial spherical lesions of different sizes and contrasts were placed inserted into the. Two tracers, ^{11}C and ^{18}F, were filled into the liver and lesions, respectively, with uniform activity distributions. Dynamic data were acquired of the phantom with ECAT953 2-D whole body scanner. This allowed the radioactive decay signature of the two radiopharmaceuticals to be measured as pseudo-washout data. In the filtered backprojection reconstructed images, the smallest lesion with 7mm interior diameters was invisible in all dynamic frames, while the two largest lesions can be clearly visualized in the FBP images, see Figure 2 (a) – (d) for an illustration.

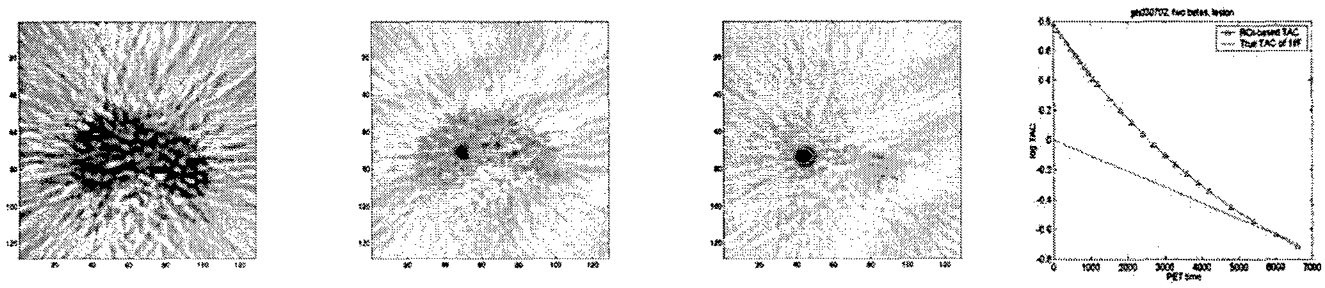

(a) (b) (c) (d)

Figure 2: (a) –(c) The last frame FBP images of the smallest, median, and largest lesions in the liver phantom; (d) The time activity curves in semi-log scale: true mono-exponential function of ^{18}F (red) and ROI averaged observation.

The largest lesion was used to mimic a primary tumor detected in a patient. A ROI was placed in it indicated in red in Figure 2 (c). The time activity curve in the lesion was estimated by fitting an ROI averaged observation. The resulting curve is plotted in semi-log scale and shown in Figure 2 (d). As we can see that the estimated curve in blue is far from the true ^{18}F time activity curve. The true curve should be a mono-exponential function and a straight line in semi-log scale. Evidently, the estimated features in lesion were severely contaminated by the activities of ^{11}C in the liver background. These features can not adequately characterize lesions. If we use these inaccurate lesion features to guide a filter design, then at an attempt to protect the lesion features during the filtering, we also vulnerably keep the unwanted background interference. This will definitely affect the performance of filtering and lower the SNR gain in the filtered images.

2.1.2 Non-invasive blood input function extraction

Blood input function is required in molecular feature extraction with FDG PET time activity models [1, 8,9]. We have also assessed the feasibility of replacing invasive blood sampling with non-invasive blood time activity curve extracted from dynamic image data. The most common way to get blood function is invasive blood drawing; however, operationally it is complicated, time consuming, and difficult for patients to have arterial blood draws throughout the procedure. A critical issue with the non-invasive approaches is their "ACCURACY". This is because, besides noise interference, the blood function is often interfered also by surrounding tissues. There are two non-invasive approaches available: one is a simple ROI based analysis and the other is the more complex FADS, or factor analysis of dynamic structure method. FADS is well known for its capability to separate time activity curves from the mixed observations.

Ten lung cancer and inflammation patient data were collected for the study. The blood samples were invasively collected from all these patients. These blood samples served as gold standard in the evaluation.

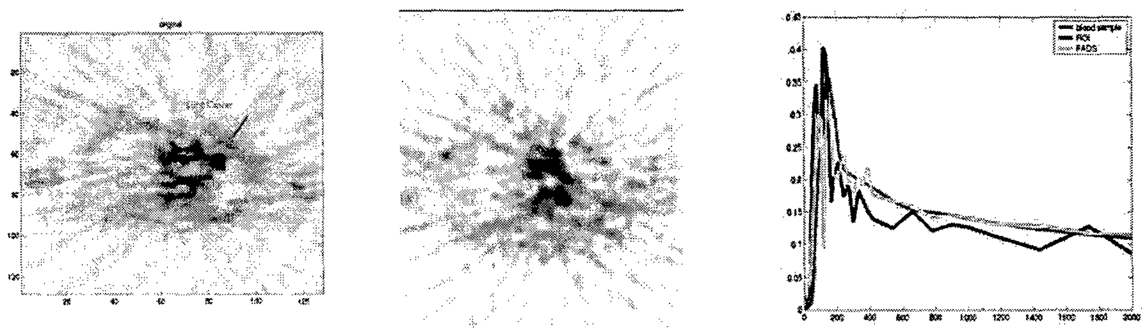

(a) (b) (c)

Figure 3: (a) The last frame FBP image of a lung cancer patient; (b) The ROI used to non-invasively extract arterial blood function; (c) The three blood functions: invasive blood samples (red), FADS estimation (green) and ROI-average (blue).

This study over 10 patients concludes that when compared to invasively collected blood samples, the blood functions estimated from FDAS have the mean square errors about 7 times lower than those of ROI average method. FADS approach is potential to outperform ROI-based method for replacing the invasive blood sampling. One example is shown in Figure 3.

FADS processing is widely used in cleaning up the surrounding background time activity interferences in the blood function non-invasively extracted in dynamic images at an area with strong arterial activity. Our study found out that FADS processed blood input functions has much more fidelity to the invasively collected blood samples in patients, but, on the other hand, we have also found that FADS processing failed to remove the interferences superimposed on the invisible artificial lesions in both experimental and digital phantom studies due to low lesion-to-background ratios. Consider the detected primary tumor and the normal tissues in properly selected areas are usually strong that are analogous to the scenario of blood function extraction. Thus, we will resort to FADS processing to separate the unwanted time activities contributed from surrounding background from the observed time activities in the primary tumor and normal tissues. The feature parameters will be estimated from the FADS resulted TACs, instead from that simply averaged in ROI.

2.2 Development of filtering and detection algorithms

Two types of filtering and detection algorithms have been developed which exploit the differences between normal and malignant tissues explored in the feature analysis. The details are reported in Appendices A and B and [8] [9].

2.3. Evaluation of spatial-temporal image processing

2.3.1 Evaluation via experimental phantom

Can adding temporal information to spatial processing improve SNR in small, faint or invisible lesions? This is a critical question that this study attempted to answer. We conducted the studies with both the digital (computer generated) phantom and the liver experimental phantom data that we believe would shed light upon answering the question.

The above-mentioned liver phantom shown in Figure 2 was used to test in gaining SNR in the smallest lesion through spatial-temporal processing. Figure 4 (a) – (c) shows the FBP reconstructed images of this lesion at Frame 1, 15 and 23 and Figure 4 (d) is the MAP reconstruction of Frame 23. This confirms that the lesion is invisible in all the frames using either the simple or advanced reconstruction methods. In other words, by exploiting only the spatial information in the data can not improve SNR high enough to make the lesion become detectable. To further increase SNR in the smallest lesion, making a use of the intrinsic, temporal information available in PET dynamic data is pursuable. We first tried to apply FADS to separate or remove the liver background activities and statistical noise superimposed onto the lesion, since we knew that FADS is well credited in decomposing the mixed observation from visible structures.

Via FADS we projected the dynamic images into the principle components of the images, but in none of the decomposed images the lesion was distinguishable. In Figure 4 (e), the first two principle component images are presented as an illustration. This indicates that a direct application of FADS provides no answer to early metastasis detection, this is because when lesion components are too weak to be dominant components, the principle component based FADS would fail to separate them from the noise. Figure 4 (f) is the output result of the metastasis detection shown in Figure 1. The technical details are given in Appendix A. In this test data, the primary tumor features were extracted in the largest artificial lesion shown in Figure 2 (c) by a simple ROI average. Although the accuracy of ROI based feature extraction had been shown not high enough, the results of this study reveal that adding temporal information to image processing indeed has potential to increase SNR in small lesions, as long as the features in small and primary lesions are similar in certain degree.

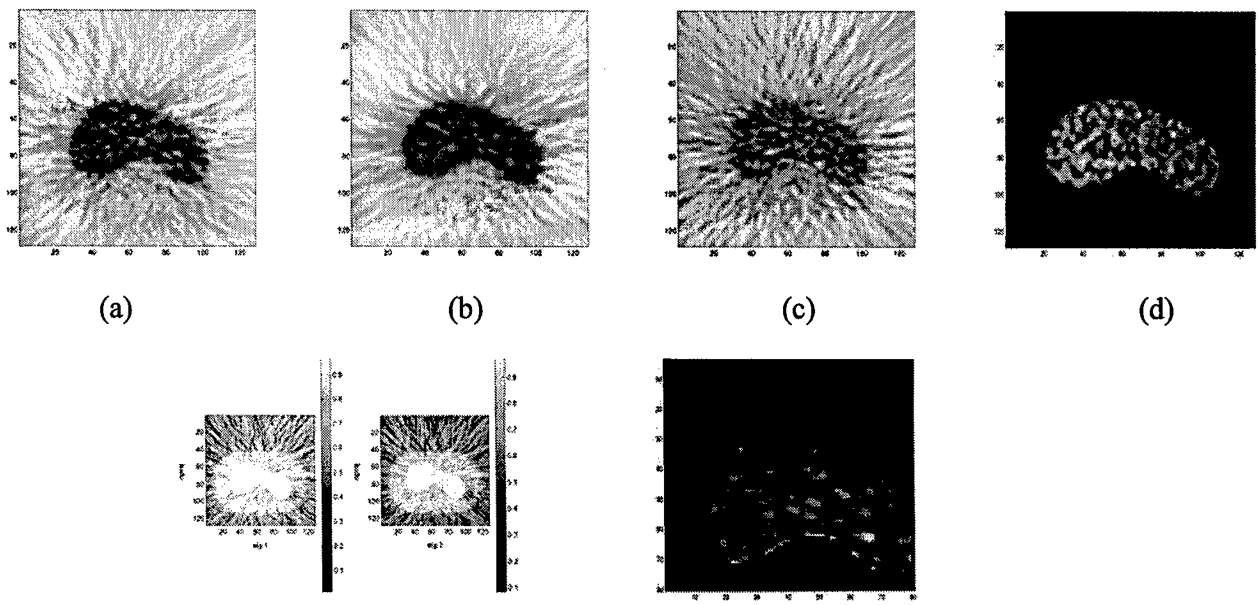

(a) (b) (c) (d)

(e) (f)

Figure 4: (a)-(c) FBP reconstruction of Frame 1,15 and 23; (b) MAP reconstruction of Frame 23; (c) FADS decomposed images; (d) filtered image using the simplest version of proposed methods.

2.3.2 Evaluation via ROC study with digital phantom study

The image of the digital phantom is shown in Figure 5 (a). There are five lesions in the ellipse. The lesions were assigned with the time activity curve collected in a proven lung metastatic malignant and the rest of the ellipse was assigned with the time activity curve in lung normal tissues, respectively. These curves are shown in Figure 5 (c). By forward projecting, the dynamic phantom sinogram data were generated and certain amount of Poisson noise was added to the projections. The noise energy level was controlled to make the lesions invisible in all the frames of FBP reconstructed images. The last frame of FBP reconstructed image with the highest SNR is presented in Figure 5 (b). None of the five lesions can be visualized as desired.

Assuming that the time activity curves in the lesions and the background are known in prior, we tested at each pixel whether the time activity curve observed is more similar to the lesion TAC or the background TAC in the sense of mean square errors. If at a pixel, the TAC observation is closer to the lesion TAC, then a lesion is detected at that pixel. Otherwise, the pixel is declared to be a normal tissue. 50 sets of dynamic phantom data were generated with/without adding digital lesions for a ROC study. The resulted ROC is given in Figure 5 (d). Although in reality the feature knowledge we know about lesion and normal tissues is not exactly the same as those in faint or invisible metastases, the resulting ROC demonstrates the potential to improve early metastasis detection from almost zero to 10% - 20%.

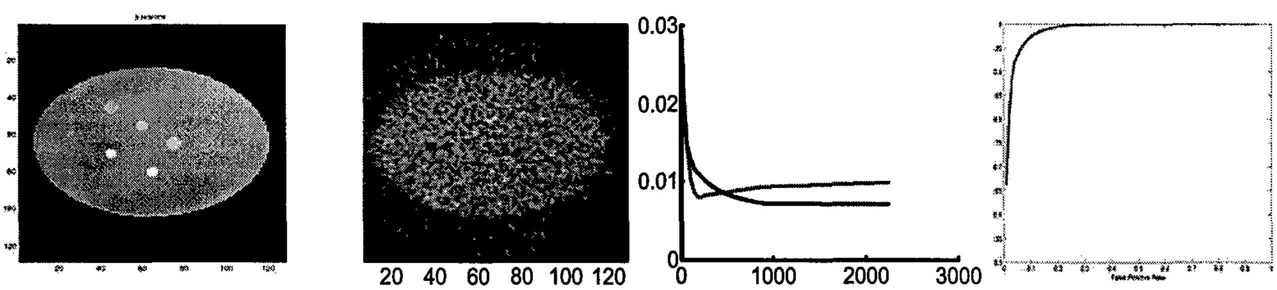

(a) (b) (c) (d)

Figure 5: (a) Digital phantom image; (b) FBP reconstructed image of (a); (c) Time activity curves assigned to lesions (red) and background (blue); (d) The measured ROC curve

2.3.3 Evaluation via animal study

We evaluated the proposed methods for early detection in vivo using animal study with a miniature PET scanner (microPET, Concorde Microsystems, Knoxville, TN). Primary tumors mimicking the molecular mechanisms of human cancer were implanted in mice subcutaneously.

The MDA-MB-435 human breast carcinoma cell line was used to grow primary tumors in the study. During the period of tumor formation, dynamic FDG microPET images of the mice were acquired to monitor the tumor growth at early stage on a multiple-day base. Three mammary fat mice were used. In order to assure the early stage to be captured, different number of cells (10^6, $0.5x10^6$ and $0.1x10^6$) were injected into the same mouse under the two arms. In this means, the rates of tumor growth should be different.

Dynamic PET imaging of FDG (200 uci) was performed on a MicroPET R4 system (Concorde MicroSystems, Inc). Six days after inoculation, thirty-five dynamic data frames were acquired for 1 hr after intravenous injection – 6x1sec, 4x3 sec, 10x30 sec, 5x60 sec, and 10x300 sec. Images were reconstructed with the OSEM algorithm, as shown in Figure 6 (a). The corresponding time-activity curves of the two tumors, normal tissues and heart have already been showed in Figure 6 (b). The blood input function was measured in the images at a selected ROI in the heart area. Figure 6 (c) is the transformed image of Figure 6 (a) after passing through the constraint temporal filter.

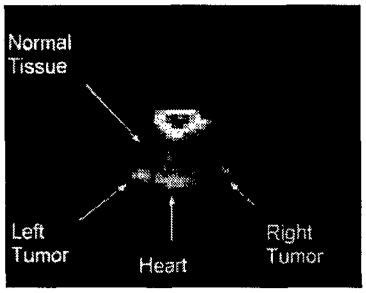

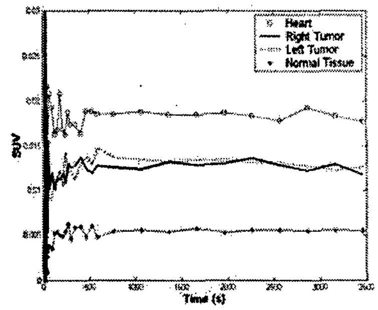

(a) (b)

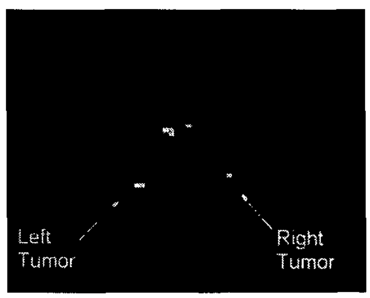

(c)

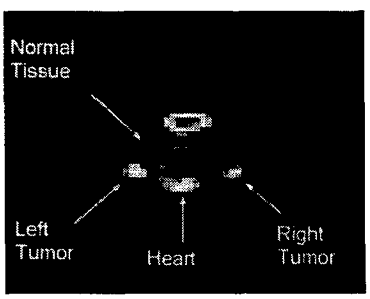

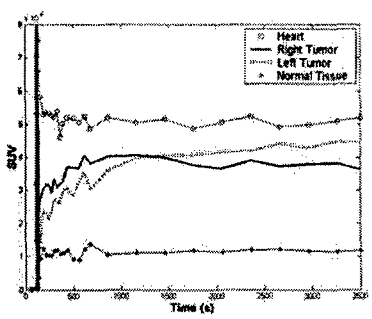

(d) (e)

Fig. 6. Animal study: (a) Reconstructed FDG-PET image (6 days after inoculation); (b) TACs drawn from (a); (c) processed image of (a) by using the constraint temporal filter; (d) Reconstructed FDG-PET image (12 days after inoculation); (e) TACs drawn from (d).

We also present another reconstructed image in Figure 6(d), which is acquired twelve days after inoculation. Figure 6(e) shows the corresponding TACs for the latterly acquired images. Comparing

Figure 6(a) and Figure 6(b), it demonstrate that the tumors grow bigger and the slope of tumor's TAC becomes steep after six more days. Using these facts, we confirmed that the findings in the filtered output image shown in Figure 6(c) were correct.

2.3.4 Evaluation via patient data

Patient study

Case of breast cancer: Fig. 7 (a) shows an FBP image of a breast cancer data archive without attenuation correction, in which only one small axillary metastasis can be visualized, indicated by an arrow. Attenuation corrected version of the same slice is shown in Fig. 7(b). Applying the primary tumor guided filtering, a method developed during this project, to the attenuation corrected dynamic images identified one extra metastasis as shown in Fig. 7(c). These positive findings have been confirmed by a follow-up study acquired 1.5 years later (the patient had no interval treatment of her primary or metastatic disease). See Figure 7 (d). Between the two studies no treatment was given and the disease progressed. Applying a threshold to the filtered image in Figure 7(c), the resulted detections are shown in Figure 7(e). Overlaying the filtered image in red to the follow-up image, Figure 7(f) demonstrates the computer identified metastases well aligned with those in the follow-up image. The slight misalignment between lesions and detections could be mitigated if an advancing registration accounting for non-rigid transformation was applied. Note that besides the two confirmed lesions, there are also some other pixels passing the threshold. This is because we only used a simple single pixel decision criterion. However, if we add the spatial size of lesions to be detected into the decision criterion, then we can get rid of the center parts in Figure 7(e). Moreover, the computer-generated likelihood of malignance will be reviewed by visual inspection. Combined with the additional knowledge of the patient's disease, the false positive findings in Figure 7(e) can be eliminated.

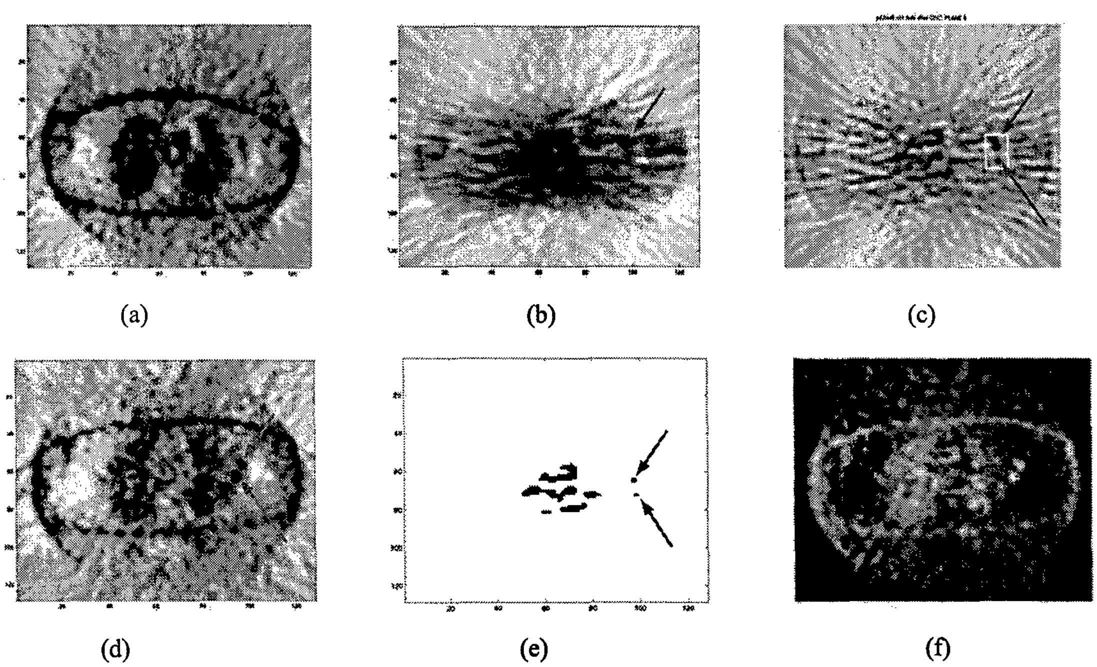

Figure 7: (a) FBP image of a breast cancer without attenuation correction; (b) Attenuation correction of (a); (c) the filtered image of (b); (d) the follow-up image after 1.5 years; (e) the detection by the computer observer; (f) the image of overlaying (e) on (d).

Cases of lung cancer and inflammation: The developed spatial temporal filtering guided with the features extracted on a patient by patient base has also been applied to differentiate between malignancy and inflammation. Figures 8(a) and (b) show a case of lung cancer and the corresponding filtering output image. Evidently the lesion was enhanced dramatically. As a contrast, Figure 9 presents a patient with lung cancer and joint inflammation where the joint is hot in the late frames of a dynamic PET scan. The simple, single template defined filter (mentioned in last annual report) was applied to process the data. We designed the filter using the physiological features extracted in a lung malignancy shown in Figure 8(a). In the filtered image, the "hot" spot caused by benign joint inflammation was filtered out the as normal tissue features. The result is shown in Fig. 9(b). This case demonstrates that the "hot" inflammation in FDGPET images may mislead visual inspection of static image, but with the feature guided spatial-temporal filtering, we can have a better chance to correctly distinct it from malignances.

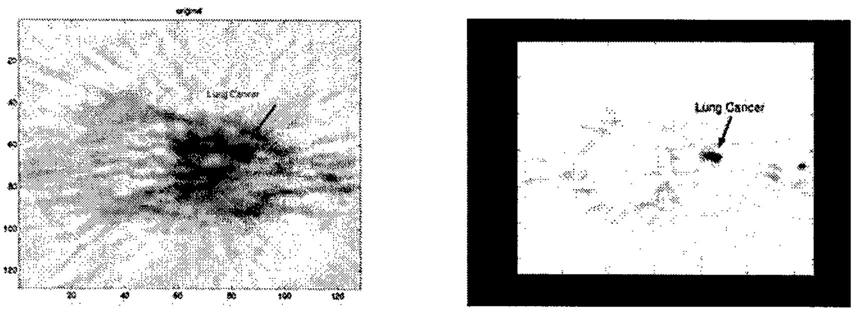

(a) (b)

Figure 8: A lung lesion

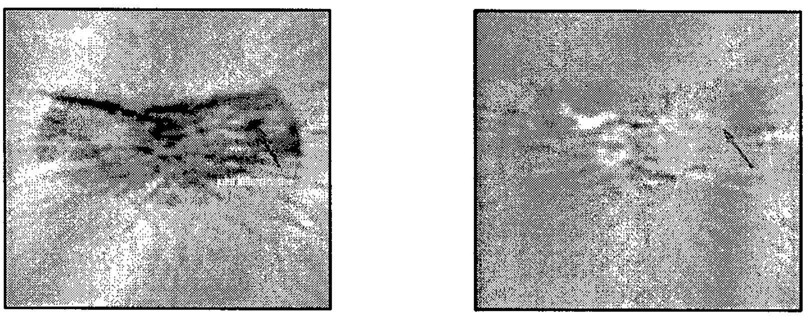

(a) (b)

Fig. 9: (a) Joint inflammation in a patient with lung cancer, and (b) Filtered dynamic image of the same slice

Remarks:

The three year grant was originally funded until July 31, 2002. However, after the first year's annual report, it was brought to our attention that we needed to obtain approval from both the U.S. Army Medical Research and Material Command Institutional Review Board (US Army IRB) for patient data collection, because although patients whose data to be used in this study will have a PET scan regardless of their participation in this study, they still must be prospectively recruited for "additional" (temporal-based) images. Since November 2000 the Army IRB had have a hold on the acquisition of the clinical data under this grant till May 2002; therefore, we had not obtained all of the data needed to complete the funded objectives.

We have requested a 24 month no-cost extension of the funding period for this project. As the US Army Medical Research Command was well aware of the delays with the clinical data, the request was proved. But due to a new PET/CT scanner purchased at the USC PET Clinical Center, the old PET scanner which has the capability to acquire dynamic scans had to be moved to and installed at our research facility, thus the task of acquiring 75 patients for performance analysis and evaluation for this project was not fully accomplished. For compensation, we added three groups of animal studies, each with 5 mice.

The major accomplishments of this activity are presented as follows:

3. Key Research Accomplishments

The main accomplishments of the project are

1. Explored temporal physiological differences in malignant and normal tissues based on the advanced FDG-PET kinetic modeling; mathematically mapped the physiological differences in temporal domain onto the kinetic (macro) parameter domain; revealed and analyzed such temporal or parametric differences in frequency domain and time-frequency domain;

2. Assessed the accuracy of ROI-based molecular feature extraction techniques with the real liver phantom data; developed the factor analysis aided feature extraction method to improve the accuracy of feature parameter estimation; evaluated the non-invasive blood input function extraction with clinically collected blood samples at the USC PET center;

3. Designed two space-temporal filtering and detection criteria to identify the early metastases embedded from the unwanted noise and background interference which exploit the physiological features in malignant and normal tissue observed in FDG-PET images;

4. Integrated the accomplishments and findings listed in Items 1 – 3 into a software prototype of Intelligent Detection of Early Metastasized Molecular Feature (IDEMMF) system, shown in Figure 1;

5. Assessed the IDEMMF system with digital or numerical phantom, experimental phantom, animal study and clinical study.

4. List of Reportable Outcomes:

4.1 Publications

1. C. C. Huang and X. Yu, ``A New Method of Computer-Aided Feature Identification for Lesion Detection in PET-FDG Dynamic Study", *IEEE Medical Imaging Conference* , Seattle, WA, November 1999.

2. X. Yu, C. C. Huang and P. S. Conti, ``Comparison of Kinetic Features Extracted in OSEM and FBP Reconstructed Dynamic PET Images for Oncology", *SNM Annual Conference*, San Louise, Mo., June 2000.

3. X. Yu and C. C. Huang, ``A Fast Method to Compute Covariance Matrix in Positron Emission Tomography Images", *IEEE Medical Imaging Conference* 2000.

4. C. C. Huang, ``Computer-Aided Lesion Detection in Positron Emission Tomography: A Signal Subspace Fitting Approach", Ph. D. Thesis, submitted to Electrical Engineering Department of USC, May 2001.

5. X. Yu, C. C. Huang and P. S. Conti, ``Assessment of ROI-based Time Activity Analyses in Dynamic PET For Oncology " SNM Annual Conference 2001, Toronto, Ca., June 2001.

6. X. Yu, Z. Li, H. Jadvar and P. S. Conti, ``Assessment of Non-invasive Blood Time Activity Extraction in Dynamic PET Oncology", SNM Annual Conference 2002, Los Angeles, CA., June 2002.

7. X. Yu, C. C. Huang, and P. S. Conti, ``Computer-aided Metastasis Detection with Dynamic PET", presented at the Era of Hope Conference, Orlando, FL., September 2002.

8. X. Yu, Z. Li, H. Jadvar and P. S. Conti, "Identification of Malignant and Benign Lesions in Dynamic PET Oncology", SNM Annual Conference 2003, New Orleans, San Louise, June 2003.

9. H. Jadvar, JR Bading and X Yu, PS Conti, "Dynamic FDG PET Kinetic Analysis of Inflammation and Cancer: Preliminary Results", SNM Annual Conference 2003, New Orleans, San Louise, June 2003.

10. J. Chen, X. Yu, "Enhanced Dynamic FDG-PET Tumor Detection with Constrained Temporal Filtering", Proceedings of IEEE International Conference on Medical Imaging, Portland, Or. October, 2003.

11. Z. Li, X. Yu, "Exploring Frequency Differences Of Physiological Processes To Enhance Dynamic FDG-PET", Proceedings of IEEE International Conference on Medical Imaging, Portland, Or. October, 2003.

12. J. Chen, X. Yu, "Rapid Assessment of PET Dynamic Images Using Computer Observers", Proceedings of IEEE International Symposium on Medical Imaging, October, 2004.

13. Z. Li, X. Yu, "Computer Aided Lesion Detection with Multi-channel Time-Frequency Analysis", Proceedings of IEEE International Conference on Medical Imaging, October, 2004.

14. X. Yu and I. S. Reed, "Theory and Algorithms of Rank Reduction for Subspace Filtering", amended submission to IEEE Trans. On Information Theory, December 2004

15. J. Chen and X. Yu, "Space-temporal Analysis and Processing of Dynamic PET Images", submitted to *IEEE Trans. On Information Technology in Biomedicine.*

16. Z. Li and X. Yu, "Exploring Physiological Differences in Time-Frequency Domain to Improve Tumor Detectability for Dynamic PET", submitted to *IEEE Trans. On Information Technology in Biomedicine.*

17. Z. Li, X. Yu, "Computer-aided Early Metastasis Detection in Dynamic Positron Emission Tomography", in preparation for submission to *IEEE Trans. On Medical Imaging Processing.*

4.2 Education Training and Graduation

Master Degree:

1. Chandhrasri, Swias, Electrical Engineering, January 1998 – May 2000
2. Tian, Ding, Electrical Engineering, September, 2000 – May 2002
3. Zheng, Jianchang, Computer Science, January 1996 – December 1997

Ph. D. Degree:

1. Huang, ChungChie, Electrical Engineering, September 1995 – December 1999
2. Thanyasrisung, Piyapong, Electrical Engineering, May 1996 – December 1997
3. Hu, ChiaChang, Electrical Engineering, September 1996 – May 1998
4. Saghari, Poorya, Electrical Engineering, September 2000 – May 2002
5. Chen, Jiansong, Electrical Engineering, September 2000 – Present
6. Li, Zheng, Electrical Engineering, January 2001 - Present

5. Conclusion

The goal of this project is to improve detection of metastatic axillary breast cancer through sophisticated physiological modeling and statistical signal processing techniques. The major focus of this project was to explore temporal physiological differences in malignant and normal tissues based on the advanced FDG-PET kinetic modeling assessment; assess and improve the accuracy of ROI-based molecular feature extraction techniques from the known primary breast tumor; design the space-temporal filtering and detection criteria to identify the early metastases from sever background interference and count noise; integrate the developed feature extraction and filtering/detection criteria into a software prototype of Intelligent Detection of Early Metastasized Molecular Feature (IDEMMF) system; and test and evaluate the prototype with phantom, animal study and clinical patient study. Our theoretical findings include mathematically map of the physiological differences in temporal domain onto the kinetic (macro) parameter domain; revealing and characterization of the temporal or parametric domain differences in frequency domain and time-frequency. The evaluations on a small scale of animal and patient data show that the IDEMME system can significantly enhance the metastatic lesion detection by exploring the temporal differences in dynamic FDG-PET images.

6. References

1. K. Schmidt, G. Mies, and L. Sokoloff, "Model of kinetic behavior deoxyglucose in heterogeneous tissues in brain: A reinterpretation of the significant of parameters fitted to homogeneous tissue models," J. Cerebral Blood Flow and Metabolism, Vol. 11, p. 10-24, 1991.

2. F. Osullivan, "Imaging radiotracer model parameters in PET: A mixture analysis approach", IEEE Trans. on Medical Imaging, Vol. 12, No. 3, pp. 399-412, 1993.

3. C. M. Kao, J. T. Yap, J. Mukherjee and M. N. Wernick, ``Image Reconstruction for Dynamic PET Based on Low-Order Approximation and Restoration of the Sinogram," IEEE Trans. Medical Imaging, Vol. 16, No. 6, Dec. 1997.

4. R. E. Carson, et al.,``An approximation formula for the variance of PET region-of-interest values," IEEE Trans. Med. Imag., Vol. 12, No. 2, p. 240-250, June 1993.

5. L.L. Scharf and B. Friedlander, "Matched subspace detectors", IEEE Trans. Signal Processing, Vol. 42, No. 8, p. 2146-2157, Aug. 1994.

6. R.H. Huesman, ``A new fast algorithm for the evaluation of regions of interest and statistical uncertainty in computed tomography," Phys. Med. Biol., Vol. 29, No 5, p. 543-552, 1984.

7. C. C. Huang, X. Yu, J. Bading and P. S. Conti, ``Feature extraction by subspace fitting of time activity curves in PET dynamic studies", IEEE Medical Imaging Conference, November 1997.

8. C.C. Huang, Ph.D. Thesis, submitted to USC EE department, May 2001.

9. P. Thanyasrisung, Ph.D. Thesis, submitted to USC EE department, May 2001.

APPENDIX A

Subspace Identification, Filtering and Detection: a New Approach for Lesion Detection in Dynamic FDG-PET

Zheng Li and Xiaoli Yu
Department of Electrical Engineering, Department of Radiology
University of Southern California
Los Angles, CA 90089-2565

January 17, 2005

Abstract

As with all nuclear medicine imaging technologies, lesion detection with positron emission tomography (PET) scanning of 2-[fluorine-18]-fluoro-2-deoxy-D-glucose (FDG)-labeled tissues is restricted by a relatively limited spatial resolution and a low signal-to-noise ratio, both rendering diagnosis by visual inspection difficult and potentially inaccurate. In this paper, a computer-aided lesion detection algorithm combined with the kinetic time activity curve (TAC) feature identification from the FDG-PET dynamic images is developed to assist visual inspection for lesion detection. We propose that the unique temporal and frequency TAC features available in dynamic FDG-PET images can be distinguishedly identified for normal and malignant tissues, then be usefully applied in statistical hypothesis tests to improve the detection of small lesions. The hypothesis is that, the TACs extracted from FDG-PET dynamic images may have variant shapes among tissues of different size and location within a given organ, but the sets of base functions weighted to compose the TACs which could be physiological process functions or wavelets base functions are invariant. Thus, our approach is based on using the linear invariant subspaces, defined as a span of a set of base functions, to model the lesion and normal tissue TAC features. The lesion and normal tissue subspaces, estimated from the known tissue types of data by the signal-subspace-fitting methods, are used for unknown lesion detection by applying a matched subspace detection criterion derived from a generalized likelihood ratio test. The experimental results using FDG-PET dynamic studies of cancer patients demonstrate that the identified TAC features are not only distinct and invariant for different tissue types of data, but also useful for discriminating lesions from normal tissues by incorporating a statistical hypothesis test. To quantitatively compare the sensitivity and specificity for different computer observers, a Monte Carol computer simulation of dynamic phantom images are simulated for achieving the receiver operating characteristic analysis.

1 Introduction

Positron emission tomography (PET), a rapidly developing technique for producing *in vivo* radiotracer distribution images, provides important physiological information. Non-invasive diagnostic procedures using PET imaging not only enable physicians to assess the metabolic activity of lesions *in vivo*, but also allow patients to avoid multiple costly procedures and to benefit from guided surgical intervention. PET scanning with 2-[fluorine-18]-fluoro-2-deoxy-D-glucose (FDG) is improving the diagnosis, staging, and treatment monitoring of a variety of human tumors [3, 22] and is becoming useful for the non-invasive diagnosis of cancer. However, as with all nuclear medicine imaging technologies, lesion detection with PET-FDG images is restricted by a relatively limited spatial resolution and a low signal-to-noise ratio, both rendering diagnosis by visual inspection difficult and potentially inaccurate, especially when the lesion diameter is small. Hence, computer-aided detection (CAD) algorithms, e.g., feature identification, have been developed to assist visual inspection in PET lesion detection. The difficulty is that spatial features such as the shape or contrast of a lesion in an image are often varied and difficult to identify [7, 8, 25]. Therefore, the PET dynamic data, providing the physiological information, becomes straightforward for feature identification [9].

The PET dynamic studies have been widely applied in medical images to estimate quantities, such as blood volume, flow, and local cerebral metabolic rates of glucose (LCMRGlc), etc [21, 16]. For example, by tracking how much glucose is metabolized in different areas of the body, PET-FDG imaging enables physicians to map glucose utilization. The compartmental models are usually used to quantitatively describe the tracer kinetic behaviors. Physiological factor analysis has been applied to the PET dynamic images to identify fundamental functions useful in the compartmental modeling of PET data [5]. Factor analysis of dynamic structures (FADS) was used to estimate the parameters of a compartment model [1]. Because FADS is used to solve an under-determined problem, there are an infinite number of sets of factors for possible solutions. A procedure called information-based factor analysis in dynamic structures (IBFADS) [14, 15] was introduced to incorporate a priori physiological information to reduce the error in the estimation of correct model. Information was added by using suitable mathematical models to describe the underlying physiological processes. Principal component analysis (PCA) [17] was introduced to enhance clinically interesting information in a PET dynamic imaging sequence in the first few principal component images, but it is a data-driving technique which can not separate signals from high noise level. A mixture model was introduced to estimate the parametric images with improved mean square error performance and low computational complexity [16]. The purpose of this paper is to extend the use the PET-FDG dynamic study for lesion detection which is based on a statistical parametric imaging. We propose that the unique spatial and temporal metabolic time activity curve (TAC) features available from PET-FDG dynamic images can not only be distinguishedly identified for normal and malignant tissues, but also be useful for improving small lesion detection by incorporating a statistical hypothesis test.

From a physiological compartment model analysis, the PET-FDG dynamic study for a given tissue type can be interpreted by a homogeneous compartment model which is governed by a set of kinetic parameters describing the passage of administered tracer for this given tissue type. A homogeneous compartment is associated with a particular dynamic structure called a physiological factor, a fundamental TAC, or a subspace basis [16]. A PET image pixel is usually modeled to contain more than one physiological factor and is called a mixed pixel or a heterogeneous pixel. It is assumed that a heterogeneous pixel TAC is a mixture of a finite number of independent homogeneous compartments, hence, a pixel TAC is composed of a combination of the physiological factors which constitute a subspace. In this paper, we hypothesize that each (heterogeneous) tissue's kinetic behavior is governed by its own set of kinetic parameters, which suggests that TAC shapes may vary among different tumors within a given patient, but will occupy the same subspace provided they have the same kinetic model parameters. For example, malignancies can be distinguished from normal tissues on the basis of biologically determined radiotracer accumulation or loss rate. Because cancer cells divides rapidly, they metabolize glucose at a much higher rate than do most normal tissues, hence, tumors uptake FDG more avidly and their TACs often increase with time [11]. Therefore, it may be possible to use the invariant subspaces identified from visible, large lesions to confirm suspected, but not unequivocally identifiable, small lesions.

We use the linear invariant subspaces to model lesion and normal tissue TAC features. By forming the PET-FDG dynamic data into a temporal-spatial matrix, the lesion and normal tissue subspaces can be simply estimated by using the signal-subspace-fitting methods. The least squares error (LSE) algorithm is used for parametric subspace estimation; while the principle component decomposition is used for non-parametric subspace estimation. In order to utilize the identified subspaces, several statistical hypothesis tests are derived for unknown lesion detection. Both superimposed and replacement data models are used to characterize the observations of large lesions and small lesions. Based on these two hypothesized data model, the statistical tests are called the matched subspace detectors [19, 24] which can be derived from the generalized likelihood ratio test (GLRT) principle. The matched subspace detector is actually the extension of the rank-1 matched filter to the multi-rank filters. In this paper, both the rank-1 and the multi-rank GLRTs are derived for the lesion detection. The rank-1 GLRT was derived in [19] by assuming that pixels are uncorrelated spatially. Considering that image pixel values are not statistically uncorrelated because each count contributes to all pixel values [2], the rank-1 GLRT needs to add a pre-whitening procedure. The spatial covariance matrix required for the pre-whitening can be computed using the methods described in [2, 10]. In multi-rank GLRT approach, it is assumed that the spatial inter-pixel correlation in each frame has the same structure but different energy level.

In this paper, we will concentrate on the filtered backProjection (FBP) reconstructed images. The results from clinical PET-FDG dynamic studies show that the physiological features estimated from known tumors and normal tissues are distinct and invariant, and are valuable for improving lesion diagnosis by incorporating a statistical test. Finally, to quantitatively compare the sensitivity and sufficiency of different estimations, detections as well as reconstructions, a Monte Carol computer simulation of phantom dynamic images are simulated for achieving the receiver operating characteristic (ROC) analysis.

In Section II, the PET-FDG dynamic data modeling described by a three-compartment FDG model is used to define the FDG TAC. Then the subspace formation is introduced based on a heterogeneous pixel assumption. Section III presents the signal-subspace-fitting methods for the lesion and normal tissue subspace identification. A subspace refining method based on a subspace angle criterion is shown for improving the subspace separation. Section IV adapts and extends the GLRT for different assumptions of pixel correlation. The results of TAC feature identifications and statistical tests for lesion detection in both clinic and phantom dynamic data are presented in

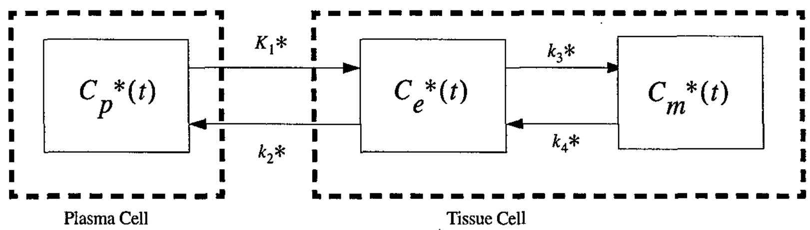

Figure 1: 4-k three compartment model. The left compartment is considered as the blood pool region and represents the concentration of FDG in the plasma. The middle compartment contains the FDG in tissue. The right compartment contains the phosphorylate FDG (FDG-6-P) in tissue.

Section V. Section IV is a conclusion.

2 Tracer Kinetics Modeling for Dynamic FDG-PET

In this paper, we will focus on FDG-PET dynamic studies because FDG is widely used as the tracer in clinical PET for lung and breast lesion detection. A 4-k three compartment model, one of most common type of model, is used to model the kinetic behavior of a time activity curve(TAC). Two cases, namely homogeneous tissue case and heterogeneous tissue case, will be discussed.

2.1 Homogeneous pixel: A 4-k Compartment Model

Under the homogeneous tissue assumption, the FDG tracer distribution in the tissue can be modeled by three compartments 4-k model (Figure 2.1). The rate constants are defined as

$$\begin{aligned}
K_1^* &= \text{the transport of FDG in plasma to tissue,} \\
k_2^* &= \text{the transport of FDG in tissue to plasma,} \\
k_3^* &= \text{the phosphorylation of FDG to FDG-6-P,} \\
k_4^* &= \text{the dephosphorylation of FDG-6-P to FDG.}
\end{aligned}$$

where $*$ indicates decay-corrected FDG tracer quantities.

It has been shown [21] that the radioactivity for a homogeneous tissue C_{tis} is:

$$\begin{aligned}
C_{tis}(t) &= \frac{K_1^*}{\beta_2 - \beta_1}[(k_3^* + k_4^* - \beta_1)\mathrm{e}^{-\beta_1 t} + (\beta_2 - k_3^* - k_4^*)\mathrm{e}^{-\beta_2 t}] \otimes C_p(t) \\
&= [M_1 \mathrm{e}^{-\beta_1 t} + M_2 \mathrm{e}^{-\beta_2 t}] \otimes C_p(t), \qquad (1)
\end{aligned}$$

where

$$
\begin{aligned}
\beta_1 &= \frac{1}{2}\left[(k_2^* + k_3^* + k_4^*) - \sqrt{(k_2^* + k_3^* + k_4^*)^2 - 4k_2^* k_4^*}\right], \\
\beta_2 &= \frac{1}{2}\left[(k_2^* + k_3^* + k_4^*) + \sqrt{(k_2^* + k_3^* + k_4^*)^2 - 4k_2^* k_4^*}\right], \\
M_1 &\triangleq \frac{K_1^*}{\beta_2 - \beta_1}(k_3^* + k_4^* - \beta_1), \\
M_2 &\triangleq \frac{K_1^*}{\beta_2 - \beta_1}(\beta_2 - k_3^* - k_4^*),
\end{aligned}
\tag{2}
$$

The total radioactivity measured by the PET scanner (under noise-free assumption), $C(t)$, including the radioactivity in the cerebral blood, can be represented as

$$
C(t) = V_b C_p(t) + C_{tis}(t) = V_b C_p(t) + [M_1 \mathrm{e}^{-\beta_1 t} + M_2 \mathrm{e}^{-\beta_2 t}] \otimes C_p(t), \tag{3}
$$

where V_b denotes the vascular space in tissue and FDG concentration in whole blood is assumed to be $V_b C_p(t)$ at time t [18].

2.2 A Heterogeneous pixel: a mixture model

Due to the limited spatial resolution of the PET scanner and the forward and backward processes in a PET system, the tissue concentration in a single pixel measured by the scanner is the mass-weighted average concentration of radioactivity in many the homogeneous tissues [12],[20]. Given that a mixed (heterogeneous) pixel contains $\bar{J}$ homogeneous subregions, from (3), $\bar{C}_{tis}(t)$, the weighted average radioactivity in a heterogeneous tissue can be written as:

$$
\bar{C}_{tis}(t) = \sum_{j=1}^{\bar{J}} w_j C_{tis\ j}(t) = \sum_{j=1}^{\bar{J}} w_j [M_{1j} \mathrm{e}^{-\beta_{1j} t} + M_{2j} \mathrm{e}^{-\beta_{2j} t}] \otimes C_p(t), \tag{4}
$$

where w_j is the weighting coefficient for the jth homogeneous subregion. Then, the total radioactivity measured by the PET scanner in a heterogeneous tissue, $\bar{C}(t)$, can be represented as:

$$
\begin{aligned}
\bar{C}(t) &= V_b C_p(t) + \bar{C}_{tis}(t) \\
&= V_b C_p(t) + \sum_{j=1}^{\bar{J}} w_j [M_{1j} \mathrm{e}^{-\beta_{1j} t} + M_{2j} \mathrm{e}^{-\beta_{2j} t}] \otimes C_p(t)
\end{aligned}
\tag{5}
$$

Notice that $C_p(t) = C_p(t) \otimes \delta(t) \approx C_p(t) \otimes \beta e^{-\beta t}$ when $\beta \to \infty$. For real data, above approximation works well when $\beta \geq 10$. By this way, all terms in (5) are expressed as convolution of blood input function with a exponential function. Combining some constant terms and rearranging the subscript j, (5) can be rewritten as:

$$\bar{C}(t) = \sum_{j=1}^{J} \alpha_j e^{-\beta_j t} \otimes C_p(t) \tag{6}$$

where α_j and J are determined by M_{1j}, $M_2 j$, w_j, V_b and $\bar{J}$. (6) is the general format to model the TAC measured by PET scanner, while (3) can be regarded as a special case ($\bar{J} = 1$) for it.

In all models listed above , the plasma input function $C_p(t)$ is considered as s given function. There are several techniques available to obtain this function: 1) normalized population-based input function, 2) invasive arterial line sampling, 3) ROIs of aorta or large vessels.

3 Time-Frequency Properties of TAC and Signal Subspaces for TAC

The FDG malignant (tumor) cell, in general, demonstrates steady increase in average standardized uptake values (SUV), while SUV in normal tissue decrease [29]. As a result, the observed TAC of malignant tissue increases with time, whereas, normal tissue TAC washouts with time [26]. This pattern is shown to be true in at least 80% of untreated primary cancers [29]. Figure 4.3 illustrates this temporal difference between clinical TACs drawn from the tumor and normal ROI. From this starting point, followed by some derivation of time-frequency properties, finally, it results in that the tumor and normal tissue's TAC belongs to two different signal subspaces.

In this section, we will first exploit the temporal difference in frequency domain to characterize the behaviors of the individual physiological process functions. Then, by decomposing the TACs into summation of physiological process functions or alternatively decomposing the TACs into summation of wavelet base functions, the time-frequency differences between the tumor and normal TACs are revealed. This differences imply that tumor and normal TACs can be approximated by different base function sets, which means the tumor and normal TACs belong to different signal subspaces.

3.1 Time Domain Properties of TAC

Define the physiological process function [27] $f(\beta, t)$ as:

$$f(\beta, t) = C_p(t) \otimes e^{-\beta t}, t \geq 0 \tag{7}$$

where $C_p(t)$ is the arterial blood input function, β is the decay coefficient. Since $C_p(t)$ is same for an individual patient, it's β value that affect the temporal properties of different $f(\beta, t)$. Before the further derivation, two constrains are added to $C_p(t)$ under the noise free assumption. First, $C_p(t)$ must be non-negative. i.e. $C_p(t) \geq 0, t \geq 0$; second, there exist a T_0 for each individual $C_p(t)$ such that $dC_p(t)/dt \geq 0,\ t \leq T_0$ while $dC_p(t)/dt < 0,\ t < T_0$ These constrains have been verified by a large patient popularity [28] as well as by plasma TAC model [4]. With these two constrains, we proved (Appendix) that for a given time $T, T > T_0$, there exists a threshold β^* in dynamic FDG-PET for each individual patient, such that the $\partial f(\beta, t)/\partial t|_{\beta=\beta^*, t=T} = 0$. Then for β value which satisfies $0 \leq \beta < \beta^*$, $\partial f(\beta, t)/\partial t|_{T_0<t\leq T} > 0$, while for $\beta > \beta^*$, $\partial f(\beta, t)/\partial t|_{t=T} < 0$. Remind that physiological process function $f(\beta, t)$ for tumor cell will go up along with time while the normal cell's physiological process function $f(\beta, t)$ will go down with time. Combining with the temporal properties we just drawn above, we can conclude that $f(\beta, t)$ for tumor cell will have $\beta \leq \beta^*$; , while $f(\beta, t)$ for normal cell will have $\beta > \beta^*$.

Using (6) and (7), the TAC measured by PET scanner in the heterogeneous tissue $\bar{C}(t)$, can be modeled as:

$$\bar{C}(t) = \sum_{j=1}^{J} \alpha_j e^{-\beta_j t} \otimes C_p(t) = \sum_{j=1}^{J} \alpha_j f(\beta_j, t), \qquad t \geq 0 \tag{8}$$

When decomposing a TAC into the linear combination of many physiological process functions, we hypothesis that the physiological process functions with β smaller that β^* are associated to malignancy tissue, while the physiological functions with β bigger than β^* are related to normal tissue. So, the physiological process functions can be divided into two sets: $\{f(\beta, t)|\beta \leq \beta^*\}$ and $\{f(\beta, t)|\beta > \beta^*\}$. The first set forms a linear subspace in which tumor's TAC lies, the second set form a linear subspace in which normal tissue's TAC lies.

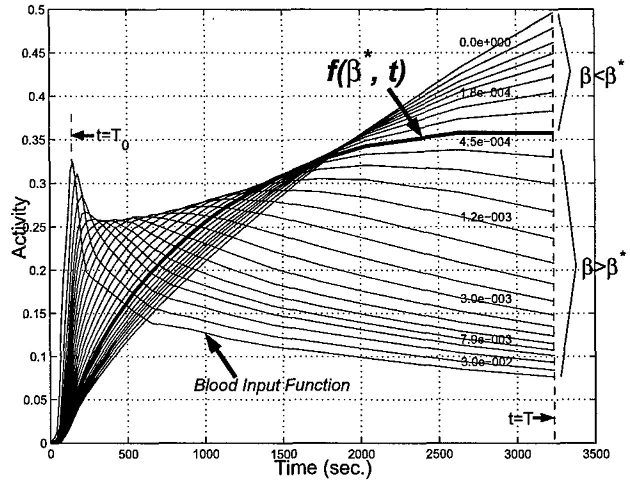

Figure 2: A bunch of the physiological process functions $f(\beta, t)$ when β varies from 0 to 1

3.2 Frequency Domain Properties of TAC

From the linear system point of view, a physiological function is the output of the arterial input function $C_p(t)$ passing through a linear time invariant system with impulse response:

$$h(\beta, t) = e^{-\beta t}, \quad t \geq 0 \tag{9}$$

Applying the Fourier Transform to the both sides of this equation (8):

$$\bar{C}(\omega) = \sum_{j=1}^{J} \alpha_j C_p(\omega) H(\beta_j, \omega) \tag{10}$$

where $C_p(\omega)$ is the Fourier Transform of blood function $C_p(t)$, $H(\beta_j, \omega)$ is the Fourier Transform of $h(\beta_j, t)$:

$$H(\beta, \omega) = 1/(\beta + j\omega), \quad |H(\beta, \omega)| = 1/\sqrt{\beta^2 + \omega^2} \tag{11}$$

Notice that the smaller the β, the lower the filter's bandwidth. So, for a certain patient (with a given blood input function), the physiological process function with smaller β contains less high frequency components than those with the larger β. Recall our hypothesis described in the previous subsection, (10)(11) indicates that the TAC in malignance has fewer high frequency components than that of normal tissue.

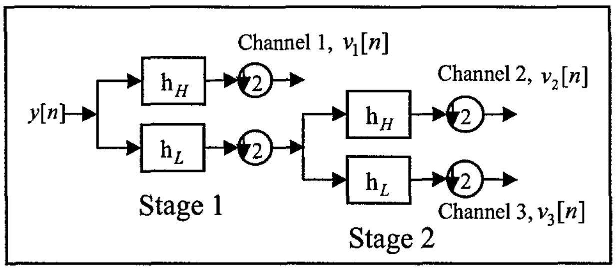

Figure 3: Two-stage wavelets analysis filter bank. $x[n]$ is the input signal, $v_i[n]$ is the output wavelet coefficients of channel i. h_L represents the lowpass subband filter, h_H represents the highpass subband filter.

3.3 Time-Frequency Domain Differences between Tumor and Normal TAC

In this section, the wavelet transformation will be employed so as we can get frequency domain information as well as short period time information. Further more, the wavelet transformation also provides an alternative way to express and identify the tumor and normal tissue's subspaces. The discrete-time wavelet analysis and synthesis, in vector format, can be written as:

$$\mathbf{v} = \mathbf{T_a y} \tag{12}$$

$$\mathbf{y} = \mathbf{T_s v} \tag{13}$$

where $\mathbf{y}$ is the input signal, $\mathbf{v}$ is the wavelet coefficients, $\mathbf{T_a}$ is the analysis matrix and $\mathbf{T_s}$ is the synthesis matrix whose columns are discrete-time wavelet base functions:

$$\mathbf{T_s} = [\psi_1, \psi_2, \ldots, \psi_k] \tag{14}$$

where $\psi_i, i = 1...k$ is the discrete-time wavelet base functions, k is the total number of base functions.

In practice, the discrete-time wavelet analysis can be implemented by subband linear filter bank[31]. Suppose $h_L[n]$ represents the low-pass subband filter, $h_H[n]$ represents the high-pass subband filter, $y[n]$ represents the input signal. Figure 3.3 illustrates a two-stage cascading structure of wavelet analysis. When passing a TAC through a multi-channel filter bank, the outputs of different channels represent the components in different frequency bands. The higher the stage, the lower the frequency. The outputs at the same channel carry the time information.

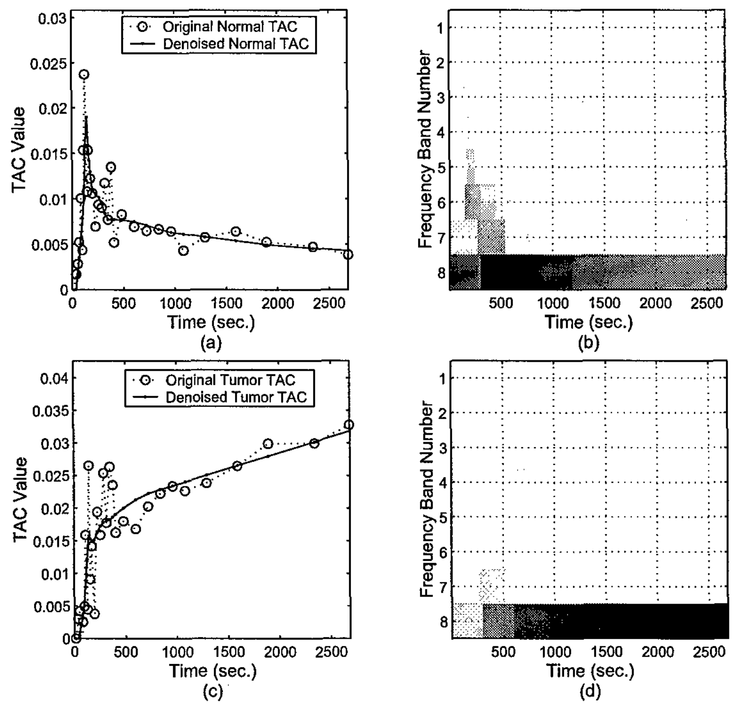

Figure 4: Wavelet tilings of noise free tumor and normal tissue's TAC. (a) clinical noisy TAC and denoised TAC for normal tissue. The denoise is done by model base least square curve fitting method. (b) wavelet tiling of denoised normal TAC. The X-axis represents the time. Y-axis represents the frequency band number, i.e. the channel number in the figure 3.3. The higher the channel number the lower the frequency band. (c) clinical noisy TAC and denoised TAC for tumor. (d) wavelet tiling of denoised tumor TAC.

Plotting the wavelet coefficients of a certain signal in 2D format, in which X axis represent the time and Y axis represent the frequency, we will get time-frequency "tiling" which shows the time-frequency distributions of that signal. Figure 3.3 illustrates the time-frequency tiling (the amplitudes of the coefficients are shown) of clinical normal and tumor TACs using wavelet analysis. It is shown that (i) tumor TAC has fewer high frequency components than that of normal tissue. (ii) energy of tumor TAC increases in the later time slots, while the energy of normal TAC decreases. These observed patterns of time-frequency tilings concord with the tumor and normal TACs' time domain and frequency domain properties derived before.

The purpose of involving the wavelet analysis here is to express the subspaces using wavelet base functions. According to (13) (14), the wavelet transformation can be regarded as the decomposition of the input signal to the weighted summation of independent wavelet base functions. The examples

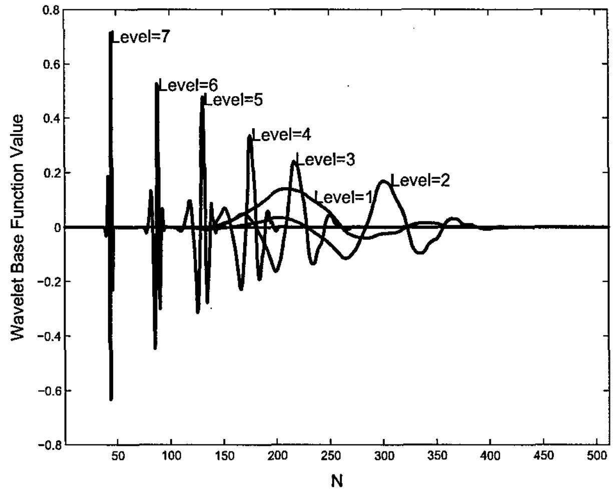

Figure 5: The Daubechies 4 wavelet base functions for 512 points seven levels filter bank. The base functions for different levels, i.e. for different frequency bands, are shown.

of base functions are shown in figure 3.3. The different patterns of time-frequency tilings between the noise free tumor and normal TACs imply that the tumor and normal TACs can be approximately expanded by different subset of wavelet base functions. In another word, the tumor and normal TACs belong to the different linear subspaces.

4 Subspace Formation and Identification

In this section, we first give a general formation of the subspaces, then two subspace identification methods are provided. The clinical studies show that our hypothesis of existence of tumor and normal tissue's subspaces is reasonable: the identified subspaces can express tumor and normal TACs accurately. Beside the two sets of base functions will be discussed, namely physiology process functions and wavelet base functions, the cubic B-splines, which are used in 4D continuous reconstruction, potentially could be used as the base functions. By this way, it prospectively can link the reconstruction process with tumor detection task.

4.1 The General Formation of Subspaces

The TAC received by the PET scanner with noise can be modeled as:

$$y(t) = \bar{C}(t) + n(t) = \sum_{i=1}^{\infty} a_i e_i(t) + n(t) \tag{15}$$

where $\{e_1(t), e_2(t), ...\}$ is a certain set of independent continuous base functions (without loss of generality, infinity number of base functions are used here. For real data, finite number of base functions should be accurate enough). After sampling this continuous signal at N time points, it becomes:

$$\mathbf{y} = \sum_{i=1}^{k} a_i \mathbf{e}_i + \mathbf{n} = \mathbf{E}\mathbf{a} + \mathbf{n}, \tag{16}$$

where $\mathbf{y}, \mathbf{e}_i, \mathbf{n} \in R^N$, $\mathbf{e}_i, i = 1, 2, ..., k$ are independent; $\mathbf{a} \triangleq [a_1, a_2, ..., a_k]' \in R^k$; $\mathbf{E} \triangleq [\mathbf{e}_1, \mathbf{e}_2, ..., \mathbf{e}_k]$ is a $N \times k$ matrix. Because $\{\mathbf{e}_1, \mathbf{e}_2, ..., \mathbf{e}_k\}$ is a set of base function defined on R^N, $k \leq N$ should be satisfied. The noise $\mathbf{n}$ is assumed to be additive Gaussian noise in this paper.

According to the subspace assumption we mentioned before, $span\{\mathbf{e}_1, \mathbf{e}_2, ..., \mathbf{e}_k\}$ is the union of two subspaces: one is the subspace for the pure tumor TAC, denoted by $\langle\mathbf{H}\rangle$; another is the subspace for the pure normal TAC, denoted by $\langle\mathbf{S}\rangle$:

$$\begin{aligned} \langle\mathbf{H}\rangle &\triangleq span\{\mathbf{e}_{i_1}, \mathbf{e}_{i_2}, ..., \mathbf{e}_{i_p}\}, \{i_1, i_2, ..., i_p\} \subset \{1, 2, ..., k\} \\ \langle\mathbf{S}\rangle &\triangleq span\{\mathbf{e}_{j_1}, \mathbf{e}_{j_2}, ..., \mathbf{e}_{j_q}\}, \{j_1, j_2, ..., j_q\} \subset \{1, 2, ..., k\} \end{aligned} \tag{17}$$

where p is the dimension of tumor's subspace and q is the dimension of normal tissue's subspace. $\langle\mathbf{H}\rangle$ and $\langle\mathbf{S}\rangle$ may have some base functions in common, but each of the subset must contain some base functions which are not included in another subset. Define matrix $\mathbf{H}$ and $\mathbf{S}$ as:

$$\begin{aligned} \mathbf{H} &\triangleq [\mathbf{e}_{i_1}, \mathbf{e}_{i_2}, ..., \mathbf{e}_{i_p}] \\ \mathbf{S} &\triangleq [\mathbf{e}_{j_1}, \mathbf{e}_{j_2}, ..., \mathbf{e}_{j_q}] \end{aligned} \tag{18}$$

According to (16) and (18), the noisy TAC $\mathbf{y}$ sampled from the normal tissue region and tumor region can be respectively modeled as:

$$H_0 \ (normal) \quad : \quad \mathbf{y} = \mathbf{S}\mathbf{a} + \mathbf{n} \tag{19}$$

$$H_1 \ (tumor) \quad : \quad \mathbf{y} = \mathbf{H}\mathbf{a} + \mathbf{n} \tag{20}$$

where $\mathbf{a} \in R^q$ for normal case, and $\mathbf{a} \in itR^p$ for tumor case.

4.2 Subspace Identification Methods

Given the P pixels tumor or normal tissue's region of interest(ROI) date, the subspace identification problem is to identify $\mathbf{H}$ or $\mathbf{S}$ respectively. Using (20)(20), the data model can be written as, for

P pixels tumor tissue's ROI data:

$$\mathbf{Y} = \mathbf{H}\mathbf{A} + \mathbf{N} \tag{21}$$

for P pixels normal tissue's ROI data:

$$\mathbf{Y} = \mathbf{S}\mathbf{A} + \mathbf{N} \tag{22}$$

where $\mathbf{Y} = [\mathbf{y}_1, \mathbf{y}_2, ..., \mathbf{y}_P]$, $\mathbf{A} = [\mathbf{a}_1, \mathbf{a}_2, ..., \mathbf{a}_P]$, $\mathbf{N} = [\mathbf{n}_1, \mathbf{n}_2, ..., \mathbf{n}_P]$. Because the identification problem is similar for tumor and normal tissue, only the case for tumor case is discussed.

4.2.1 Parametric : Least Squares Estimation (LSE)

For the tumor ROI data described in (21), the subspace fitting using the LSE is defined as [23]:

$$\hat{\mathbf{H}}, \hat{\mathbf{A}} = \arg\min_{\mathbf{H},\mathbf{A}} ||\mathbf{Y} - \mathbf{H}\mathbf{A}||_F^2, \tag{23}$$

where $||\cdot||_F$ denotes the Frobenius norm. It can be derived [23] that:

$$\hat{\mathbf{H}} = \arg\max_{\mathbf{H}} \mathrm{tr}\{\mathbf{P}_H \mathbf{Y}\mathbf{Y}^T \mathbf{P}_H^T\} \tag{24}$$

where $\mathbf{P}_H = \mathbf{H}(\mathbf{H}^\top\mathbf{H})^{-1}\mathbf{H}^\top$ is the orthogonal projection matrix that projects onto the column space of $\mathbf{H}$ and "tr" is the trace operator. When the measured blood function $C_p(t)$ is available, each column of $\mathbf{H}$ can be modeled using (6), otherwise (??)(6) will be used. By this way, the only unknowns in $\mathbf{H}$ are the exponential parameters β_j, so the LSE becomes to search the β_j over a reasonable range, i.e. $[0, 1]$ in this case(One β_j is corresponding to blood function and so as considered a known term). Newton-Raphson [30] or spectral analysis method [13] can be used to get the numerical solution for this problem.

4.2.2 Non-Parametric: Wavelet Transformation Method

Wavelet based subspace identification procedure includes three steps. First, using synthesis filter bank (13) to compute the complete set of discrete-time wavelet base functions. Second, using analysis filter bank (12) to compute the mean value of wavelet coefficients $\mathbf{y}$ for TACs at the given P tumor pixels. Third, the base functions for p dimension subspace of the tumor are wavelet base functions with the first p most significant wavelet coefficients. So,

$$\hat{\mathbf{H}} = [\psi_{i_1}, \psi_{i_2}, ..., \psi_{i_p}] \tag{25}$$

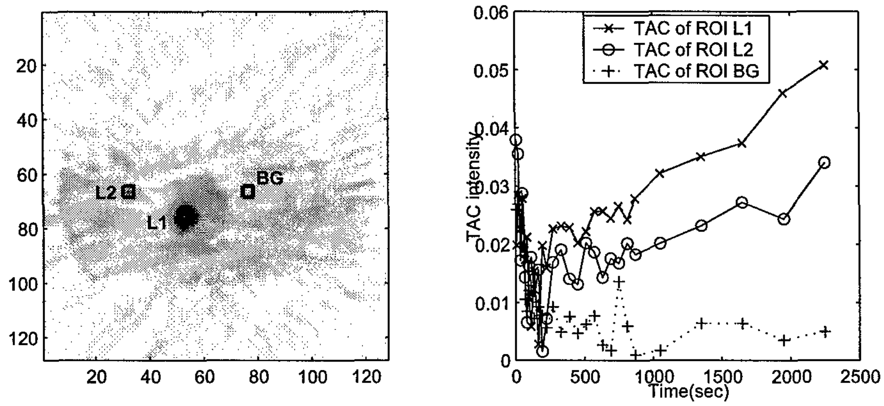

Figure 6: Clinic FBP reconstructed image and ROI TACs. (a) the last frame(28^{th}) of the PET-FDG dynamic FBP reconstructed images, where three 5×5 pixels ROIs are chosen: L1 in the large lesion (primary), L2 in the small lesion (metastasis) and BG in the background (normal). (b) the average TACs for ROI L1, ROI L2 and ROI BG respectively.

The subscripts $i_1, \dots, i_p$ are chosen such that $\mathbf{v}_{i_1}, \dots, \mathbf{v}_{i_p}$ are first p most significant values in $\mathbf{v}_i$, $i = 1...k$.

4.3 Subspace Identification Results

A clinical 28-frame PET-FDG dynamic study of lung cancer is shown here to verify our hypothesis about the existence of the subspaces and the subspace identification methods (The detailed information about the clinical data is listed in the next section). There are two lesions in this study, clearly visualized large tumor (primary) and another barely seen smaller tumor (metastasis). Figure 4.3 shows the clinic image and ROI TACs sampled from the image. Our clinical study shows the identified subspaces are accurate and separable.

Parametric LSE Method: The normal and tumor TAC's subspaces estimated by the LS method were found to be spanned by $\{e^{-\theta_1 t}, e^{-\theta_2 t}, e^{-\theta_3 t}\}$ and $\{1 - e^{-\beta_1 t}, e^{-\beta_2 t}, te^{-\beta_3 t}\}$, respectively, and the parameter sets were $\{\theta_1 = 0.00025,\ \theta_2 = 0.005,\ \theta_3 = 0.05\}$ and $\{\beta_1 = 0.005,\ \beta_2 = 0.0223,\ \beta_3 = 0.00125\}$ for BG and L1, respectively. Figure (??) show the curve fitting results using subspaces identified by LSE. Table (4.3) shows the curve fitting MSE. Both the figure and MSE show that the identified tumor subspace $\hat{\mathbf{H}}$ can fit tumor TAC well while fit normal TAC badly; the

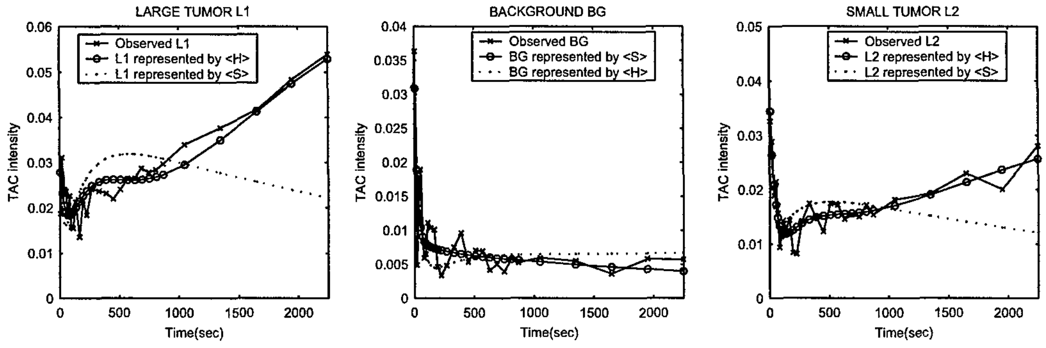

Figure 7: Comparison of accuracy and separability of extracted lesion and normal tissue's subspaces using least square estimation. The $\hat{\mathbf{H}}$ is estimated tumor's subspace using TAC data in L1, $\hat{\mathbf{S}}$ is estimated normal tissue's subspace using TAC data in BG. (*left*) TAC in L1 represented by the subspace $\hat{\mathbf{S}}$ and TAC in L1 represented by the subspace $\hat{\mathbf{H}}$. (*middle*) TAC in BG represented by the subspace $\hat{\mathbf{H}}$ and TAC in BG represented by the subspace $\hat{\mathbf{S}}$. (*right*) TAC in L2 represented by the subspace $\hat{\mathbf{H}}$ and TAC in L2 represented by the subspace $\hat{\mathbf{S}}$.

identified normal subspace $\hat{\mathbf{S}}$ can fit normal TAC well while fit tumor TAC badly. In one word, the identified subspaces are accurate and separable.

	L1 TAC	L2 TAC	BG TAC
$<\hat{\mathbf{H}}>$	0.0197	0.0123	0.0226
$<\hat{\mathbf{S}}>$	0.0536	0.0266	0.0195

Table 1: Curving fitting MSE for different TACs. The subspaces $<\hat{\mathbf{H}}>$ and $<\hat{\mathbf{S}}>$ are estimated by LSE

Non-Parametric Wavelet Transformation Method: The equations (12)(??) (25) and the base functions choosing criteria are applied. Setting $p = 8$, $q = 12$, the base functions for tumor and normal subspaces are illustrated in Figure 4.3. Figure 4.3 shows the curve fitting results using subspaces identified by wavelet method. Table (4.3) shows the curve fitting MSE.

The results from both methods show that the estimated subspaces $\hat{\mathbf{S}}$ and $\hat{\mathbf{H}}$ can respectively represent the normal and lesion TAC very accurately (with small MSE). At the same time, $\hat{\mathbf{S}}$ and $\hat{\mathbf{H}}$ are separable: $\hat{\mathbf{S}}$ can not represent the tumor TAC accurately (with large MSE) and $\hat{\mathbf{H}}$ can not represent normal TAC accurately.

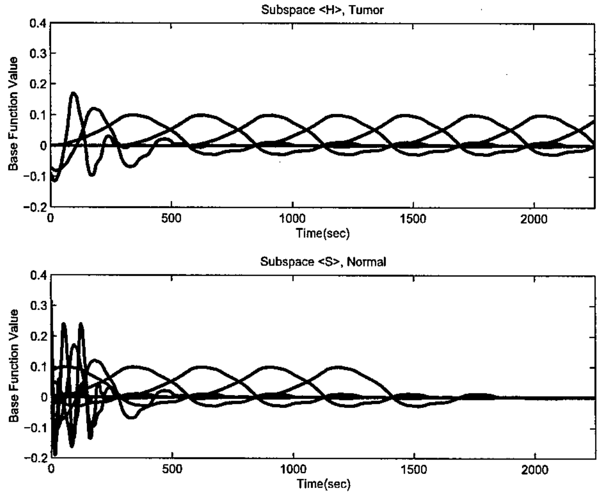

Figure 8: The tumor subspaces $\langle H \rangle$ and normal subspace$\langle S \rangle$ extracted using wavelet method

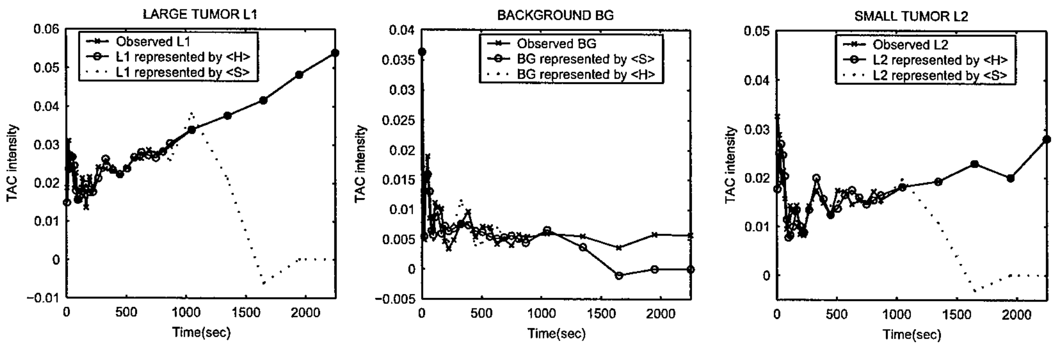

Figure 9: Comparison of accuracy and separability of extracted lesion and normal tissue's subspaces using wavelet method. The $\hat{\mathbf{H}}$ is estimated tumor's subspace using TAC data in L1, $\hat{\mathbf{S}}$ is estimated normal tissue's subspace using TAC data in BG. Notice that some estimated TAC overlap with the patient TAC. (*left*) TAC in L1 represented by the subspace $\hat{\mathbf{S}}$ and TAC in L1 represented by the subspace $\hat{\mathbf{H}}$. (*middle*) TAC in BG represented by the subspace $\hat{\mathbf{H}}$ and TAC in BG represented by the subspace $\hat{\mathbf{S}}$. (*right*) TAC in L2 represented by the subspace $\hat{\mathbf{S}}$ and TAC in L2 represented by the subspace $\hat{\mathbf{H}}$.

	L1 TAC	L2 TAC	BG TAC
$<\hat{\mathbf{H}}>$	0.0154	0.0208	0.0296
$<\hat{\mathbf{S}}>$	0.0887	0.0446	0.0134

Table 2: Curving fitting MSE for different TACs. The subspaces $<\hat{\mathbf{H}}>$ and $<\hat{\mathbf{S}}>$ are estimated by wavelet analysis method

5 Matched Subspace Detection

The generalized likelihood ratio test (GLRT) criterion is employed to solve the detection problem. By using the principle of the GLRT, the matched subspace detectors [19, 24] will be derived under two different assumptions of noise's time correlation and pixel's spatial correlation. The first one assumes that the pixel is uncorrelated spatially and the noise is white in time. The second one assumes the pixel is spatially correlated and noise is colored. For each of the detector, replacement data model and superimposed data model, are applied.

5.1 Hypothesized Data Model

Depending on modeling whether the lesion is mixed with surrounding normal tissue or not, two data models are used for the detection hypothesis.

Replacement Model: The lesion absence hypothesis H_0 says that the data consists of a sum of normal tissue signal $\mathbf{x}_0$ and the noise $\mathbf{n}_0$. The lesion existence hypothesis H_1 says that the data consist of a sum of lesion signal $\mathbf{x}_1$ and the noise $\mathbf{n}_1$. That is,

$$H_0 : \mathbf{y} = \mathbf{x}_0 + \mathbf{n}_0 \quad \text{and} \quad H_1 : \mathbf{y} = \mathbf{x}_1 + \mathbf{n}_1. \tag{26}$$

where $\mathbf{x}_1 = \mathbf{H}\theta$, $\theta \in \mathcal{R}^p$; $\mathbf{x}_0 = \mathbf{S}\phi$, $\phi \in \mathcal{R}^q$. $\mathbf{n_0}$ and $\mathbf{n_1}$ are additive Gaussian noise.

Superimposed Model: The lesion absence hypothesis H_0 is same as replacement model: the data consists of a sum of normal tissue signal $\mathbf{x}_0$ and the noise $\mathbf{n}_0$. The lesion existence hypothesis H_1 says that the data consist of a sum of lesion signal $\mathbf{x}_1$, normal tissue signal $\mathbf{x}_{01}$ (which means $\mathbf{x_{01}} \in \mathbf{S}$, but $\mathbf{x_{01}}$ may not be equal to $\mathbf{x_0}$) and the noise $\mathbf{n}_1$. That is,

$$H_0 : \mathbf{y} = \mathbf{x}_{00} + \mathbf{n}_0 \quad \text{and} \quad H_1 : \mathbf{y} = (\mathbf{x}_1 + \mathbf{x}_{01}) + \mathbf{n}_1, \tag{27}$$

where $\mathbf{x}_1 = \mathbf{H}\theta$, $\theta \in \mathcal{R}^p$; $\mathbf{x}_{00} = \mathbf{S}\phi_0$, $\phi_0 \in \mathcal{R}^q$; $\mathbf{x}_{01} = \mathbf{S}\phi_1$, $\phi_1 \in \mathcal{R}^q$. $\mathbf{n_0}$ and $\mathbf{n_1}$ are additive Gaussian noise.

5.2 Generalized Likelihood Ratio Test

Given hypothesis test with model:

$$H_0 : \mathbf{y} = \mathbf{x}_0 + \mathbf{n}_0 \quad \text{and} \quad H_1 : \mathbf{y} = \mathbf{x}_1 + \mathbf{n}_1. \tag{28}$$

The generalized likelihood ratio test is:

$$l(\mathbf{y}) = \frac{l(\hat{\mathbf{x}}_1|\mathbf{y})}{l(\hat{\mathbf{x}}_0|\mathbf{y})} \gtrless_{H_0}^{H_1} 0 \tag{29}$$

where $l(\cdot) \triangleq ln(p(\cdot))$, $p(\cdot)$ is the probability density function, $\hat{\mathbf{x}}_1$ and $\hat{\mathbf{x}}_0$ are maximum likelihood estimate(MLE) of $\mathbf{x}_1$ and $\mathbf{x}_0$ respectively.

5.3 Matched Subspace Detectors

Case 1: White Noise Without Spacial Correlation

For the replacement model defined in (26) with the assumption that the noise $\mathbf{n}_i$ is normal with zero mean and covariance matrix $\sigma_i^2\mathbf{I}$ and the signal $\mathbf{x}_i$ obey the linear subspace model $\mathbf{x}_1 = \mathbf{H}\boldsymbol{\theta}_1$ and $\mathbf{x}_0 = \mathbf{S}\boldsymbol{\theta}_0$. Using (29)[19]:

$$l_1(\mathbf{y}) = \frac{l(\hat{\theta}, \hat{\sigma}_1^2|\mathbf{y})}{l(\hat{\phi}, \hat{\sigma}_0^2|\mathbf{y})} = (\frac{\hat{\theta}_1^2}{\hat{\theta}_0^2})^{-N/2} exp\{-\frac{1}{2\hat{\theta}_1^2}||\hat{\mathbf{n}_1}||_2^2 + \frac{1}{2\hat{\theta}_0^2}||\hat{\mathbf{n}_0}||_2^2\}\frac{p(\theta, \sigma_1^2)}{p(\phi, \sigma_0^2)} \tag{30}$$

Substituting the MLE of σ_i, θ and ϕ into it, finally result in:

$$L_1(\mathbf{y}) = \frac{||\hat{\mathbf{n}}_0||_2^2}{||\hat{\mathbf{n}}_1||_2^2} = \frac{\mathbf{y}^\top \mathbf{P}_S^\perp \mathbf{y}}{\mathbf{y}^\top \mathbf{P}_H^\perp \mathbf{y}} \gtrless_{H_0}^{H_1} \eta_1 \tag{31}$$

where $\mathbf{P}_H^\perp$ is the orthogonal projection onto the complement subspace of $\langle\mathbf{H}\rangle$ and $\mathbf{P}_S^\perp$ is the orthogonal projection onto the complement subspace of $\langle\mathbf{S}\rangle$, which are defined as:

$$\begin{aligned} \mathbf{P}_S^\perp &= \mathbf{I} - \mathbf{S}(\mathbf{S}^\mathbf{T}\mathbf{S})^{-1}\mathbf{S}^\mathbf{T} \\ \mathbf{P}_H^\perp &= \mathbf{I} - \mathbf{H}(\mathbf{H}^\mathbf{T}\mathbf{H})^{-1}\mathbf{H}^\mathbf{T} \end{aligned} \tag{32}$$

Similarly, for the superimposed model defined in (27), the GLRT becomes [19]:

$$L_2(\mathbf{y}) = \frac{||\hat{\mathbf{n}}_0||_2^2}{||\hat{\mathbf{n}}_1||_2^2} = \frac{\mathbf{y}^\top \mathbf{P}_S^\perp \mathbf{y}}{\mathbf{y}^\top \mathbf{P}_{HS}^\perp \mathbf{y}} \gtrless_{H_0}^{H_1} \eta_2 \tag{33}$$

where $\mathbf{P}_{HS}^\perp$ is the orthogonal projection onto the complement subspace of $\langle\mathbf{HS}\rangle \triangleq \langle\mathbf{H}\rangle \bigcup \langle\mathbf{S}\rangle$, which is defined as:

$$\mathbf{P}_{HS}^\perp = \mathbf{I} - \mathbf{HS}(\mathbf{HS}^\mathbf{T}\mathbf{HS})^{-1}\mathbf{HS}^\mathbf{T} \tag{34}$$

Case 2: Colored Noise With Spacial Correlation

It is assumed that the spatial inter-pixel correlation in each frame has the same structure but different energy level. Let the P-dimensional vector $\mathbf{f}_i = [f_i(1), f_i(2), \cdots, f_i(P)]^\top$ denote the spatial pixel data for the i-th frame and denote $\mathbf{F} = [\mathbf{f}_1, \mathbf{f}_2, \cdots, \mathbf{f}_N]$. We assume that all the columns of the matrix $\mathbf{F}$ are independent. Hence $\mathbf{Y} \triangleq [\mathbf{y}_1, \mathbf{y}_2, \cdots, \mathbf{y}_P] = \mathbf{F}^\top$. The derivation of the multi-rank GLRT for the constrained correlation structure is based on a replacement model, i.e.,

$$\begin{cases} H_0 : \mathbf{Y} = \mathbf{X}_0 + \mathbf{N}_0, \\ H_1 : \mathbf{Y} = \mathbf{X}_1 + \mathbf{N}_1. \end{cases} \tag{35}$$

The GLRT can be derived as :

$$L_3(\mathbf{Y}) = \frac{1 + (\mathbf{G}^{-1/2}\mathbf{R}\tilde{\mathbf{s}})^\top \mathbf{P}_{\tilde{\mathbf{S}}}^\perp (\mathbf{G}^{-1/2}\mathbf{R}\tilde{\mathbf{s}})}{1 + (\mathbf{G}^{-1/2}\mathbf{R}\tilde{\mathbf{s}})^\top \mathbf{P}_{\tilde{\mathbf{H}}}^\perp (\mathbf{G}^{-1/2}\mathbf{R}\tilde{\mathbf{s}})} \gtrless_{H_0}^{H_1} \eta_3 \tag{36}$$

where $\mathbf{R}$ is the covariance matrix, $\mathbf{s} \triangleq \mathbf{M}^{-1/2}\mathbf{1}$, $\tilde{\mathbf{s}} \triangleq (\mathbf{s}^\top\mathbf{s})^{1/2}\mathbf{s}$,$\mathbf{G} \triangleq \mathbf{R}\mathbf{R}^\top - (\mathbf{R}\tilde{\mathbf{s}})(\mathbf{R}\tilde{\mathbf{s}})^\top$. The matrix $\mathbf{M}$ is the correlation structure for each frame.

6 Result and Discussion

Three categories of dynamic PET studies are involved to demonstrate our methods. Physical phantom study was designed to validate the efficacy of MSD for dynamic PET lesion detection. Digital phantom study and clinical study were designed to validate the subspace identification methods as well as MSD with estimated subspaces.

6.1 Dynamic PET Physical Phantom Study

Image Type	FBP Reconstructed Image	MAP Reconstructed Image
Original Reconstructed Image	1.55	1.62
MSD w/ Replacement Model	3.75	4.05

Table 3: Average Lesion to Background Contrasts for Physical Phantom Study

6.2 Dynamic FDG-PET Digital Phantom Study

The dynamic digital phantom is generated by passing an original noise free dynamic digital phantom through a forward projection and a backwards reconstruction. The noise free dynamic digital phantom, which simulates the anatomic structure of body containing heart, normal tissue and tumors, contains 28 frames of 128x128 pixel images. To mimic the clinical physiological process, all the TACs assigned to the digital phantom are obtained by the clinical FDG-PET studies. The

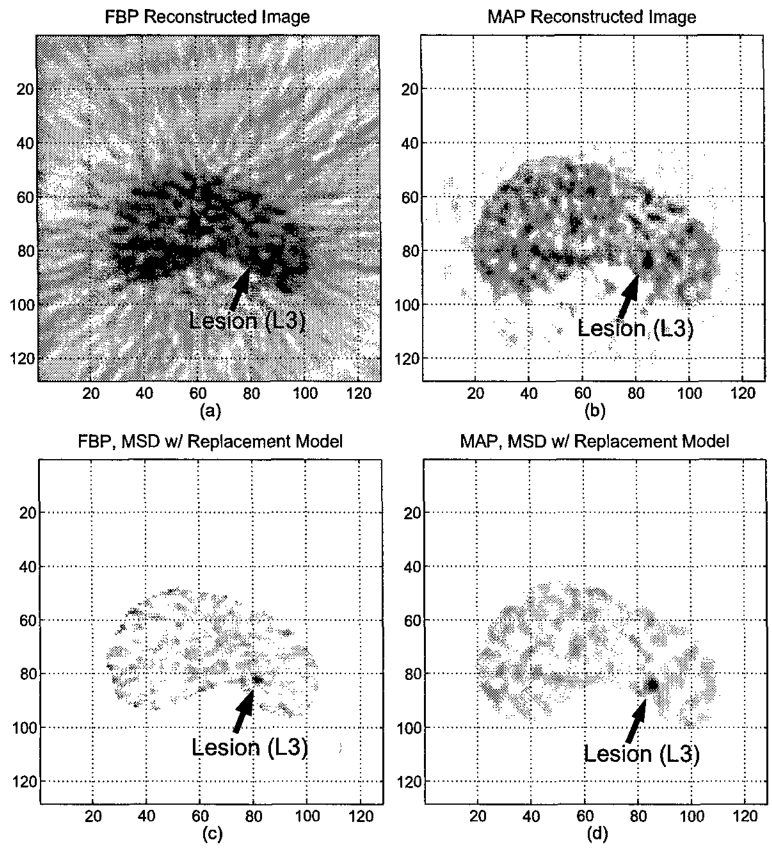

Figure 10: Physical phantom study. (a) FBP reconstructed image at last frame (b) MAP reconstructed image at last frame (c) Detection for FBP reconstructed image (d) Detection for MAP reconstructed image

measured blood function of one patient was used as the blood input function in the phantom. The TACs in the proven tumor and normal ROI of the same patient are extracted from the clinical images. Then based on the tracer dynamic model provided by (6), the parameters are estimated by spectral analysis method [13]. By this way, we can get low noise phantom TACs while mimic true clinic TACs very well (the TACs sampled from the clinical image, even after averaging, are with high noise). The computer simulated phantom at last frame was shown in Figure. 6.2(a).

When simulating the forward projection for the phantom image, the total count of sinagram in each frame was scaled to approach the total count for the corresponding frame in clinical dynamic study. Then the sinagram data was added with Possion noise and blurred for system resolution. FBP method is used for the reconstruction. Figure. 6.2(b) shows phantom dynamic image at the last frame.

The estimated lesion and normal subspace $\hat{\mathbf{H}}$ and $\hat{\mathbf{S}}$ were computed using TAC data sampled from a 5×5 ROI in upper lesion in noise free phantom. Parametric least square and non-parametric wavelet based methods were applied to identify subspaces. Replacement model and superimposed model based matched subspace detection algorithm were employed for detection. The output images are shown in Figure. 6.2 (c)(d)(e)(f). To calculate the average lesion to background contrast, mean lesion and background values were achieved by averaging the 5×5 lesion and background ROIs respectively. The results are listed in Table 6.2.

Image Type	**Upper Lesion**	**Lower Lesion**
Reconstructed Image	1.45	1.05
Replacement Model, LSE subspace	4.49	4.59
Replacement Model, wavelet subspace	5.01	4.62
Superimposed Model, LSE subspace	29.9	17.4
Superimposed Model, wavelet subspace	8.57	4.50

Table 4: Average Lesion to Background Contrasts for Digital Phantom Study

6.3 Clinic Dynamic PET-FDG Study

6.3.1 Protocol and Reconstruction of Dynamic PET-FDG Study

The clinical PET-FDG dynamic data was acquired with a Siemens/CTI ECAT Model 953A whole-body PET scanner. This device provides 31 contiguous transaxial image planes with an axial field

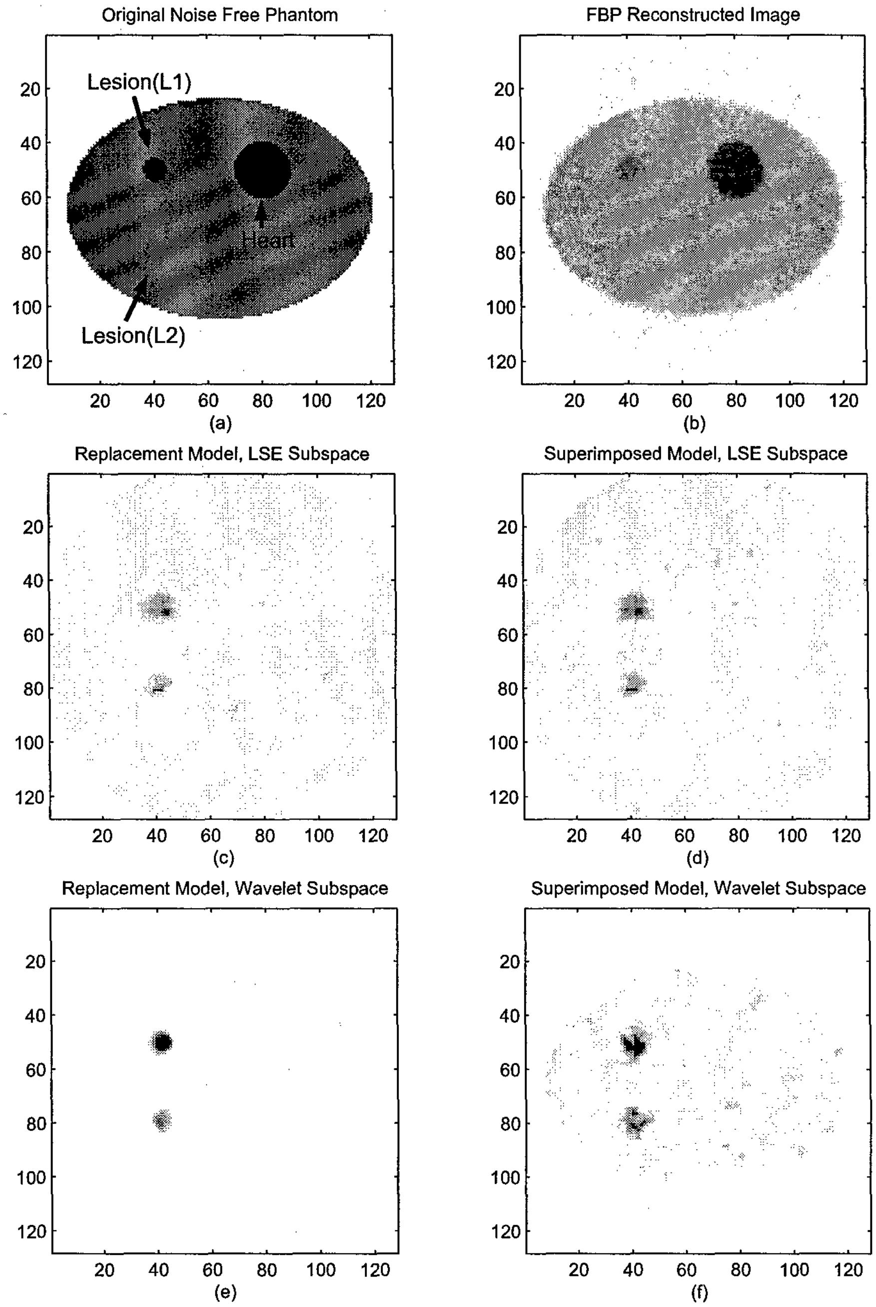

Figure 11: Digital phantom study. (a) original noise free dynamic phantom at last frame (b) FBP reconstruction dynamic phantom at the last frame. (c) detection based on replacement model, subspaces were estimated by LSE. (d) detection base on superimposed model, subspaces were estimated by LSE (e) detection base on replacement model, subspaces were estimated using wavelet method. (f) detection base on superimposed model, subspaces were estimated using wavelet method.

of view of 10.8 cm. The nominal intrinsic resolution of the system is 4 mm in all 3 dimensions. Consecutive detector rings are separated by tungsten septa in order to reduce scatter noise. Dynamic data will be acquired from 0 to 55 minute post injection. The dynamic structure protocol for the clinical data acquisition was listed in Table 1. Two reconstruction methods, namely FBP

Scan Type	**Scan Times**	**Frame Duration**
Dynamic scan	0 - 2 min	15 sec/frame
Dynamic scan	3 - 5 min	30 sec/frame
Dynamic scan	6 - 25 min	1 min/frame
Dynamic scan	26 - 45 min	5 min/frame

Table 5: Dynamic Data Acquisition Protocol

and MAP reconstruction, were used in our clinical studies.

6.3.2 Clinical Lung Cancer Study

The image contains one confirmed primary tumor and one confirmed metastatic lymph node, which is shown in Figure 6.3.2 (a) and (b). $\hat{\mathbf{H}}$ and $\hat{\mathbf{S}}$ are estimated using 5×5 ROI date in the primary tumor region. Substituting the $\hat{\mathbf{H}}$ and $\hat{\mathbf{S}}$ estimated by LSE and wavelet methods into (31), finally result in the output images shown in Figure 6.3.2 (c)(d)(e)(f). Notice that only replacement model based methods are employed in clinical data study. Because for clinical data we have tried, superimpose model based methods always get worse result comparing to replacement model. This problem will be explained in the discussion section. The average metastasis to background contrasts are listed in Table 6.3.2. To calculate the mean contrast, mean metastasis values were achieved by averaging the 3×3 ROI centered at the confirmed metastasis region, while mean background values were achieved by averaging whole body's region(not the whole image).

6.3.3 Clinical Breast Cancer Study

The detection procedures are same as the lung cancer case, two breast cancer images at different planes are tested: one for the primary tumor, another for metastatic lymph node. The original clinic images and all output images are shown in Figure 6.3.3 and Figure 6.3.3. The average metastasis to background contrasts are listed in Table 6.3.2.

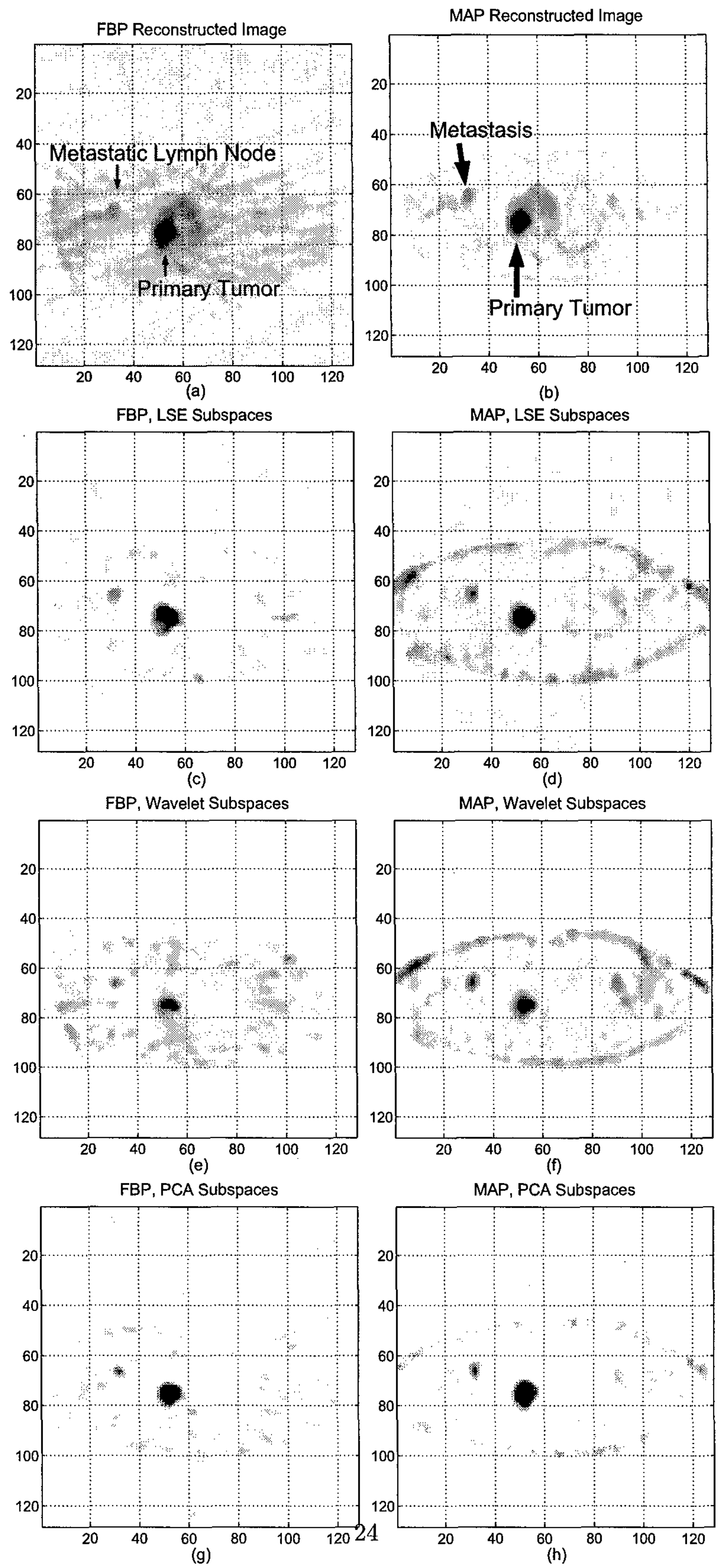

Figure 12: Clinic lung cancer study. (a) FBP reconstructed image at last frame (b) MAP reconstructed image at last frame (c) Detection for FBP reconstructed image, subspaces were estimated by LSE (d) Detection for MAP reconstructed image, subspaces were estimated by LSE (e) Detection for FBP reconstructed image, subspaces were estimated by Wavelet method (f) Detection for MAP reconstructed image, subspaces were estimated by Wavelet method

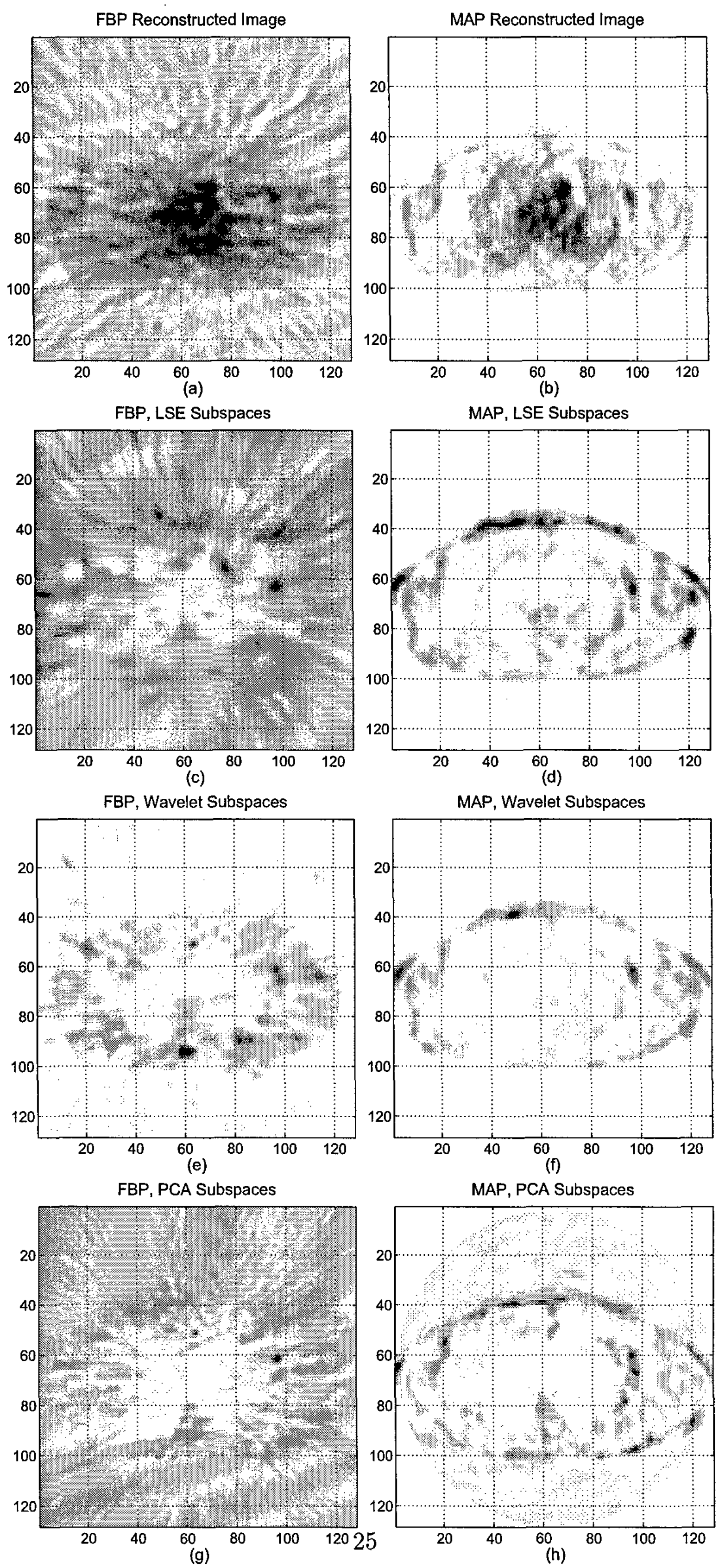

Figure 13: Clinic breast cancer study. (a) FBP reconstructed image at last frame (b) MAP reconstructed image at last frame (c) Detection for FBP reconstructed image, subspaces were estimated by LSE (d) Detection for MAP reconstructed image, subspaces were estimated by LSE (e) Detection for FBP reconstructed image, subspaces were estimated by Wavelet method (f) Detection for MAP reconstructed image, subspaces were estimated by Wavelet method

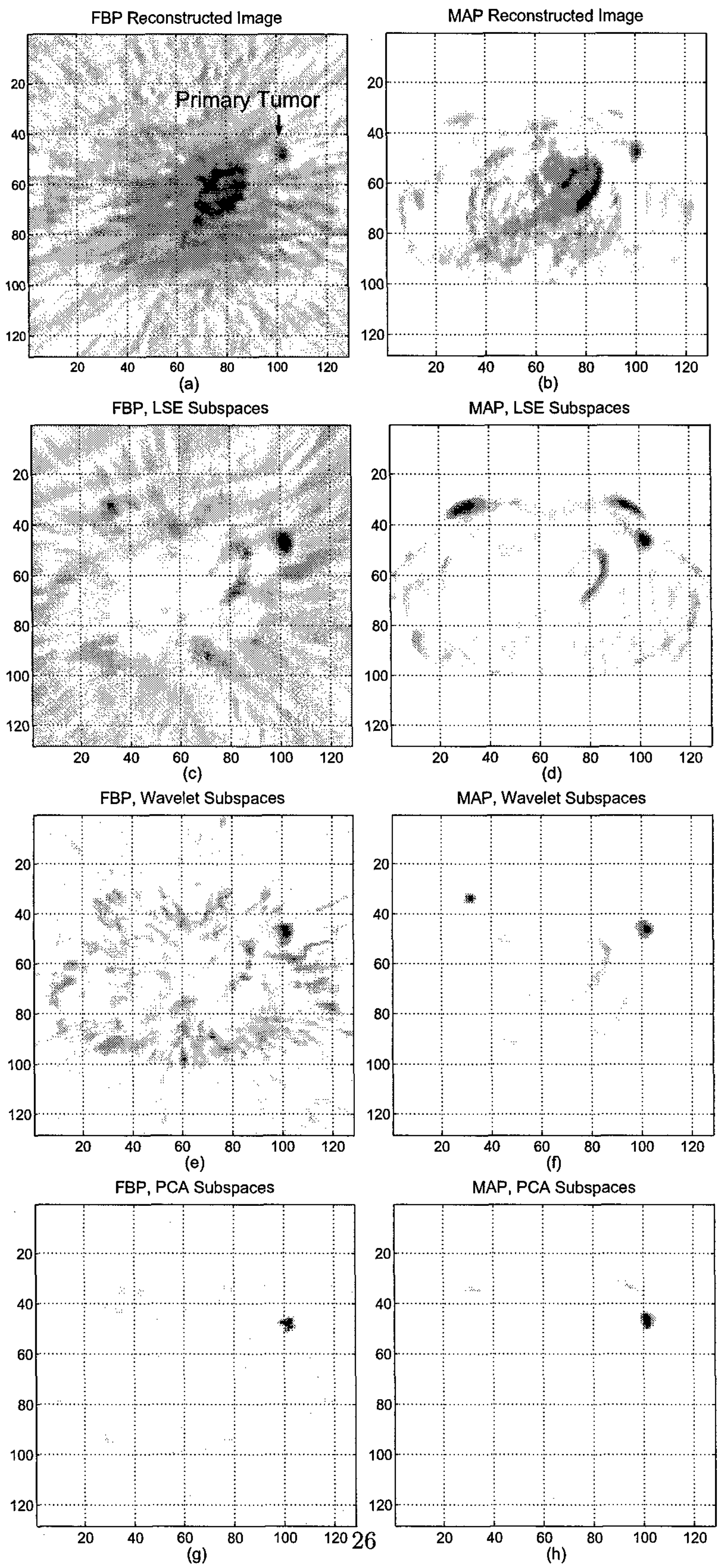

Figure 14: Clinic breast cancer study. (a) FBP reconstructed image at last frame (b) MAP reconstructed image at last frame (c) Detection for FBP reconstructed image, subspaces were estimated by LSE (d) Detection for MAP reconstructed image, subspaces were estimated by LSE (e) Detection for FBP reconstructed image, subspaces were estimated by Wavelet method (f) Detection for MAP reconstructed image, subspaces were estimated by Wavelet method

Image Type	Lung Metastasis	Breast Metastasis
FBP Reconstructed Image	2.67	2.03
MAP Reconstructed Image	3.99	2.34
FBP, LSE subspace	6.84	3.13
FBP, wavelet subspace	4.34	2.91
MAP, LSE subspace	4.95	5.01
MAP, wavelet subspace	6.38	5.40

Table 6: Average Lesion to Background Contrasts Using Different Method for Clinical Lung and Breast Metastasis Cases

6.4 Receiver Operating Characteristic (ROC) Study

It is known that lesion detectability is well described by the ROC curve. The ROC curve is determined by the rates of true positive and false positive. Fifty lesion phantom studies (with 250 known lesions) and fifty normal tissue phantom studies were conducted. The rates of true and false positive decisions made from the three ROI kinetic analyses are counted, respectively, to form ROC curves. The ROC curves, corresponding to the three kinetic feature analysis methods, are obtained by Monte Carlo simulations and shown in Fig. 1 (e). The resulting ROC curves show that the ROI based kinetic analyses with spatial decorrelation outperform the conventional TAC average. Putting an additional constraint to the structure of the interpixel correlation further lowers the false positive rate, because the correlation structure is estimated from the last frame and applied to the rest. Due to relatively high counts, the structure estimated in the last frame is more accurate than that in the early frames. The ROC curves, corresponding to the three kinetic feature analysis methods, are obtained by Monte Carlo simulations and shown in Fig. 6.4.

The resulting ROC curves showed that the area under curve (AUC) in the ROI based kinetic analysis with spatial decorrelation outperform the conventional TAC average. Putting an additional constraint to the structure of the interpixel correlation further lowers the false positive rate, because the correlation structure is estimated from the last frame and applied to the rest. The reason is that, due to relatively high counts, the structure estimated in the last frame is more accurate than that in the early frames. Also the AUC for MAP and OSEM is larger than that of FBP, which shown that the iterative reconstruction method outperform the FBP method not only in the image visualization, but also in the detection performance.

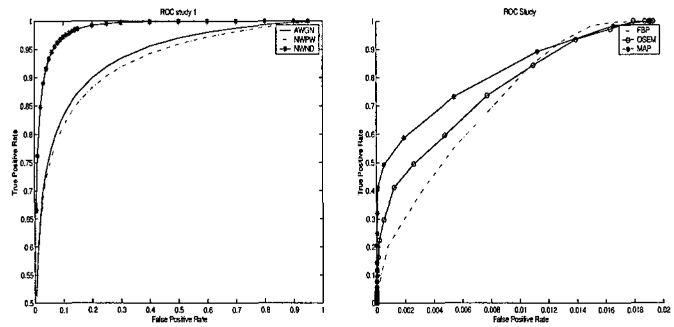

Figure 15: ROC curves simulation (a) FBP: GLRT (white noise, non-white noise) vs multi-pixel FLRT, where A_z(multi-pixel GLRT)> A_z (GLRT with non-white noise) $\approx A_z$ (GLRT with white noise). (b) GLRT with white noise assumption: A_z(MAP)> A_z(OSEM)> A_z(FBP).

6.5 Discussion

The phantom and the clinical data study show that:

matched subspace detection result v.s. original image: MSD results have higher tumor to background contrast. In phantom study, the MSD results can find lower lesion invisible in the original image. In clinical study, the MSD results improved lesion to background contrast for all cases, but for some case the high noise make the false alarm rate high.

replacement model v.s. superimposed model: In phantom study, it is guaranteed that the pure tumor TACs can be expressed explicitly by $\hat{\mathbf{H}}$ only and the pure normal TACs can be expressed explicitly by $\hat{\mathbf{S}}$ only. So the superimposed model, just as what we expected, have higher tumor to background contrast in phantom study. At the same time the noise in the MSD result with superimposed model is also higher than that with replacement model. However, the situation changes for clinical study. In reconstructed clinical PET image, the tumor, not matter how big it is, could be more or less mixed with normal tissue. There may not exist such a pure tumor which can be used to extract the true tumor only subspace $\mathbf{H}$. Even if the large tumor ROI were defined, the estimated tumor subspace is somehow mixed subspace $\hat{\mathbf{H}} \bigcup \hat{\mathbf{S}}$. So, for clinical study, the replacement model provide better results.

LSE bases v.s. wavelet bases: For some cases the LSE bases have better results, while for other cases wavelet bases provide better result. However, the wavelet method always have one advantage over LSE method: LSE needs blood input function which is not always available or blood modeling which will make the LS curve fitting process difficult. On the contrary, the wavelet method don't need blood input function all the time and is robust for all data set we test.

7 Conclusion

We have obtained encouraging results in preliminary research of exploiting kinetic features of the time activity curves (TAC), identification subspaces and using matched subspace filter to assist in lesion detection with FDG-PET dynamic images.

Results showed that the TAC subspaces identified from the FDG-FDG dynamic images have the important characteristics which are applicable for computer-aided lesion detection: (a) express TAC curves accurately, (b) distinguishable as lesion and normal tissue subspaces, (c) readily incorporable to a matched subspace detector for lesion detection. By an application of the identified lesion and normal tissue subspaces to the matched subspace detector, the lesion-to-normal tissue contrast can be significantly enhanced relative to the original filtered backprojection clinical images. A Monte Carlo of phantom dynamic study is conducted for the detection performance based a receiver operating characteristic (ROC) analysis.

A The condition of non-decreasing slope for the physiological process function

Suppose that the blood input function $C_p(t)$ is a continuous, differentiable function and satisfies the following conditions:

$$C_p(t) = 0,\ t < 0; \quad C_p(t) \geq 0, t \geq 0;$$
$$C_p'(t) = \frac{dC_p(t)}{dt} > 0, t < T_0, \quad C_p'(t) = 0, t = T_0; \quad C_p'(t) < 0, t > T_0, \tag{37}$$

More over, we assume all functions appear in this proof are differentiable and continuous.

Let the physiological process function be:

$$f(\beta, t) = C_p(t) \otimes e^{-\beta t} = \int_0^t C_p(\tau) e^{-\beta(t-\tau)} d\tau = \int_0^t C_p(t-\tau) e^{-\beta\tau} d\tau, \quad \beta \geq 0,\ t \geq 0 \tag{38}$$

We want to show that:

(i) $\forall\, T > T_0$, $\exists \beta^*$ s.t. $\frac{\partial f(\beta^*, t)}{\partial t}|_{t=T} = 0$

(ii) $\forall\, 0 < t < T$, $\frac{\partial f(\beta^*, t)}{\partial t} > 0$

(iii) $\forall\, \beta > \beta^*$, $\frac{\partial f(\beta, t)}{\partial t}|_{t=T} < 0$

(iv) $\forall\, 0 \leq \beta < \beta^*$, $\frac{\partial f(\beta, t)}{\partial t}|_{0<t\leq T} > 0$

Let $g(\beta, t) = \frac{\partial f(\beta, t)}{\partial t}$, using (38), $g(\beta, t)$ can be written as:

$$g(\beta, t) = \frac{\partial f(\beta, t)}{\partial t} = C_p(t) - \beta f(\beta, t) \tag{39}$$

or

$$g(\beta, t) = \frac{\partial f(\beta, t)}{\partial t} = C_p(0) e^{-\beta t} + \int_0^t C_p'(\tau) e^{-\beta(t-\tau)} d\tau = C_p(0) e^{-\beta t} + e^{-\beta t} \int_0^t e^{\beta\tau} C_p'(\tau) d\tau \tag{40}$$

Proof of (i).

When fix the $t = T$, $g(\beta, T)$ is the continious function of β. Using (39), when $\beta = 0$, $g(0, T) = C_p(T) > 0$. If we can show that $g(\beta, t)|_{t=T} < 0$ for some $\beta > 0$, then there must exist a β^* such that $g(\beta^*, T) = 0$.

Let T_0^+ be a time point s.t. $T_0 < T_0^+ < T$, there exist a number $0 < M < \infty$ s.t. $C_p'(t) \leq -M$, $\forall t \in [T_0^+, T]$. Also, there exist a number $0 < N < \infty$ s.t. $C_p'(t) \leq N, \forall t \in [0, T_0]$. Using the later part of equation (40):

$$
\begin{aligned}
g(\beta,T) &= e^{-\beta T}[C_p(0) + \int_0^T e^{\beta\tau} C_p'(\tau)d\tau] \\
&= e^{-\beta T}[C_p(0) + \int_0^{T_0} e^{\beta\tau} C_p'(\tau)d\tau + \int_{T_0}^{T_0^+} e^{\beta\tau} C_p'(\tau)d\tau + \int_{T_0^+}^{T} e^{\beta\tau} C_p'(\tau)d\tau] \\
&\leq e^{-\beta T}[C_p(0) + \int_0^{T_0} e^{\beta\tau} C_p'(\tau)d\tau + \int_{T_0^+}^{T} e^{\beta\tau} C_p'(\tau)d\tau] \\
&\leq e^{-\beta T}[C_p(0) + \int_0^{T_0} e^{\beta\tau} N d\tau - \int_{T_0^+}^{T} e^{\beta\tau} M d\tau] \qquad (41) \\
&= e^{-\beta T}[C_p(0) + N\frac{e^{\beta T_0}-1}{\beta} - M\frac{e^{\beta T}-e^{\beta T_0^+}}{\beta}] \\
&< \frac{e^{-\beta T}}{\beta}[C_p(0)\beta e^{\beta T_0^+} + Ne^{\beta T_0^+} + Me^{\beta T_0^+} - Me^{\beta T}] \\
&= \frac{Me^{-\beta(T-T_0^+)}}{\beta}[\frac{C_p(0)\beta+N+M}{M} - e^{\beta(T-T_0^+)}]
\end{aligned}
$$

Notice that $T - T_0^+ > 0$, the term $\frac{C_p(0)\beta+N+M}{M}$ increases linearly with β, while term $e^{\beta(T-T_0^+)}$ increases exponentially with β. So, for some $\beta > 0$, $g(\beta,T) < 0$. Now, since $g(0,T) > 0$ and we just proved that there exist a value β such that $g(\beta,T) < 0$, there must be a point β^* where $g(\beta^*,T) = 0$.

Proof of (ii)

When fix β^*, $g(\beta^*,t)$ is the function of t. By using (40), it's easy to show that $g(\beta^*,t) > 0$ for $t \in (0, T_0]$. Next, we'll consider the case for $t \in (T_0, T)$. From (39), taking time-derivative of $g(\beta,t)$ results in:

$$\frac{\partial g(\beta,t)}{\partial t} = C_p'(t) - \beta\frac{\partial f(\beta,t)}{\partial t} = C_p'(t) - \beta g(\beta,t) \qquad (42)$$

We have assume that $g(\beta^*,t)|_{t=T} = 0$. If $g(\beta^*,t)$ is not always positive in (T_0,T), suppose at time point $t' \in (T_0,T)$, $g(\beta^*,t') \leq 0$. Then there must exist another time point $t'' \in (t',T)$ such that: $\frac{\partial g(\beta^*,t)}{\partial t}|_{t=t''} \geq 0$, $C_p'(t'') < 0$ and $g(\beta^*,t'') = 0$, which contradict (42). So for $t \in (0,T_0)$, $g(\beta^*,t) > 0$. Combining two above cases, $\forall 0 < t < T$, $\frac{\partial f(\beta^*,t)}{\partial t} > 0$

Proof of (iii)

In order to prove (iii), we first need to prove that $\frac{\partial^2 f(\beta,t)}{\partial\beta\partial t}|_{\beta=\beta^*} < 0, \quad t \in (0,T]$. Continue from

(40),

$$\frac{\partial^2 f(\beta,t)}{\partial\beta\partial t} = -tC_p(0)e^{-\beta t} - \int_0^t (t-\tau)C_p'(\tau)e^{-\beta(t-\tau)}d\tau \tag{43}$$

This equation shows that $\frac{\partial^2 f(\beta,t)}{\partial\beta\partial t} < 0$ is hold for any $\beta \geq 0$ and $t \in (0, T_0]$. Proceed from (43):

$$\begin{aligned}
\frac{\partial^3 f(\beta,t)}{\partial t\partial\beta\partial t} &= -C_p(0)e^{-\beta t} + \beta tC_p(0)e^{-\beta t} - \int_0^t C_p'(\tau)e^{-\beta(t-\tau)}d\tau + \beta\int_0^t (t-\tau)C_p'(\tau)e^{-\beta(t-\tau)}d\tau \\
&= -C_p(0)e^{-\beta t} - \int_0^t C_p'(\tau)e^{-\beta(t-\tau)}d\tau + \beta[tC_p(0)e^{-\beta t} + \int_0^t (t-\tau)C_p'(\tau)e^{-\beta(t-\tau)}d\tau] \\
&= -\frac{\partial f(\beta,t)}{\partial t} - \beta\frac{\partial^2 f(\beta,t)}{\partial\beta\partial t}
\end{aligned} \tag{44}$$

To prove $\frac{\partial^2 f(\beta,t)}{\partial\beta\partial t}|_{\beta=\beta^*} < 0$ for $t \in (0,T)$, the prove by contradiction is used. Suppose there exist a solution to $\frac{\partial^2 f(\beta,t)}{\partial\beta\partial t}|_{\beta=\beta^*,t=t_0} = 0, \quad t_0 \in (T_0,T)$. Without loss the generality, we can also assume the t_0, if it exists, is the minimum one. So, $\frac{\partial^2 f(\beta,t)}{\partial\beta\partial t} < 0$ for $\beta = \beta^*, \; t \in (T_0, t_0)$. Using equation(44)

$$\frac{\partial^3 f(\beta,t)}{\partial t\partial\beta\partial t}|_{\beta=\beta^*,t=t_0} = -\frac{\partial f(\beta,t)}{\partial t}|_{\beta=\beta^*,t=t_0} < 0 \tag{45}$$

Notice that $t_0 \in (0,T)$, by using (ii), the "$<$" sign is hold. Remind that $\frac{\partial^2 f(\beta,t)}{\partial\beta\partial t} < 0$ for $t \in (0,T_0]$. As t increase from T_0, due to our assumption, t_0 is the first time point that the function $\frac{\partial^2 f(\beta,t)}{\partial\beta\partial t}$ becomes zeros. This implies that $\frac{\partial^3 f(\beta,t)}{\partial\beta\partial^2 t} \geq 0|_{\beta=\beta^*,t=t_0}$, contradict with (45). So, there does not exist t_0 such that $\frac{\partial^2 f(\beta,t)}{\partial\beta\partial t}|_{\beta=\beta^*,t=t_0} = 0$ for $t \in (0,T)$. Therefor

$$\frac{\partial^2 f(\beta,t)}{\partial\beta\partial t}|_{\beta=\beta^*} < 0, \quad t \in (0,T) \tag{46}$$

Next, we'll show $\frac{\partial^2 f(\beta,t)}{\partial\beta\partial t}|_{\beta=\beta^*,\ t=T} < 0$. Using equation (43),

$$\begin{aligned}
\frac{\partial^2 f(\beta,t)}{\partial\beta\partial t}|_{\beta=\beta^*,t=T} &= -TC_p(0)e^{-\beta^* T} - \int_0^T (T-\tau)C_p'(\tau)e^{-\beta^*(T-\tau)}d\tau \\
&= -T[C_p(0)e^{-\beta^* T} + \int_0^T C_p'(\tau)e^{-\beta^*(T-\tau)}d\tau] + \int_0^T \tau C_p'(\tau)e^{-\beta^*(T-\tau)}d\tau \\
&= -Tg(\beta^*,T) + \int_0^T \tau C_p'(\tau)e^{-\beta^*(T-\tau)}d\tau
\end{aligned} \tag{47}$$

Notice that $g(\beta^*, T) = 0$, so:

$$\begin{aligned}
\frac{\partial^2 f(\beta,t)}{\partial\beta\partial t}|_{\beta=\beta^*,t=T} &= \int_0^T \tau C_p'(\tau)e^{-\beta^*(T-\tau)}d\tau \\
&= \int_0^{T_0} \tau C_p'(\tau)e^{-\beta^*(T-\tau)}d\tau + \int_{T_0}^T \tau C_p'(\tau)e^{-\beta^*(T-\tau)}d\tau \\
&< \int_0^{T_0} T_0 C_p'(\tau)e^{-\beta^*(T-\tau)}d\tau + \int_{T_0}^T T_0 C_p'(\tau)e^{-\beta^*(T-\tau)}d\tau \\
&= T_0 \int_0^T C_p'(\tau)e^{-\beta^*(T-\tau)}d\tau \\
&= T_0[g(\beta^*, T) - C_p(0)e^{-\beta^* T}] = -T_0 C_p(0)e^{-\beta^* T} \leq 0
\end{aligned} \tag{48}$$

So, $\frac{\partial^2 f(\beta,t)}{\partial t\partial\beta}|_{\beta=\beta^*,\ t=T} < 0$. Combine this with (46), we get:

$$\frac{\partial^2 f(\beta,t)}{\partial t\partial\beta}|_{\beta=\beta^*} < 0, \quad t \in (0,T] \tag{49}$$

Next, we'll prove $\forall\beta > \beta^*$, $\frac{\partial f(\beta,t)}{\partial t}|_{t=T} < 0$ by using (49) and prove by contradiction. If (iii) is not hold, then when β increases from β^*, assume the function $\frac{\partial f(\beta,t)}{\partial t}|_{t=T}$ cross the zero first time when $\beta = \beta^{*+}$. Notice that, same as β^*, β^{*+} also satisfies (ii) and (49). This implies, $\frac{\partial^2 f(\beta,t)}{\partial t\partial\beta}|_{\beta=\beta^{*+},\ t=T} < 0$. But this contradicts with the assumption that β^{*+} is the first value which makes $\frac{\partial f(\beta,t)}{\partial t}|_{t=T}$ cross the zero. There for:

$$\forall\ \beta > \beta^*, \quad \frac{\partial f(\beta,t)}{\partial t}|_{t=T} < 0 \tag{50}$$

Proof of (iv)

Use the same technique as proof of (iii), we can prove $\forall\ 0 \leq \beta < \beta^*$, $\frac{\partial f(\beta,t)}{\partial t}|_{t=T} > 0$. So, we only need to prove that

$$\forall\ 0 \leq \beta < \beta^*, \ \frac{\partial f(\beta,t)}{\partial t}|_{0<t<T} > 0 \tag{51}$$

The proof by contradict will be employed again. Assume (51) is not hold, because $\frac{\partial f(\beta,t)}{\partial t}$ is continuous function, there must exist a β^{*-}, $0 \leq \beta^{*-} < \beta^*$ and a T^-, $0 < T^- < T$ such that $\frac{\partial f(\beta,t)}{\partial t}|_{\beta=\beta^{*-},\ t=T^-} = 0$. Then β^{*-} and T^- are a pair of β and t values which satisfy (i), (ii) and (iii). To make to clear, rewrite (iii) for β^{*-} and T^- case:

$$\forall\ \beta > \beta^{*-}, \ \frac{\partial f(\beta,t)}{\partial t}|_{t=T^-} < 0 \tag{52}$$

Notice that $\beta^* > \beta^{*-}$, $T^- < T$, above equation implies that $\frac{\partial f(\beta,t)}{\partial t}|_{\beta=\beta^*,\ t=T^-} < 0$ which is obviously contradict with (ii). So, equation (51) is hold. Finally, result in:

$$\forall\ 0 \leq \beta < \beta^*,\ \frac{\partial f(\beta,t)}{\partial t}|_{0<t\leq T} > 0 \tag{53}$$

References

[1] D. Barber, "The use of principal components in the quantitative analysis of gamma camera dynamic studies," *Phys. Med. Biol.,* 25: p. 283-292, 1980.

[2] R.E. Carson, *et al.,* "An approximation formula for the variance of PET region-of-interest values," *IEEE Trans. Med. Imag.,* Vol. 12, No. 2, p. 240-250, June 1993.

[3] P.S. Conti *et al.,* "PET and [^{18}F]-FDG in oncology: a clinical update," *Nuclear Med. and Bio.,* Vol: 23, p. 717-735, 1996.

[4] D. Feng and X. Wang, "A computer simulation study on the effects of input function measurement noise in tracer kinetic modeling with positron emission tomography (PET)," *Comput. Bio. Med.,* Vol. 23, No. 1, p. 57-68, 1984.

[5] William J. Geckle "Physiological factor analysis (PFA) and parametric imaging of dynamci PET images," *Fifth Annual IEEE Symposium on Computer-Based Medical Systems,* p 9-16, 1992.

[6] G.H. Golub and C.F. Van Loan, *Matrix Computation,* 3rd edition, the Johns Hopkins University Press, 1996.

[7] C. C. Huang and X. Yu, "Computer-aided lesion detection with statistical model-based features in PET images," *USC-Radiology Internal Report,* July, 1996.

[8] C.C. Huang, X. Yu, J.R. Bading, and P.S. Conti, "Computer-aided lesion detection with statistical model-based features in PET images," *IEEE Trans. Nuclear Science*, Vol. 44, No. 6, p. 2509-2521, Dec. 1997.

[9] C.C. Huang, X.Yu, J. Bading, and P.S. Conti, "Feature extraction by subspace fitting of time activity curve in PET dynamic studies," *IEEE Med. Imag. Conf.,* Nov. 1997.

[10] R.H. Huesman, "A new fast algorithm for the evaluation of regions of interest and statistical uncertainty in computed tomography," *Phys. Med. Biol.,* Vol. 29, No 5, p. 543-552, 1984.

[11] K. Kubota, T. Matsuzawa, *etc.,* "Differential diagnosis of lung tumor with positron emission tomography: A prospective study," *J. of Nucl. Med.,* Vol. 31, p. 1927-1933, 1990.

[12] G. Lucignani, K.C. Schmidt, R.M. Moreco, *et al.*, "Measurement of regional cerebral glucose utilization with Fluorine-18-FDG and PET in heterogeneous tissues: Theoretical considerations and practical procedure," *J. Nuclear Med.,* Vol. 34, No, 3, 360-369, Mar. 1993.

[13] S.R. Meikle, J.C. Matthews, V.J. Cunningham, *etc.* "Spectral analysis of PET projection data," *Medical Imaging Conference,* p. 1888-1892, 1997.

[14] K.S. Nijran and D. Barber, "Towards automatic analysis of dynamic radionuclide studies using principal-component factor analysis," *Phys. Med. Biol.,* 30: p. 1315-1325, Dec. 1985.

[15] K.S. Nijran and D. Barber, "Factor analysis of dynamic function studies using a priori physiological information," *Phys. Med. Biol.,* 31: p. 1107-1117, Oct. 1986.

[16] F. O'Sullivan, "Imaging radiotracer model parameters in PET: A mixture analysis approach," *IEEE Trans. Med. Imag.,* Vol. 12, No. 3, p. 399-412, 1993.

[17] F. Pedersen, M. Bergstrom, E. Bengtsson, and B. Langstrom, "Principal component analysis of dynamic positron emission tomography images," *European J. of Nucl. Med.,* Vol. 21, No. 12, p. 1285-1292, Dec. 1994.

[18] M.E. Phelps, J.C. Mazziotta, and H.R. Schelbert, *Positron Emission Tomography and Autoradiology, Principles and Applications for the Brain and Heart,* Raven Press, 1986.

[19] L.L. Scharf and B. Friedlander, "Matched subspace detectors," *IEEE Trans. Signal Processing,* Vol. 42, No. 8, p. 2146-2157, Aug. 1994.

[20] K. Schmidt, G. Mies, and L. Sokoloff, "Model of kinetic behavior of deoxyglucose in heterogeneous tissues in brain: A reinterpretation of the significant of parameters fitted to homogeneous tissue models," *J. Cerebral Blood Flow and Metabolism,* Vol. 11, p. 10-24, 1991.

[21] S.C. Huang, M.E. Phelps, E.J. Hoffman, K. Sideris, C.J. Selin, and D. E. Kuhl, "Noninvasive determination of local cerebral metabolic rate of glucose in man," *Amer. Physiological Society,* E69-E82, 1980.

[22] L.G. Strauss and P.S. Conti, "The applications of PET in clinical oncology," *J. of Nuclear Med.,* Vol. 32, No. 4, p. 623-648, Apr. 1991.

[23] M. Viberg and B. Ottersten, "Sensor array processing based on subspace fitting," *IEEE Trans. Signal Processing,* Vol. 39, No. 5, p. 1110-1121, May 1991.

[24] X. Yu and I.S. Reed "Adaptive detection of signals with feature linear mappings and representations," *IEEE Trans. Signal Processing,* Vol. 43, No. 12, Dec. 1995.

[25] X. Yu and C.C. Huang, "Lesion detection with statistical model-based prior information in positron emission tomography," *IEEE Med. Imag. Conf,,* Anaheim, CA, Nov. 2-9, 1996.

[26] H. Zhuang, M. Pourdehnad, E.S. Lambright, etc. "Dual Time Point 18F-FDG PET Imaging for Differentiating Malignant from Inflammatory" *J. Nucl. Med,* 2001, 42: 1412-1417

[27] T.E. Nichols, J. Qi, E. Asma, R.M. Leahy, "Spatiotemporal Reconstruction of List-Mode PET Data" *IEEE Tran. on Med. Imag* Apr. 2002, vol. 21, NO. 4, p396-404

[28] X. Yu, Z. Li and J. Chen, "Exploration and Processing Spatial-Temporal Features in Dynamic FDG-PET", *Annual Report to DoD BCRP,* 2003.

[29] Kenneth R. Zasadny and Richard L. Wahl "Enhanced FDG-PET Tumor Imaging with Correlation-Coefficient Filtered Influx-Constant Images" *The Journal of Nuclear Mecidine,* Vol.37, No.2, Feb. 1996

[30] C.L. Lawson and R.J. Hanson, "Solving Least Squares Problems" *Prentice-Hall,* 1974, Chapter 23, p. 161.

[31] Martin Vetterli, Jelena Kovacevic "Wavelets and subband coding" *Prentice Hall* 1995

APPENDIX B

Enhanced Dynamic FDG-PET Tumor Detection with Constrained Temporal Filtering [1]

Jiansong Chen and Xiaoli Yu
Department of Electrical Engineering, Department of Radiology
University of Southern California
Los Angles, CA 90089-2565

December 9, 2004

[1]This work was supported in part by STOP CANCER Foundation

Abstract

Residual FDG activity in normal tissues, such as blood vessels and the liver, as well as the spilled in background activity can impair the detection of small or modestly tracer-avid tumors in FDG-PET cancer imaging. In order to maximize tumor visualization but minimize background and artifacts, an efficient new method is adapted from the constrained temporal filtering processing widely used for signal detection and extended to the application of dynamic FDG-PET processing. Comparing with the well-known Patlak analysis and spectral analysis (SA), the main advantage of the proposed method is that it can objectively remove the partial volume effect superimposed onto the TAC as well as the residual blood activities and result in the pixel-by-pixel estimations of the infux constant as the output of the filter. Since the constrained temporal filter is designed to preserve the power of tumor signal, therefore, it is likely to offer a desirable noise canceling result, while make no or minimum distortion on tumor signatures. In contrast, Patlak analysis may suffer in their ability to classify tumor and normal structures when the tumor is severely interfered by background activity and present approximately similar time activity curve as that of normal tissues at the end of the post-FDG injection period. For comparison, analytical expressions for SNR and CNR of filtered images are derived, and the results of our digital phantom study suggest that the proposed method has the best performance, comparing with the Patlak and SA. The mice implanted with cancer cells are imaged with dynamic FDG-PET on the 6th day and the 12th day after implantation, respectively. The proposed method is applied to process the earlier acquired images and the resulting findings are confirmed with the later acquisitions. The results show that the new method can enhance the tumor-to-background ratio at an early stage and is promising for improving lesion detectability.

1 Introduction

Positron emission tomography (PET) with [^{18}F]2-fluoro-2-deoxy-D-glucose(FDG)has been widely used for non-invasive diagnosis of cancer. The diagnostic advantage of FDG-PET is important because alterations in the metabolism of cells are often evidenced in disease states before structural changes can be determined using other medical imaging technologies, such as computerized tomography (CT) and magnetic resonance imaging (MRI). While PET imaging provides a higher sensitivity (95) for detecting lymph node metastasis than alternative modalities [1], recent study shows nearly a 20 false-negative rate[2]. In addition to the relatively limited spatial resolution of PET, the residual blood-born FDG activity may be contributing to this finding. Note that most dynamic FDG-PET tumor detection methods are based on one fact that malignancies can be distinguished from normal tissues on the basis of biologically determined radiotracer accumulation or loss rate. Because malignant tumors are metabolically active and FDG-avid on PET imaging, they metabolize glucose at a much higher rate than do most normal tissues[3]. However, even after 60 minutes post-FDG injection, there is substantial blood-pool FDG activity remaining, possibly impairing the ability to detect small tumor near blood vessel or near tissues with high normal FDG activity. Besides the effect of residual FDG activity, the partial volume effect (PVE) also imparis the spatial resolution of PET. PVE is contributed from the surrounding background activities, the boundary pixels of a malignant area represent a mixture of tumor and normal tissues, instead of the pure tumor tissues. Therefore, PVE dramatically lowers the tumor-to-background contrast of small structures that are smaller than two times the full-width at half-maximum (FWHM)of the tomograph [4].

Developing methodologies for maximally removing the residual blood FDG activity and correcting the PVE has always been a critical issue in various FDG-PET quantitative studies. For instance, the non-parametric techniques simply decompose the observed FDG-PET data to extract the desired signal subspace using singular value decomposition or eigen-decomposition method. After kinetic modeling using FDG is well established, parametric methods attract more attention. The widely used Patlak analysis estimates the macroparameter by determining the slope of a *transformed* tracer uptake curve, which is based on three-compartment three-rate constants model

(3K)[5]. This method is extremely computationally efficient and has good performance on residual FDG activity cancellation [2]. However, the assumption underlying the Patlak method is that FDG is irreversibly trapped in the system($k_4 = 0$) and this assumption only be valid for most malignant tumors with progresive FDG accumulation in tissue over time. Therefore, Patlak analysis may be vulnerable when the tumor is severely interfered by background activity because of PVE. Spectral analysis is another conventional parametric approach, which enables the determination of pharmacokinetic parameters with relatively few model assumptions[6]. This method is limited by a lack of knowledge of parameters in the model and the fitting procedure is also a concern, which is based on non-negative lease squares (NNLS) algorithm, not a linear operator. Other previous attempts to produce high quality PET images considered the use of various filters for FDG-PET images either in the spatial or frequency domains[7],[8],[9].

This paper proposes a new approach by using a constrained temporal filter. The emphasis of this method is to preserve the FDG features attributed to tumor tissues and eliminate the undesired contributions of the residual FDG activity at the same time. In fact, by using two imposed constraints, we can objectively remove the partial volume effect superimposed onto the time-activity curves (TACs) as well as the residual blood activities, while making no distortion on the desired malignancy features in time domain. Moreover, because this constrained temporal filter is designed to minimize the energy of the output signal, our approach can also suppress the PVE and statistical noise, besides removal of the structured interferences. Simulation results in section IV show that the proposed approach outperforms Patlak and spectral analysis.

The paper is structured as follows. Sections II introduce the FDG model and briefly review Patlak and spectral analysis. Sections III presents the ... Section IV validates ... through phantom and animal studies.

Notation: All boldface letters indicate vectors (lower case) or matrices (upper case).

2 The Fluoro-Deoxy-Glucose (FDG) Kinetic Model

2.1 A 4-k Compartmental Model for the FDG Tracer Kinetics

The FDG kinetic model consists of three compartments which describes the tracer distribution in the homogeneous tissue, as shown in Figure 1. The first compartment is considered as the blood pool region and represents the concentration of FDG in the plasma. The second and third compartments contain the concentrations of FDG in tissue and phosphorylated FDG in tissue (FDG-6-P), respectively. The rate constants in Figure 1 are defined as follows:

$$\begin{aligned} K_1 &= \text{the transport of FDG in plasma to tissue,} \\ k_2 &= \text{the transport of FDG in tissue to plasma,} \\ k_3 &= \text{the phosphorylation of FDG to FDG-6-P,} \\ k_4 &= \text{the dephosphorylation of FDG-6-P to FDG.} \end{aligned}$$

The rate of change in the concentrations of FDG and FDG-6-P in a homogeneous ROI can be described by the following differential equations

$$\begin{aligned} \frac{dC_e(t)}{dt} &= K_1 C_p(t) - (k_2 + k_3) C_e(t) + k_4 C_m(t), \\ \frac{dC_m(t)}{dt} &= k_3 C_e(t) - k_4 C_m(t), \end{aligned} \tag{1}$$

where $C_e(t)$ represents the concentration of FDG in the tissue at time t, $C_m(t)$ represents the concentration of FDG-6-P (and all metabolites derived from FDG-6-P) in the same region, and $C_p(t)$ represents the FDG concentration in the arterial plasma. Solutions of (1) [10] given that the initial conditions $C_e(0) = C_m(0) = 0$ show that the total radioactivity for a homogeneous tissue, $C(t)$, is the sum of the free [^{18}F]FDG concentration plus the concentration of metabolites, i.e.,

$$\begin{aligned} C(t) &= C_e(t) + C_m(t) \\ &= \frac{K_1}{\beta_2 - \beta_1} \left[(k_3 + k_4 - \beta_1) \mathrm{e}^{-\beta_1 t} + (\beta_2 - k_3 - k_4) \mathrm{e}^{-\beta_2 t} \right] \otimes C_p(t) \\ &= \left[M_1 \mathrm{e}^{-\beta_1 t} + M_2 \mathrm{e}^{-\beta_2 t} \right] \otimes C_p(t), \end{aligned} \tag{2}$$

where

$$\begin{aligned} \beta_1 &= \frac{1}{2} \left[(k_2 + k_3 + k_4) - \sqrt{(k_2 + k_3 + k_4)^2 - 4 k_2 k_4} \right], \\ \beta_2 &= \frac{1}{2} \left[(k_2 + k_3 + k_4) + \sqrt{(k_2 + k_3 + k_4)^2 - 4 k_2 k_4} \right], \\ M_1 &\triangleq \frac{K_1}{\beta_2 - \beta_1} (k_3 + k_4 - \beta_1), \\ M_2 &\triangleq \frac{K_1}{\beta_2 - \beta_1} (\beta_2 - k_3 - k_4), \end{aligned} \tag{3}$$

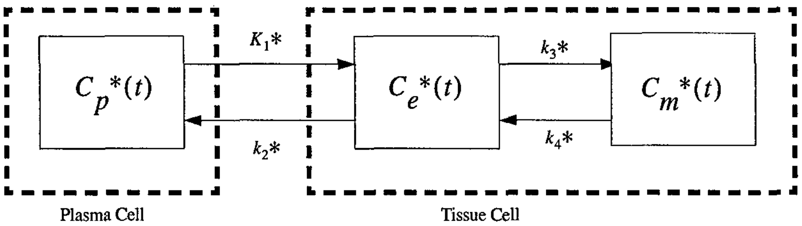

Figure 1: 4-k three compartment model

and $\otimes$ denotes the convolution operator.

The radioactivity measured by the PET scanner (under noise-free assumption), including the radioactivity in the cerebral blood, can be represented as

$$C_{\text{total}}(t) = V_b C_p(t) + C(t) = V_b C_p(t) + [M_1 e^{-\beta_1 t} + M_2 e^{-\beta_2 t}] \otimes C_p(t), \tag{4}$$

where $C_{\text{total}}(t)$ is the total radioactivity measured by the scanner at time t; V_b denotes the vascular space in tissue and FDG concentration in whole blood is assumed to be $V_b C_p(t)$ at time t [11].

2.2 A 3-k Compartmental Model for the FDG Tracer Kinetics

The 3-K compartment FDG model is proposed by Sokoloff *et al.* in 1977 [10]. This model assumes that [^{18}F]FDG-6-P is irreversibly trapped in tissue for the duration of experiment and it is described by

$$\begin{aligned} \frac{dC_e(t)}{dt} &= K_1 C_p(t) - (k_2 + k_3) C_e(t), \\ \frac{dC_m(t)}{dt} &= k_3 C_e(t), \end{aligned} \tag{5}$$

The total radioactivity, including the radioactivity in the cerebral blood, is represented as

$$C_{\text{total}}(t) = V_b C_p(t) + C(t) = V_b C_p(t) + [M_1 + M_2 e^{-\beta_2 t}] \otimes C_p(t), \tag{6}$$

3 CONVENTIONAL METHODS OF DYNAMIC PET TUMOR DETECTION

Before presenting the proposed constrained temporal filtering approach, it is worthwhile to present a brief overview of Paltlak and spectral analysis in general. We will compare the performance of these two methods with that of the proposed approach in Section V.

3.1 Patlak analysis

Patlak analysis assumes 3-K compartment model for the FDG tracer kinetics (that is, k_4^* is assumed to be zero).

The solution to the differential equations (3) is

$$C_{\text{total}}(t) = K_i \int_0^t C_p(\tau)d\tau + vC_p(t) \tag{7}$$

where v is related to the effective distribution volume of FDG.

By dividing through by $C_p(t)$, the Patlak method employed to determine the macroparameter $K_i = \frac{K_1 k_3}{k_2+k_3}$ is given by

$$\frac{C_{\text{total}}(t)}{C_p(t)} = K_i \frac{\int_0^t C_p(\tau)d\tau}{C_p(t)} + v \tag{8}$$

Based on above equations, Patlak approach is implemented by an pixel-by-pixel analysis of $\frac{\int_0^t C_p(\tau)d\tau}{C_p(t)}$ versus $\frac{C_{\text{total}}(t)}{C_p(t)}$, which gives the estimation of K_i. That K_i-slope image is expected to be a one parameter approach to improve image contrast over static imaging, since the tumor would have a higher influx and retention of FDG over most other normal tissues as a function of time. In particular, earlier work in [2] shows that Patlak analysis has good performance on residual FDG activity cancellation.

However, Patlak analysis may be vulnerable because the assumption underlying the Patlak method is that FDG is irreversibly trapped in the system (k_4=0). Even this assumption is valid for most cases because most malignant tumors have progressive FDG accumulatio in tissue over time, it is failed sometimes when the tumor is severely interfered by background activity because of PVE. Figure 5(b) shows the time-activity curves (TACs) extracted in the selected ROIs from a mouse study at an early stage of tumor growth. As we can see the TAC of the tumor tissue has an approximately flat slope at the later frames. If we apply Patlak analysis to compute the K_i-slope image, it fails to classify the tumor and normal tissues.

3.2 Spectral analysis

In the spectral analysis method, the tissue concentration of FDG activity, $C_{\text{total}}(t)$, is modeled as a linear combination of basis functions, each defined as a exponential function convolved with $C_p(t)$:

$$
\begin{aligned}
C_{\text{total}}(t) &= \sum_{j=1}^{J} \alpha_j e^{-\beta_j t} \otimes C_p(t), \qquad t \geq 0 \\
&= \sum_{j=1}^{J} \alpha_j f(\beta_j, t), \qquad t \geq 0
\end{aligned} \tag{9}
$$

where J is the maximum number of basis functions allowed in the model and values of β are chosen to cover the spectrum of expected kinetic behavior. A spectrum of β values are predefined and spaced logarithmically on a given interval $[\lambda,1]$, where λ is the decay constant of the radioisotope. The unknown coefficients, α_j, can be estimated by the linear least square recursive curve fitting technique with non-negative constrains. This technique can be applied at a pixel level enabling calculation of parametric images independent of an assumed compartmental structure [11]. Therefore, it is a general modeling approach. However, due to a lack of knowledge on the range of β, covering the spectrum of all possible kinetic behavior often results in estimation of a large number of unknown coefficients α_js. The accuracy of the estimation is then degraded. Furthermore, the linearity of the spectral analysis method may break down if (a) one or more of the measurement vectors contains negative values, or (b) the true number of non-zero coefficients cannot be resolved, either because of measurement noise or insufficient degrees of freedom. [12]

4 CONSTRAINED TEMPORAL FILTER

4.1 Optimization Criteria

Based on 3-K compartment model and taking into account the partial volume effect, we rewrite the equation (7) as

$$
C_{total}(t) = K_i \int_0^t C_p(\tau)d\tau + V_b C_p(t) + C_v(t) + N(t) \tag{10}
$$

where $C_v(t)$ is the sum of $[M_2 \mathrm{e}^{-\beta_2 t} \otimes C_p^*(t)]$ and partial volume effect (PVE) contributed from the surrounding pixels (voxels) ; $N(t)$ is the random noise which is uncorrelated with $C_p(t)$ and $C_v(t)$. Let vector $\mathbf{c}_p = [C_p(t_1), C_p(t_2), \ldots, C_p(t_m)]^T$ be the sampled plasma concentration, where t_j is the time instant that frame j is acquired, and similarly define the vectors, $\mathbf{c}_{total}$, $\mathbf{c}_v$ and $\mathbf{n}$. Equation (10) then be expressed in a vector form,

$$\mathbf{c}_{total} = K_i\mathbf{s}_p + V_b\mathbf{c}_p + \mathbf{c}_v + \mathbf{n} = K_i\mathbf{s}_p + \mathbf{e} \tag{11}$$

where

$$\mathbf{s}_p = [\int_0^{t_1} C_p(\tau)d\tau, \int_0^{t_2} C_p(\tau)d\tau, \ldots, \int_0^{t_m} C_p(\tau)d\tau \tag{12}$$

$$\mathbf{e} = V_b\mathbf{c}_p + \mathbf{c}_v + \mathbf{n} \tag{13}$$

In order to cancel the interference $\mathbf{e}$ defined in equation (13), pervious work has developed many ways to find the weight vector $\mathbf{w}$ of an optimum filter subject to well-defined optimality criteria. Although the details differ in different applications, the main assumptions and processing algorithms are essentially the same. In particular, an important assumption is that the interfering signals are uncorrelated with the desired signal. However, in our practice, the signal ($K_i\mathbf{s}_p$) and the interference ($\mathbf{e}$) may be either partially or completely correlated. Moreover, [13] shows how the interference rejection becomes more severe with increasing correlation between the desired signal and the interferences. Therefore, in this work, we introduce a new optimum criterion called *optimum interference plus noise rejecter* [14]. By using this criterion, all the interferences, whether correlated or uncorrelated with the desired signal, are considered undesired and the weight vector $\mathbf{w}$ is chosen to pass the K_i undistorted at the filter output while maximally rejecting the contribution of the residual FDG activity, PVE and random noise. Multiplying both sides of equation (11) with $\mathbf{w}$, the output of the optimum filter is given by

$$\begin{aligned}\mathbf{w}^T\mathbf{c}_{total} &= K_i\mathbf{w}^T\mathbf{s}_p + V_b\mathbf{w}^T\mathbf{c}_p + \mathbf{w}^T\mathbf{c}_v + \mathbf{w}^T\mathbf{n}\\ &= K_i\mathbf{w}^T\mathbf{s}_p + \mathbf{w}^T\mathbf{e}\end{aligned} \tag{14}$$

where $\mathbf{w}^T\mathbf{e}$ is the undesired contribution of the residual FDG activity, PVE and noise.

Then we propose two constrains to ensure unity gain in the desired signal direction and complete removal of the interference,

$$\mathbf{w}^T\mathbf{s}_p = 1 \tag{15}$$

$$\mathbf{w}^T\mathbf{e} = 0 \tag{16}$$

However, because interference $\mathbf{e}$ includes unknown random noise $\mathbf{n}$ and background FDG concentration $\mathbf{b}_g$, it is usually difficult to determine the exact format of the $\mathbf{e}$. In practice, we define another interference variable $\mathbf{e}_{sub}$ as $\mathbf{e}_{sub} = \mathbf{c}_p$ or $\mathbf{e}_{sub} = [\mathbf{c}_p, \mathbf{b}_g]$, which is depended on whether we can successfully extract the features of the interference caused by $\mathbf{b}_g$. Then, we can rewrite (16) as

$$\mathbf{w}^T \mathbf{e}_{sub} = 0 \tag{17}$$

and the optimization objection function can be expressed as

$$\min_{\substack{\mathbf{w}^T \mathbf{s}_p = 1 \\ \mathbf{w}^T \mathbf{e}_{sub} = 0}} E[(\mathbf{w}^T \mathbf{e})(\mathbf{w}^T \mathbf{e})^T] = \min_{\substack{\mathbf{w}^T \mathbf{s}_p = 1 \\ \mathbf{w}^T \mathbf{e}_{sub} = 0}} \mathbf{w}^T \mathbf{R_e} \mathbf{w} (18)$$

where $\mathbf{R_e}=E(\mathbf{e}\mathbf{e}^T)$ is the covariance matrix of the interference and it is free of the desired signals. Substituting the constraints (15) and (17) into (14), the output of the optimum filter is

$$\hat{K}_i = \mathbf{w}^T \mathbf{c}_{total} = K_i + \mathbf{w}^T \mathbf{c}_v + \mathbf{w}^T \mathbf{n} \approx K_i \tag{19}$$

The approximation in (19) holds because the interference $\mathbf{e}$, including random noise, should be minimized by the filter $\mathbf{w}$ resulted from Equation (18).

4.2 Constrained Filter

The addition of the constrains to adaptive processing was first described by Frost [15]. Frost presented a method of adapting the weights in a filter while holding the filter response fixed in a certain waveform or time function or at certain frequencies [16]. It means that if we have a $m \times 1$ constraint vector $\mathbf{h}_i$ defined in prior by a filter designer, no matter how the filter weights w_i are changed, we can always keep

$$\mathbf{w}^T \mathbf{h}_i = f_i \tag{20}$$

where f_i is a given constant and $\mathbf{w}$ is a $m \times 1$ weight vector.

Equation (12) illustrates that the constrained filter will preserve all the energy of $\mathbf{h}_i$ if f_i equals to unity and eliminate the energy of $\mathbf{h}_i$ if f_i equals to zero. Suppose there are K such constraint equations altogether. Then we may combine these constraints in one equation by defining a $m \times K$ constraint matrix,

$$\mathbf{H} = [\mathbf{h}_1, \mathbf{h}_2, \ldots, \mathbf{h}_K] \tag{21}$$

and by defining $\mathbf{f}$ to be a K-dimensional vector of the coefficients f_i,

$$\mathbf{f} = [f_1, f_2, \ldots, f_K]^T \tag{22}$$

The constrains may then by written as

$$\mathbf{w}^T\mathbf{H} = \mathbf{f}^T \tag{23}$$

If we let the interference $\mathbf{e}$(13) be the input signal of the constrained filter, then the output signal is,

$$\hat{\mathbf{e}} = W^T\mathbf{e} \tag{24}$$

The average power of the constrained filter output signal is

$$P = \mathbf{w}^T E(\mathbf{e}\mathbf{e}^T)\mathbf{w} = \mathbf{w}^T\mathbf{R_e}\mathbf{w} \tag{25}$$

Hence the optimization problem is to minimize $\mathbf{w}^T\mathbf{R_e}\mathbf{w}$ subject to the constraint (23). Comparing with (18), that is exactly the optimization criterion what we started in the previous part. By using LMS criteria [18], we have

$$\mathbf{w} = \mathbf{R_e}^{-1}\mathbf{H}(\mathbf{H}^T\mathbf{R_e}^{-1}\mathbf{H})^{-1}\mathbf{f} \tag{26}$$

which is the weight vector of our constrained temporal filter, satisfying the optimization criterion (18). The derivation of (26) is given in Appendix A.

In the following discussion, we will use the above derivation to find the the constrained temporal filter in order to enhance the tumor-to-background contrast in dynamic PET imaging. Suppose the image size is $L \times L$ pixels at a given frame. Combining all images of m frames together, we form a new $m \times L^2$ matrix,

$$\mathbf{X} = [\mathbf{c}_{total}{}^1, \mathbf{c}_{total}{}^2, \ldots, \mathbf{c}_{total}{}^{L^2-1}, \mathbf{c}_{total}{}^{L^2}] \tag{27}$$

where $\mathbf{c}_{total}{}^i$ is the TAC in vector form at the i^{th} pixel as illustrated in (11).

Even though our goal is to minimize $\mathbf{w}^T\mathbf{R_e}\mathbf{w}$ (18) (25), it is actually difficult to determine the value of interference $\mathbf{e}$ and its covariance matrix $\mathbf{R_e}$ since they include the unknown random noise $\mathbf{n}$ and background FDG concentration $\mathbf{b}_g$. In practice, we take and alternative way to achieve that goal.

Because the tumors under our study are assumed being small, in the TAC observations $\mathbf{c}_{total}{}^{i}$, the residual FDG activity, PVE and noise should be dominant, comparing with the FDG activity of tumor tissue. Therefore, we can use samples of $\mathbf{c}_{total}{}^{i}$ at all different pixels to approximate the covariance matrix of $\mathbf{e}_{sub}$,

$$\mathbf{e}_{sub} \approx \mathbf{e} \approx \mathbf{X} = [\mathbf{c}_{total}{}^{1}, \mathbf{c}_{total}{}^{2}, \dots, \mathbf{c}_{total}{}^{L^2-1}, \mathbf{c}_{total}{}^{L^2}] \tag{28}$$

hence

$$\widehat{\mathbf{R}_{\mathbf{e}_{sub}}} \approx \widehat{\mathbf{R}_{\mathbf{e}}} \approx \mathbf{X}\mathbf{X}^T \tag{29}$$

and using the two constrains stated in (15) and (16), we construct the constraint matrix,

$$\mathbf{H} = [\mathbf{s}_p, \mathbf{e}_{sub}] \tag{30}$$

and

$$\mathbf{f} = \begin{cases} [1,0], & if\ \mathbf{e}_{sub} = \mathbf{c}_p\ ; \\ (1), & if\ \mathbf{e}_{sub} = [\mathbf{c}_p, \mathbf{b}_g]\ . \end{cases} \tag{31}$$

$$\begin{aligned} \mathbf{f} = [1,0], &\qquad if\ \mathbf{e}_{sub} = \mathbf{c}_p \\ or \qquad \mathbf{f} = [1,0,0], &\qquad if\ \mathbf{e}_{sub} = [\mathbf{c}_p, \mathbf{b}_g] \end{aligned} \tag{32}$$

Substituting (30), (33)and (30) into (26),we have the optimum constrained temporal filter for dynamic PET, which satisfied (15), (16) and (18)

4.3 Extension to 4-K model

We can also adapt the proposed optimum criterion to the 4-K compartment model. Using the same definitions as in (6), the tissue concentration of FDG activity is rewritten as:

$$\mathbf{c}_{total}(t) = M_1 \int_0^t e^{-\beta_1(t-\tau)}\mathbf{c}_p(\tau)d\tau + V_b\mathbf{c}_p(t) + \mathbf{c}_v(t) + \mathbf{n}(t) \tag{34}$$

and the vector form is given by:

$$\mathbf{c}_{total} = M_1\mathbf{s}_p + V_b\mathbf{c}_p + \mathbf{c}_v + \mathbf{n} = M_1\mathbf{s}_p + \mathbf{e} \tag{35}$$

where

$$\mathbf{s}_p = [\int_0^{t_1} e^{-\beta_1(t_1-\tau)}\mathbf{c}_p(\tau)d\tau, \int_0^{t_2} e^{-\beta_1(t_2-\tau)}\mathbf{c}_p(\tau)d\tau, \ldots, \int_0^{t_m} e^{-\beta_1(t_m-\tau)}\mathbf{c}_p(\tau)d\tau \tag{36}$$

Then, we can follow the same derivations as those of 3-K compartment model.

In general, performance of tumor detection is degraded with respect to that of the 3-K model. This is expected, since the 4-K model has additional parameter with respect the 3-K model. However, how to determine that additional parameter β_1 of 4K model is a difficult problem. Previous work has proposed many methods to resolve this problem, like classical nonlinear least squares (NLS), weighted integration method (WIM) and generalized linear least squares (GLLS) method. For most cases, those techniques work well when the tumor location is known. However, if the tumor is unknown, we have to go through every pixel in the image to estimate the parameters. It is time consuming and the computational requirement is high. Moreover, how to set the initial value is also a strong concern. Therefore, in the proposed approach, we take a different way to implement the parameter estimation.

It is shown in [20]that $\mathbf{c}_p(t)$ satisfies two constrains in the noise free case: first, $\mathbf{c}_p(t) > 0$ for $t > 0$; second, there exists a constant T_k such that $\frac{dC_p(t)}{dt} > 0$ when $t < T_k$ and $\frac{d\mathbf{c}_p(t)}{dt} < 0$ when $t > T_k$. With these constrains, it has been proved that for a given time T, $T > T_k$, there exists a threshold β_1^* of the macroparameter in dynamic FDG-PET for each individual patient, such that the physiological process function specified by β_1^* is horizontal (e.g. $\frac{\partial \mathbf{c}_p(t)\otimes e^{-\beta^* t}}{\partial t} = 0$) at a certain time $t = T > T_k$. Further more, when $T_k < t$, the physiological functions with $\beta < \beta_1^*$ will increase monotonically, or otherwise decrease when $\beta_1 > \beta_1^*$. We also notice that the the physiological process function for tumor cell will go up along with time; physiological process function of inflammation cell will be roughly flat after a long time; while the normal cell's physiological process function will go down. Therefore, wehn decomposing a TAC into a linear combination of many physiological process functions, we hypothesize that *the physiological functions with β_1 smaller than β_1^* are associated to malignancy tissue, but the physiological functions with β_1 larger than β_1^* are related to normal tissue.*

Based on above finding, we can first determine the value of β_1^*, which is the first step of our parameter estimation method. Then, we choose several predefined β_1 values by spacing the interval

$[0, \beta_1^*]$ uniformly or logarithmically. In the next step, we form a constrained filter bank, in which each filter is corresponding to one predefined value of β_1 and generated by the proposed approach of this work. Suppose there are N branches in the filter bank, after using this constrained filter bank to process the dynamic PET images, the output vector of a certain pixel in the PET image is given by

$$\mathbf{r} = [r_0, r_1, \ldots, r_{N-1}]^T \tag{37}$$

$$r_i = \mathbf{w}_i{}^T \mathbf{c}_{total} = M_1 \mathbf{w}_i{}^T \mathbf{s}_p + \mathbf{w}_i{}^T \mathbf{e} \tag{38}$$

$$= s_i + z_i \tag{39}$$

where s_i is the desired signal of the ith branch in the constrained filter bank and z_i is the interference and noise of branch i.

Because $\mathbf{z} = [z_0, z_1, \ldots, z_N - 1]^T$ is not white, the covariance matrix $\mathbf{R_z} = \mathbf{z}\mathbf{z}^T$ is not necessarily a scaled identity matrix. Therefore, we pass the output vector $\mathbf{r}$ through a noise whitening filter, the resulting signal is given by:

$$\mathbf{r}\prime = \mathbf{s}\prime + \mathbf{z}\prime = \mathbf{s}\mathbf{R_z}^{-1/2} + \mathbf{z}\mathbf{R_z}^{-1/2} \tag{40}$$

where $\mathbf{r}\prime = [r_0\prime, r_1\prime, \ldots, r_{N-1}\prime]^T$.

Finally, we use Maximal Ratio Combining (MRC) technique to combine the output of all branches simultaneously. At this stage, each of the branch output is weighted with a gain factor proportional to its own SNR and all of the output are combined to give the resulting output image, which has the best SNR value. The output of the MRC scheme can be written as follows:

$$y = \sum_{i=0}^{N-1} g_i r_i\prime \tag{41}$$

where g_i is the combining factor of branch i and the derivation of g_i is given in Appendix B.

The constrained filter bank and maximal ratio combining scheme is shown in Figure. 2.

How to extract the features of the interference caused by background FDG concentration $\mathbf{b}_g$ is another strong concern of the proposed technology. The simplest way to resolve this problem is that we do not use any background information when we form the $\mathbf{e}_{sub}$, ie. , $\mathbf{e}_{sub} = \mathbf{c}_p$. However, we

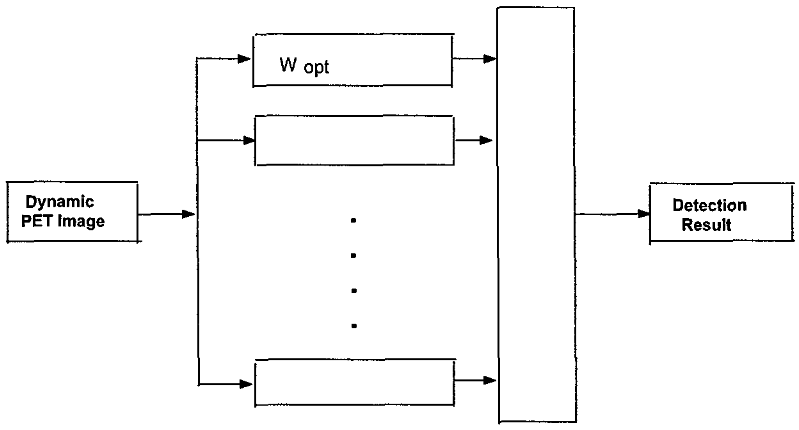

Figure 2: Constrained temporal filter bank

still want to eliminate the background interference as much as possible, since the background FDG concentration will definitely degrade the image quality of the detection result. In our approach, we draw ROIs in the dynamic PET image and obtain the $\mathbf{b}_g$ from the ROI of the background area. Then we form the $\mathbf{e}_{sub}$ as $\mathbf{e}_{sub} = [\mathbf{c}_p, \mathbf{b}_g](33)$ and generate the optimum weight vector $\mathbf{w}$ for the whole image. The best way to form the $\mathbf{i}_{sub}$ is to acquire the features of $\mathbf{b}_g$ adaptive. For instance, we can use computed tomography (CT) to segment the whole PET image and distinguish several different background area. Then we draw ROIs in these background area and extract several difficult features $\mathbf{b}_g^1$, $\mathbf{b}_g^2$,...,$\mathbf{b}_g^n$. The background interference is expressed by

$$\mathbf{e}_{sub}^i = [\mathbf{c}_p, \mathbf{b}_g^i] \tag{42}$$

then we use $\mathbf{e}_{sub}^i$ to generate the optimum weight vector $\mathbf{w}^i$ for the ith segmentation of the PET image.

4.4 Decision Criterion

The problem of detecting small areas of images which differ in some statistical sense from their immediate surroundings is of considerable interest in a number of image processing applications. This section addresses a power detection algorithm which is the locally optimal detector for random objects in Gaussian backgrounds. For the 3-K compartment model, the two hypotheses of our problem are given by (14):

$$H_0 \ : \qquad x_i = n_i = \mathbf{w}^T\mathbf{e} \tag{43}$$

$$H_1 \ : \qquad x_i = s_i + n_i = K_i\mathbf{w}^T\mathbf{s}_p + \mathbf{w}^T\mathbf{e} \tag{44}$$

where x_i is the a certain pixel in the ith segmentation of the PET images, s_i is the equivalent desired signal and n_i is the equivalent noise. We assume that n_i is Gaussian process with local mean m_i and power spectral density σ_i^2.

Because signal-plus-noise density is unknown due to the uncertainty of tumor location, likelihood ratio test can not be applied in our case. However, since we can measure the first and second moment statistics of equivalent noise n_i from the images, power detection scheme can provide great probability of detection for a given false alarm rate. This power detector consists of a half-wave linear device with the transfer characteristic

$$y_i = \begin{cases} x_i, & when\ x_i \geq 0\ ; \\ 0, & when\ x_i < 0\ . \end{cases} \tag{45}$$

Then by taking the power of y_i and applying a power detector, the decision criterion becomes

$$"if \quad z_i > f(\alpha_i), \qquad then\ decide\ object\ present" \tag{46}$$

with the threshold $f(\alpha_i)$ is a function of false alarm rate α_i

$$\alpha_i = Q(\frac{f(\alpha_i) - m_i}{\sigma_i}) \tag{47}$$

where z_i is the power of y_i and the Q-function is defined by

$$Q(x) = \frac{1}{\sqrt{2\pi}} \int_x^\infty e^{-t^2/2} dt \tag{48}$$

The derivation of Equation (48) is given in Appendix C.

Following the same procedure, we can derive the decision criterion for the 4-K compartment model.

5 EXPERIMENT RESULTS AND DISCUSSION

5.1 Digital phantom Study

In our digital phantom study, we use the simulated dynamic PET images, containing a uniformly distributed ellipsoid background and 9 small tumors. Among them, the three tumors in the upper row are crosses of 3×2 pixels, containing 5 pixels in total. The middle and bottom three tumors are squares of 2×2 pixels and 3×3 pixels, respectively. The area of each pixel is $2.7mm$ and tumor-to-background ratio is equal to 1.5. The time-activity curves of the tumor and normal tissue, which are used to generate this original phantom image, are extracted from the clinic patient data.Three different methods have been applied to process the phantom image: Patlak analysis, spectral analysis (SA) and the constrained temporal filter. Visual results Figure.3(a) shows the original phantom image (true image), which contains nine artificial tumors in a uniform backgroud. Two noisy and noise-free Filtered Backprojection (FBP) reconstructed phantom images are showed in Figure.3(b) and Figure.3(c). Both of figures show the last frame of the reconstructed phantom images, which are believed to have the highest tumor-to-background contrast among al dynamic images. By comparing the Figure.3(a) and Figure.3(b), we can clearly see the distortion caused by partial volume effect. Figure.3(d), Figure.3(e) and Figure.3(f) are the results of the noisy image in Figure.3(c) processed by Patlak, SA and the constrained temporal filter, respectively. Figure.3(g) shows the TACs drawn from the tumor and background in the original phantom image. Figure.3 (h)is the TACs drawn from the boundary of the tumor in the noise-free FBP reconstructed phantom image, which actually is the mixture of the two TACs showed in the Figure.3(g) because of PVE.

5.1.1 Quantitative results

For performance evaluation, we measured the SNR and CNR in the output images resulted from the above three methods. The definitions of SNR and CNR are described next.

(1) *Singal-to-Noise Ratio*

We use the same definitions of SNR and CNR given in [19]. Let ${V_{jk}}^d$ be the value of the $(j,k)th$ pixel in the desired ROI(DROI). ${V_{jk}}^d$ consists of a deterministic value plus statistical noise; the desired deterministic value if then the mean $E(V_j k^d)$, and the strength of the noise is the standard deviation $[var({V_{jk}}^d)]^{1/2}$. Signal-to-noise ratio of the desired feature (SNR_d) is defined as

$$SNR_d = \frac{E({V_{jk}}^d)}{\sqrt{var({V_{jk}}^d)}} \tag{49}$$

where $E(V_j k^d)$ and $[var({V_{jk}}^d)]^{1/2}$ in a homogeneous region can be estimated using the sample mean and variance.

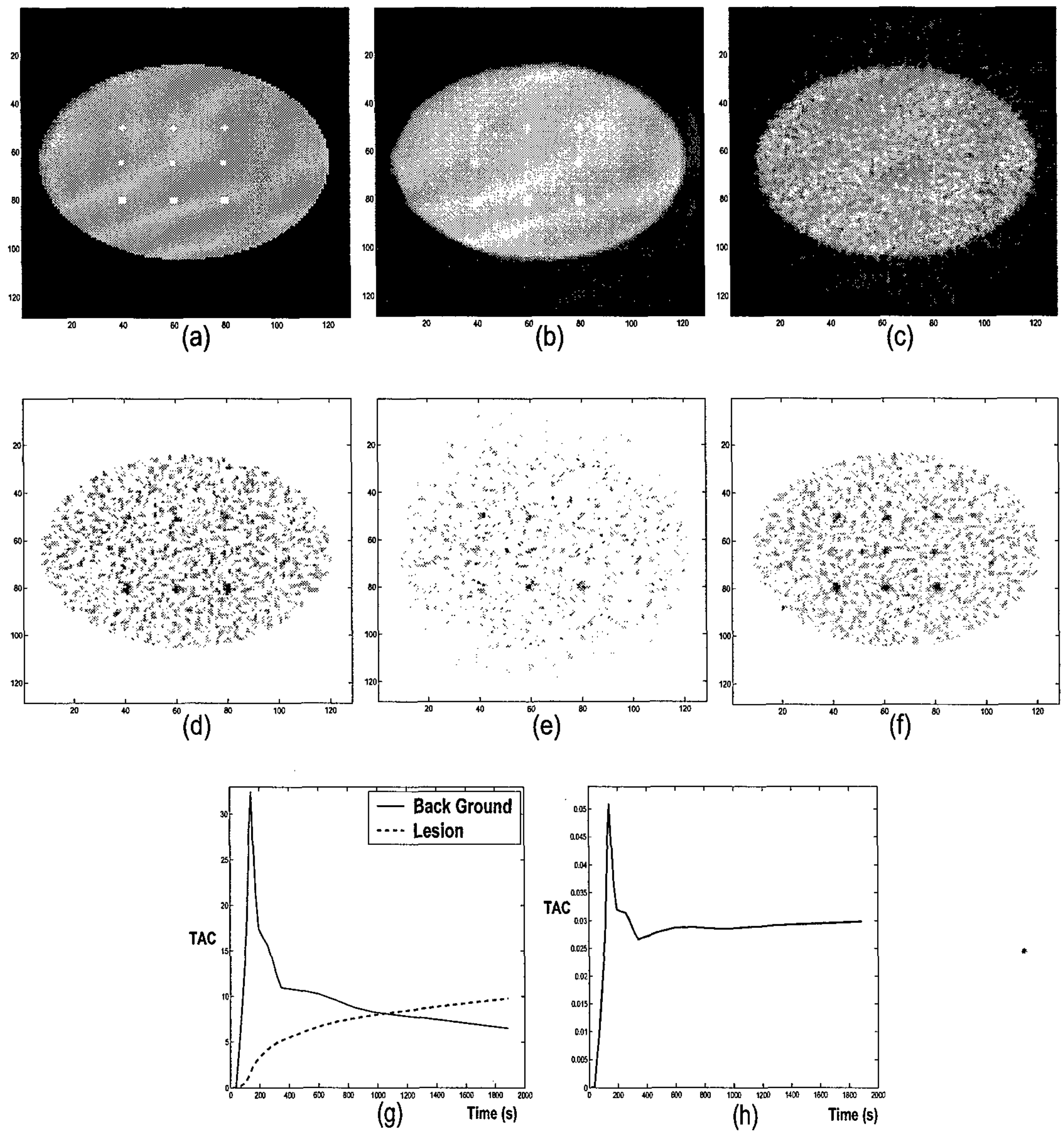

Figure 3: Results of digital phantom study. (a) Original phantom image, (b) FBP reconstructed phantom image (noise free), (c) FBP reconstructed phantom image (with noise), (d) Noisy image in Figure.3(c) processed by Patlak analysis, (e) Image in Figure.3(c) processed by SA, (f) Image in Figure.3(c) processed by constrained temporal filter.

TABLE I
PERFORMANCE OF PATLAK , SA AND CONST. FILTER

	SA		Patlak		Const. Filter	
	SNR	CNR	SNR	CNR	SNR	CNR
Tumor (1,1)	1.157	0.833	2.238	1.472	1.434	1.064
Tumor (1,2)	1.672	2.009	1.113	0.954	1.385	1.403
Tumor (1,3)	0.945	1.213	2.184	2.090	3.298	3.326
Average of above 3 tumors	***1.258***	***1.352***	***1.845***	***1.505***	***2.039***	***1.931***
Tumor (2,1)	1.322	1.468	1.270	0.755	2.136	1.789
Tumor (2,2)	1.169	1.414	2.084	1.848	3.172	3.026
Tumor (2,3)	0.500	0.254	1.700	1.037	3.609	3.487
Average of above 3 tumors	***0.997***	***1.045***	***1.685***	***1.214***	***2.972***	***2.767***
Tumor (3,1)	0.618	0.240	1.359	1.068	1.633	1.472
Tumor (3,2)	1.185	1.418	2.054	1.788	3.188	3.001
Tumor (3,3)	1.715	1.960	3.086	2.700	2.854	2.724
Average of above 3 tumors	***1.173***	***1.206***	***2.166***	***1.852***	***2.559***	***2.399***

(2) *Contrast-to-Noise Ratio*

In addition to SNR_d, the CNR between the desired signal (tumor tissue) and undesired signal (interference) is usually important for image interpretation. The CNR between the desired signal and undesired signal is defined as

$$CNR_{du} = \frac{E({V_{jk}}^d) - E({V_{jk}}^u)}{\sqrt{0.5[var({V_{jk}}^d) + var({V_{jk}}^u)]}} \tag{50}$$

where ${V_{jk}}^u$ is the value of the $(j,k)th$ pixel in the undesired ROI (UROI), and $E(V_jk^u)$ and $var({V_{jk}}^u)$ are the mean and the variance of pixel values in UROI, respectively.

By using (49) and (50), Table I compares the quantitative results of Patlak analysis, spectral analysis (SA) and the constrained temporal filter. As Fig.3(a) shows, the nine tumors in original phantom data are arranged as a 3×3 matrix. The index (i, j) of that matrix are used in Table I to indicate the location of tumors.

Both image results and numerical results suggest that the constrained temporal filter has the best performance. Comparing with the other two methods, the main advantage of our approach is that it can objectively remove the PVE superimposed onto the TAC and the residual blood activities in the pixel-by-pixel estimations of M_1.

5.2 Physical phantom Study

Figure 4: Results of physical phantom study.
(a) MAP reconstructed phantom image (b) Output image of processing Figure.4(a)by the constraint temporal filter, (c) Power detector result of Figure.4(b),

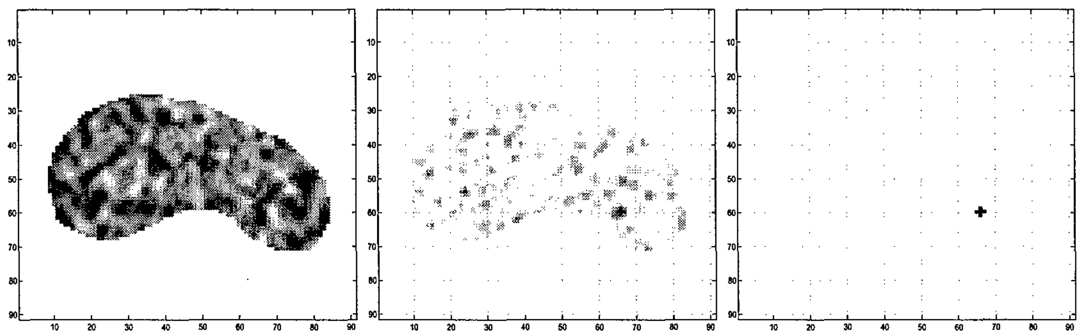

(a) (b) (c)

(a) MAP reconstructed phantom image (b) Output image of processing Figure.4(a)by the constraint temporal filter, (c) Power detector result of Figure.4(b),

5.3 Animal Study

Dynamic PET imaging of FDG (200 μci) was performed on a MicroPET R4 system (Concorde MicroSystems, Inc). Female athymic nude mice with human breast cancer cell MDA-MB-435 inoculated into both sides of mammary fat pads under the arms. Six days after inoculation, thirty-five dynamic data frames (6×1 sec, 4×3 sec, 10×30 sec, 5×60 sec, and 10×300 sec) were acquired for 1 hour after intravenous injection. Images were reconstructed with the OSEM algorithm, as shown in Figure.5(a). The corresponding time-activity curves of the two tumors, normal tissues and heart have already been shown in Figure.5(c). Figure.5(e) is the resulted image of Figure.5(a) after passing through the constraint temporal filter.

In Figure.5(b) we show the OSEM reconstructed image acquired twelve days after inoculation. Figure.5(d) demonstrates the corresponding TACs and Figure.5(f) is the resulted image of Figure.5(b) after passing through the constraint temporal filter. Comparing Figure.5(a) and Figure.5(b), we can see that the tumors grow bigger and the slope of tumor's TAC becomes larger after six more days. Based on detection result of Figure.5(h), we confirm that the findings in the filtered output image shown in Figure.5(g) are correct.

From the results of the mouse study, it appears that using constrained temporal filter is an optimal approach to eliminate the residual blood FDG activity especially for the stressing cases with difficulties to tell the difference between the slopes of tumor and normal tissues. This approach also offers a desirable result in eliminating partial volume effect (PVE) and image noise artifacts.

5.4 Clinic Study

5.4.1 Protocol of Dynamic PET-FDG Study

The clinical PET-FDG dynamic data was acquired with a Siemens/CTI ECAT Model 953A whole-body PET scanner. This device provides 31 contiguous transaxial image planes with an axial field of view of 10.8 cm. The nominal intrinsic resolution of the system is 4 mm in all 3 dimensions. Consecutive detector rings are separated by tungsten septa in order to reduce scatter noise. Dynamic data will be acquired from 0 to 55 minute post injection.The dynamic structure protocol for the clinical data acquisition was listed in Table 2.

Scan Type	Scan Times	Frame Duration
Dynamic scan	0 - 2 min	15 sec/frame
Dynamic scan	3 - 5 min	30 sec/frame
Dynamic scan	6 - 25 min	1 min/frame
Dynamic scan	26 - 45 min	5 min/frame

Table 1: TABLE II: Dynamic Data Acquisition Protocol

5.4.2 Clinical Breast Cancer Study

Two breast cancer images at different planes are tested: one for the primary tumor, another for metastatic lymph node.

5.4.3 Clinical Lung Cancer Study

The detection procedures are same as the breast cancer case. The image contains one confirmed primary tumor and one confirmed metastatic lymph node

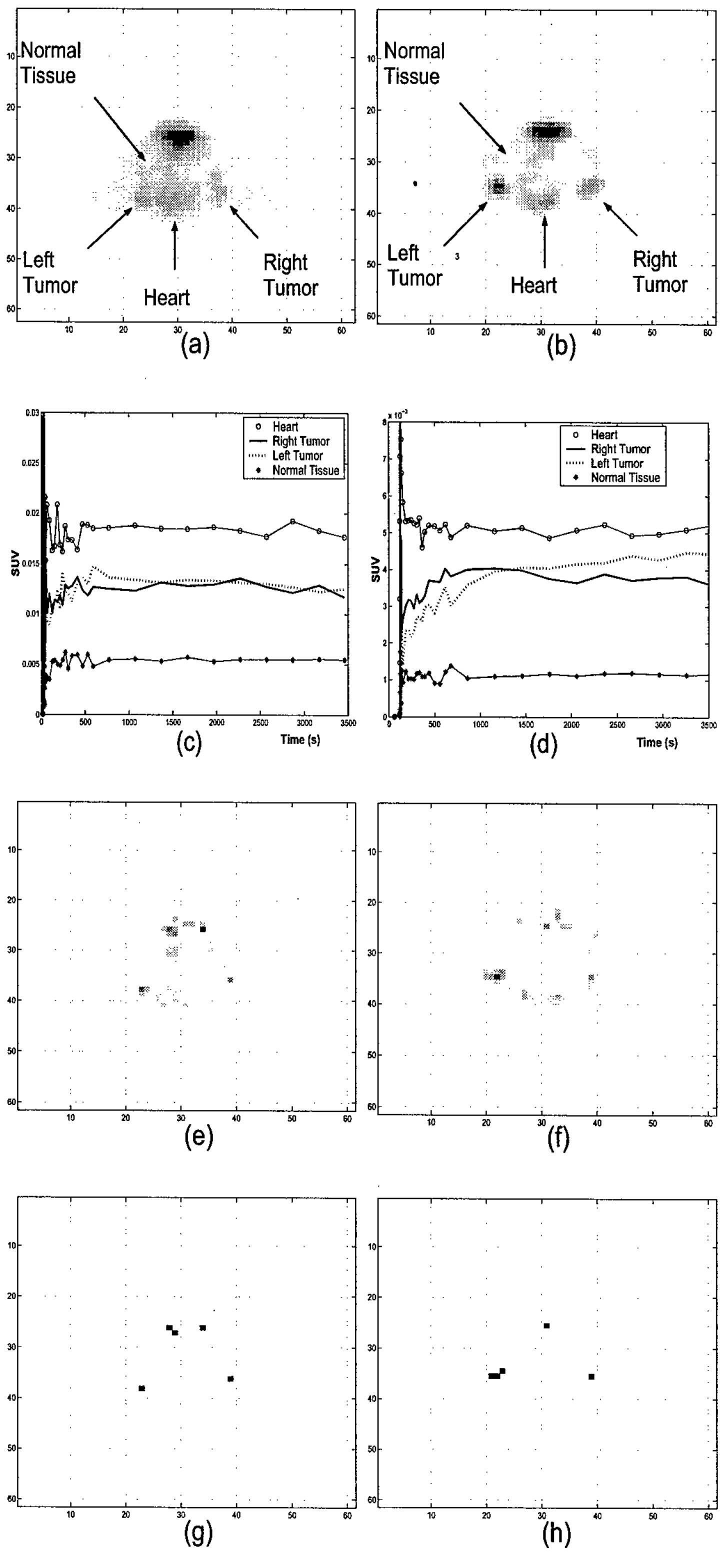

Figure 5: Results of animal study. (a) OSEM Reconstructed FDG-PET image (six days after inoculation) at the last frame with the highest tumor-to-backgournd ratio, (b) OSEM Reconstructed FDG-PET image (twelve days after inoculation) at the last frame with the highest tumor-to-backgournd ratio, (c) TACs drawn from Figure.5(a), (d) TACs drawn from Figure.5(b), (e) Output image of processing Figure.4(a)by the constraint temporal filter, (f) Output image of processing Figure.4(b)by the constraint temporal filter, (g) Power detector result of Figure.5(e), (h) Power detector result of Figure.5(f).

Figure 6: Results of constrained filter.

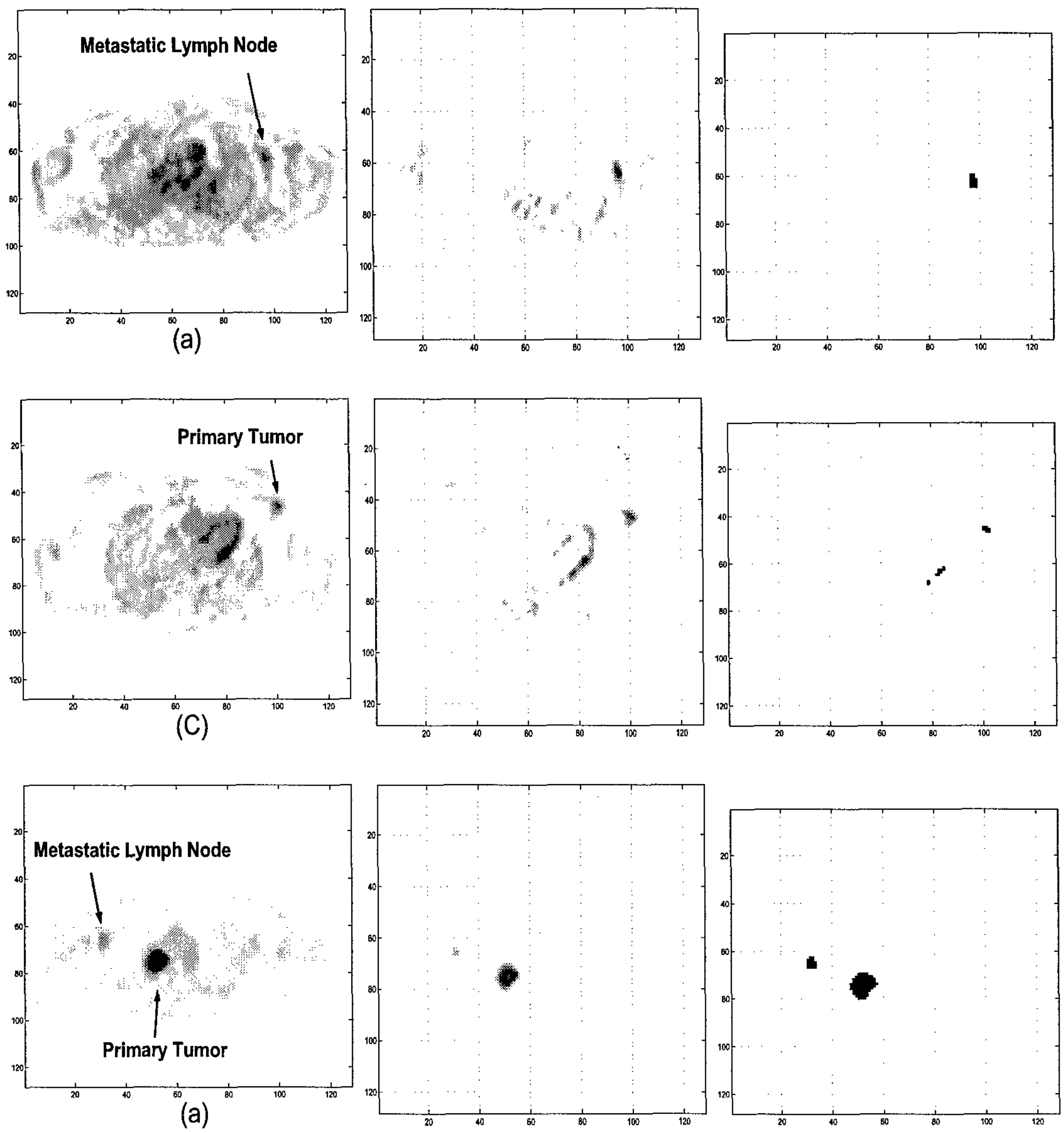

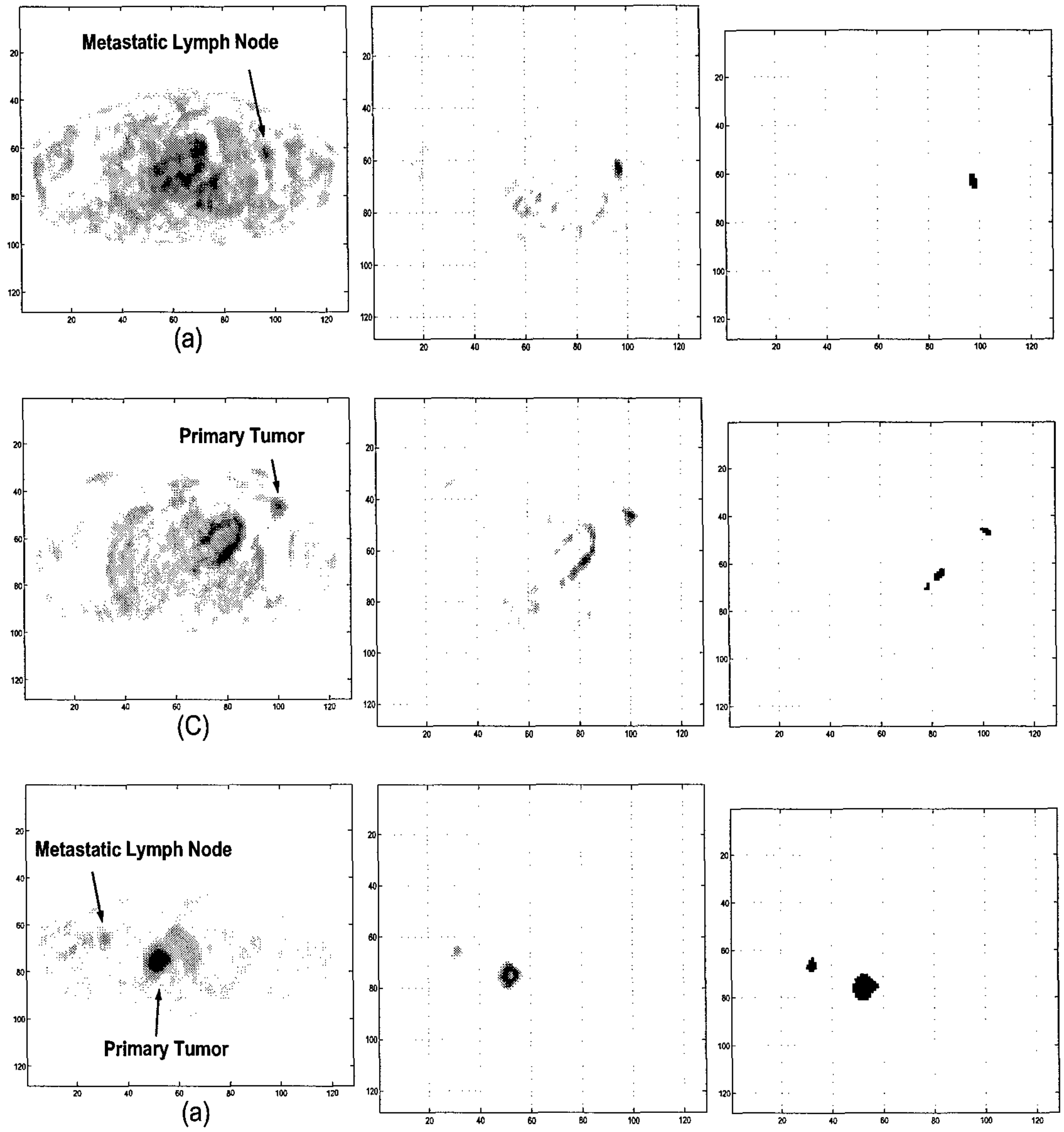

Figure 7: Results of constrained filter bank

6 CONCLUSION

Enhancement of tumor-to-background contrast in dynamic PET images may be obscured by residual FDG-associated activity in normal tissues and blood as well as by PVE. Even though Patlak method and spectral analysis can improve tumor visualization when tumors are large, it fails sometimes when tumor and normal tissues have the almost same slope of TAC due to the PVE. A new approach of using the constrained temporal filter seems to be superior to Patlak and SA methods as shown in our digital phantom study and the animal study of early detection with mouse.

7 APPENDIX

7.1 A

The problem of optimization subject to a constraint may be handled with the Lagrange multiplier method. We define the performance index

$$I(\mathbf{w}) = \mathbf{w}^T \mathbf{R_e} \mathbf{w} + \Lambda(\mathbf{w}^T \mathbf{H} - \mathbf{f}^T) \tag{51}$$

where Λ is K-dimensional column vector of Lagrange multiplier. We may determine the optimum weight vector $\mathbf{w}$ by setting the derivatives of $I(\mathbf{w})$ with respect to w_i equal to zero,

$$\frac{\partial I(W)}{\partial w_i} = 0, 1 < i \le m \quad and \quad \mathbf{w} = [w_1, w_2, \ldots, w_m]^T \tag{52}$$

Then, we obtain

$$\nabla_{\mathbf{w}} I(\mathbf{w}) = \mathbf{R_e}\mathbf{w} + \mathbf{H}\Lambda = 0 \tag{53}$$

where

$$\nabla_{\mathbf{w}} = [\frac{\partial}{\partial w_1}, \frac{\partial}{\partial w_2}, \ldots, \frac{\partial}{\partial w_m}]^T \tag{54}$$

The optimum weight vector is then

$$\mathbf{w} = -\mathbf{R_e}^{-1}\mathbf{H}\Lambda \tag{55}$$

To evaluate $\mathbf{w}$, we have to know Λ. However, since $\mathbf{w}$ must satisfy the constraint, the following relation holds:

$$\mathbf{H}^T\mathbf{w} = -\mathbf{H}^T\mathbf{R_e}^{-1}\mathbf{H}\Lambda = \mathbf{f} \tag{56}$$

Hence,

$$\Lambda = -(\mathbf{H}^T\mathbf{R_e}^{-1}\mathbf{H})^{-1}\mathbf{f} \tag{57}$$

and Equation (55) gives

$$\mathbf{w} = \mathbf{R_e}^{-1}\mathbf{H}(\mathbf{H}^T\mathbf{R_e}^{-1}\mathbf{H})^{-1}\mathbf{f} \tag{58}$$

7.2 B

The combined output of the MRC scheme can be written as follows:

$$y = \sum_{i=0}^{N-1} g_i r_{i'} = \sum_{i=0}^{N-1} g_i s_{i'} + \sum_{i=0}^{N-1} g_i z_{i'} \tag{59}$$

where g_i is the combining factor of branch i and $z_i\prime$ of the different branches are uncorrelated. The SNR of the combined output signal is given by

$$\Gamma = \frac{\sum_{i=0}^{N-1} {g_i}^2 {E_s}^i}{\sum_{i=0}^{N-1} {g_i}^2 {\sigma_i}^2} \tag{60}$$

where ${\sigma_i}^2$ is the power spectral density of $z_i\prime$ and ${E_s}^i$ is the energy of $r_i\prime$. The combining gain factors should be chosen in order to maximize the above SNR. By using Schwarz inequality we can write the above resulting SNR as

$$\Gamma \leq \frac{(\sum_{i=0}^{N-1} {g_i}^2 {\sigma_i}^2)(\sum_{i=0}^{N-1} {E_s}^i/{\sigma_i}^2)}{\sum_{i=0}^{N-1} {g_i}^2 {\sigma_i}^2} = \sum_{i=0}^{N-1} \frac{{E_s}^i}{{\sigma_i}^2} \tag{61}$$

Equality in Schwarz inequality is obtained if and only if combining gain factors are chosen as

$$g_i = k \frac{\sqrt{{E_s}^i}}{{\sigma_i}^2} \tag{62}$$

where k is an arbitrary positive constant. Thus, the maximum value of the output SNR is given by

$$\Gamma = \sum_{i=0}^{N-1} \frac{{E_s}^i}{{\sigma_i}^2} = \sum_{i=0}^{N-1} \Gamma_i \tag{63}$$

Consequently, the SNR of the resulting signal is equal to the sum of the SNRs in each branch for maximal ratio combining.

7.3 C

For the desired signal absent hypothesis H_0, the probability density function of x_i is given by

$$p_{x_i}(x_i) = \frac{1}{\sqrt{2\pi}\sigma_i} e^{-\frac{(x_i - m_i)^2}{2{\sigma_i}^2}} \tag{64}$$

The probability distribution function of the output of the half-wave linear device can be expressed in terms of the input borbability density function as

$$P(y_t \leq y_i) = 0 \qquad for\ y_i < 0 \tag{65}$$

$$or \quad P(y_t \leq y_i) = P(x_i < 0) + \int_0^{y_i} p_{x_i}(x_i) dx_i \qquad for\ y_i \geq 0 \tag{66}$$

By differentiating Equation (66)with respect to y_i, we get

$$p_{y_i}(y_i) = P(x_i < 0)\delta(y_i) + p_{x_i}(y_i)U(y_i) \tag{67}$$

where $U(y_i)$ is the unit step function. Since $z_i = (y_i)^2$, $y_i \geq 0$

$$p_{z_i}(z_i) = Q(\frac{m_i}{\sigma_i})\delta(\sqrt{z_i}) + \frac{1}{2\sqrt{2z_i\pi}\sigma_i}e^{-\frac{(\sqrt{z_i}-m_i)^2}{2\sigma_i{}^2}}U(\sqrt{z_i}) \tag{68}$$

The false alarm rate α_i is given by

$$\alpha_i = \int_{f(\alpha_i)}^{\infty} p_{z_i}(z_i)dz_i = Q(\frac{f(\alpha_i) - m_i}{\sigma_i}) \tag{69}$$

References

[1] L.P. Adler, J.P. Crowe, N.K. Al-kaisi, *et al.*, "Evaluation of breast masses and axillary lymph nodes with [F-18] 2-Deoxy-2-fluoro-D-glucose PET," *Radiology,* 187: p. 743-750, 1993.

[2] Keneth R. Zasadny and Richard L. Wahl, "Enhanced FDG-PET Tumor Imaging with Correlation-Coefficient Filtered Influx-Constant Images", *The Journal of Nuclear Mecidine,* Vol.37, No.2, February 1996.

[3] K. Kubota, T. Matsuzawa, *et al.,* "Differential diagnosis of lung tumor with positron emission tomography: a prospective study," *Journal of Nuclear Medicine,* Vol. 31, pp. 1927-1933, 1990.

[4] E. J. Hoffman, S. C. Huang, and M. E. Phelps, "Quantitation in positron emission computed tomography: 1. Effect of object size," *J. Comput. Assist. Tomogr.,* Vol. 3, pp. 299-308, 1979.

[5] C. S. Patlak, R. G. blasberg, and J. Fenstermacher, "Graphical evaluation of blood to brain transfer constants from multiple-time uptake data", *J. Cerebral Blood Flow and Metabolism,* Vol. 3, pp. 1-7,1983.

[6] V. J. Cunningham, T. Jones, "Spectral analysis of dynamic PET studies", *J. Cereb Blood Flow Metab,* Vol.13, pp. 15-23,1993

[7] M. A. King, P. W. doherty, and R. B. Schwinger, "A Wiener filter for nuclear medicine images," *Med. Phys.,* Vol. 10, pp. 876-880, 1983.

[8] M. A. King, B. C. Penney, and S. J. Glick, "An image-dependent Metz filter for nuclear-medicine imagesc," *J. Nucl. Med.,* Vol. 29, pp. 1980-1989, 1988.

[9] F. E. Turkheimer, John A. D. Aston, Richard B. Banati, Cyril riddell, and Vincent J. Cunningham, "A linear wavelet filter for parametric imaging with dynamic PET," *IEEE Trans. Med. Imaging,* Vol. 22, No. 3, March 2003.

[10] S.C. Huang, M.E. Phelps, E.J. Hoffman, K. Sideris, C.J. Selin, and D. E. Kuhl, "Noninvasive determination of local cerebral metabolic rate of glucose in man," *Amer. Physiological Society,* E69-E82, 1980.

[11] M.E. Phelps, J.C. Mazziotta, and H.R. Schelbert, *Positron Emission Tomography and Autoradiology, Principles and Applications for the Brain and Heart,* Raven Press, 1986.

[12] L. Sokoloff, M. Reivich, C. Kennedy, M. H. D. Rosiers, C. S. Patlak, K. D. Pettigrew, O. Sakurada, and M. Shinohara, "The [14C] deoxyglucose method for the measurement of local cerebral glucose utilization: Theory, procedure, and normal values in the conscious and anesthetized albino rat," *J. Neurochem,* vol.28, pp. 897-916, 1977

[13] V. J. Cunningham, J. Ashburner, H. Byrne, T. Jones, "Use of spectral analysis to obtain parametric images from dynamic PEt sutdies," In: K. Uemura (eds) *Quantification of brain function. Tracer kinetic and image analysis in brain PET,* Elsevier, pp. 101-108, 1993.

[14] S. R. Meikle, J. C. matthews, V. J. Cunningham, D. L. Bailey, L. Livieratos, T. Jones, P. Price, "Spectral analysis of PET projection data," *Nuclear Science Symposium, 1996. Conference Record., 1996 IEEE* Vol. 3, pp. 1888-1892, Nov. 1996.

[15] Y. Bresler, V. U. Reddy, and T. Kailath, "Optimum Beamforming for Coherent Signal and Interferences," *IEEE Trans. Acoust., Speech, Signal Processing,* Vol. 36, no. 6, June, 1988.

[16] V. U. Reddy, A. Paulraj, and T. Kailath, "Performance analysis of the optimum beamformer in the presence of correlated sources and its behavior under spatial smoothing," *IEEE Trans. Acoust., Speech, Signal Processing,* Vol, ASSP-35, pp. 927-936, July 1987.

[17] O. L. Frost, III, "An Algorithm for Linearly Constrained Adaptive Array Processing," *Proceeding of the IEEE,* 60, no. 8 (August 1972): 926.

[18] R. T. compton, Jr., "Adaptive Antennas-Concepts and Performance," New Jersey, Prentice Hall, 1988:361-367.

[19] J. N. Lee and S. J. Riederer, "the contrast-to-noise in relaxation time, synthetic, and weighted-sum MR images," *Magnet. Reson. Med.* vol. 5, pp. 13-22, 1987

[20] Zheng Li and Xiaoli Yu, "Exploring Frequency Difference of Physiological Processes to Enhance Dynamic FDG-PET without Knowing Blood Functioin",